Impurity–point defect complexes: Diffusion studies in Si and SiGe, and electrical studies in Ge

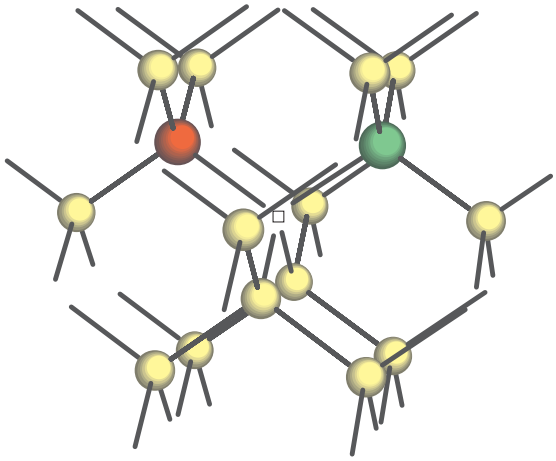

Ph.D. thesis

Jacob Fage-Pedersen

Institute of Physics and Astronomy
University of Aarhus, Denmark

This edition printed February 2001. Minor misprints have been corrected relative to the submitted version (November 2000) and the numbering of references and footnotes has changed.

Front illustration: An impurity–vacancy complex in the silicon lattice. A vacant lattice site (□) is neighboured by two large-size impurity atoms.

Contents

Preface **vii**
Acknowledgments . . . vii
Publications . . . viii
Participants in this work . . . ix
Reading guide to thesis . . . x

1 Introduction **1**
1.1 Si technology: Perfection and imperfection . . . 1
1.2 Downscaling and fast devices . . . 1
1.3 Irradiation-induced point defects . . . 3

2 Diffusion in silicon: Mechanisms, concepts, and theory **5**
2.1 Mechanisms of impurity diffusion in Si . . . 5
2.1.1 The diffusion equation . . . 5
2.1.2 Microscopic mechanisms . . . 6
2.1.3 Mechanisms of different elements . . . 8
2.2 Native point defects and their interaction with dopants . . . 10
2.3 Dopant diffusion in the extrinsic regime . . . 12
2.4 Activation energies of diffusion . . . 16
2.4.1 Self-diffusion . . . 16
2.4.2 Impurity diffusion . . . 18
2.4.3 Vacancy mechanism . . . 18
2.4.4 Interstitial-related mechanisms . . . 21

3 Diffusion studies: Experimental aspects **25**
3.1 Molecular-Beam Epitaxy (MBE) . . . 25
3.2 Secondary-Ion Mass Spectrometry (SIMS) . . . 28
3.3 Transmission-Electron Microscopy (TEM) . . . 33
3.4 Rutherford-back scattering spectrometry (RBS) . . . 34

4 Article: Sb diffusion in a high Sn-background concentration in Si **35**
4.1 Introduction . . . 35
4.2 Experimental details . . . 36
4.3 Experimental results . . . 37
4.4 Discussion . . . 40

5 Vacancy-mediated diffusion at high dopant concentrations **45**
5.1 Introduction . . . 45
5.2 Vacancy percolation in group-V backgrounds in Silicon . . . 46
5.2.1 Background . . . 46
5.2.2 Review of the vacancy-percolation model . . . 47
5.2.3 Some critical remarks . . . 50
5.3 Impurity–vacancy complexes . . . 51
5.3.1 Findings in the literature . . . 51
5.3.2 Comments . . . 54
5.4 Percolation or clustering? . . . 56
5.4.1 Discussion . . . 56
5.4.2 Concluding remarks . . . 58
5.5 The case of a Sn background . . . 59
5.5.1 On the analysis . . . 59
5.5.2 A final word on Sn precipitation . . . 61

6 Article: Si self-interstitial injection from Sb complex formation in Si **65**
6.1 Introduction . . . 65
6.2 Experiment and results . . . 67
6.3 Discussion . . . 74
6.4 Summary . . . 76

7 Comments on Sb-complex formation **77**
7.1 Precipitation and complex formation . . . 77
7.2 The kickout reaction . . . 79

8 Diffusion of P and B in strained and relaxed Si and SiGe **81**
8.1 Introduction . . . 81
8.2 Quantification of strain and compositional effects upon diffusion 83
8.3 Experimental details . . . 84
8.4 Results and discussion . . . 86
8.4.1 Effect of a surface cap . . . 86
8.4.2 Diffusion coefficients . . . 87
8.4.3 The effects of strain and Ge content . . . 91
8.4.4 Coupling between the entropy and the enthalpy . . . 92

9 Deep levels in semiconductors: Concepts and experimental issues 95
9.1 Carrier capture and emission 95
9.2 Experimental issues 98
9.2.1 Transient spectroscopies 98
9.2.2 Instrumentation 100

10 Article: Irradiation-induced defects in Ge studied by transient methods. 101
10.1 Introduction 101
10.2 Experimental Details 102
10.3 Experimental Results: Overview 103
10.4 Experimental Results: Analysis and Discussion 109
10.4.1 Level $E_{0.27}$ 113
10.4.2 Level $E_{0.37}$ 113
10.4.3 Level $H_{0.30}$ 116
10.4.4 Level $E_{0.29}$ 118
10.4.5 Levels $E_{0.13}$, $E_{0.19}$, and $E_{0.23}$ 118
10.4.6 Levels $E'_{0.19}$ and $E_{0.14}$ 119
10.4.7 Levels $E_{0.30}$, $E_{0.28}$, and $E_{0.21}$ 119
10.4.8 Variations In the Literature 120
10.5 Summary 121

11 Comments on deep levels in n-type Ge 123
11.1 On the defect levels in Ge 123
11.2 On the E center in $Si_{1-x}Ge_x$, $0 \leq x \leq 1$ 125
11.3 A digression: Arsenic diffusion in Ge 128

12 Summary and Conclusions 129

A Further experiments with MCTS in n-type Ge 133
A.1 On the possible coupling between $E_{0.37}$ and $H_{0.30}$ 133

References 139
List of references 139
Author index 151

Problems worthy of attack
Prove their worth by hitting back
PIET HEIN

Preface

This thesis is submitted to the Faculty of Science at the University of Aarhus, Denmark, to meet the requirements for the Ph. D. degree in physics. The work has been carried out under the supervision of Arne Nylandsted Larsen in the period from August 1996 to September 2000, in the MBE semiconductor group at the University of Aarhus. The purpose of the work has been to study the interactions among dopant atoms and between dopant atoms and native point defects (i.e., lattice vacancies and self-interstitial atoms) in Si, SiGe and Ge.

Acknowledgements

The author gratefully acknowledges the Faculty of Science at the University of Aarhus for having financed this work.

My gratitude is expressed to all the people that I have worked with in the MBE semiconductor group. Helpfulness and a relaxed atmosphere are some of the reasons why it has always been a great pleasure to be in the group. Of these people, I am especially indebted to my supervisor, Arne Nylandsted Larsen, for his friendly attitude and for providing open and very fruitful discussions. John Lundsgaard Hansen has been an inspiring colleague and I have many a time benefitted from his technical inventiveness. Pia Bomholt has been of valuable assistance in the chemistry lab and has been a most pleasant coworker. Much appreciation goes to Nikolaj Zangenberg for a fine collaboration and for helping me out with SIMS measurements from time to time. Jean-Jacques Goubet has been a splendid discussion partner concerning DLTS issues.

In the course of the experimental work, I have been fortunate to visit collaborators from other institutes. All SIMS measurements I have performed at the Microelectronics Center in Copenhagen, in connection with which measurements much appreciation is owed to Peixiong Shi for his helpfulness and tech-

nical skills. A special gratitude is owed to Abdelmadjid Mesli, of the PHASE[1] laboratory of CNRS,[2] Strasboug (presently at CNRS, Mulhouse) for providing good, analytical discussions, and for his ability to spread enthusiasm. Gratitude is owed to Margareta Linnarsson of KTH[3], Stockholm, for the collaboration on SIMS measurements during one of my visits to Stockholm. In the fall of 1998, I was lucky to work for two months in Scott Dunham's group at Boston University. That was a very enjoyable period for me, and I gained valuable knowledge on computer simulations and *ab initio* calculations.

My fellow *kontorkammerater* over the years and friends at the institute hopefully know what they have meant to me. And above all, the most sincere appreciation is expressed to my family.

Publications

The present work has so far resulted in the following publications:

[I] *Sn-background induced diffusion enhancement of Sb in Si*
Jacob Fage-Pedersen, Arne Nylandsted Larsen, Peter Gaiduk, John Lundsgaard Hansen, and Margareta Linnarsson, Phys. Rev. Lett. **81**, 5856 (1998).

[II] *Sb-precipitation induced injection of Si self-interstitials in Si*
P. Gaiduk, J. Fage-Pedersen, J. Lundsgaard Hansen, and A. Nylandsted Larsen, Phys. Rev. B **59**, 7278 (1999).

[III] *Si self-interstitial injection from Sb complex formation in Si*
J. Fage-Pedersen, P. Gaiduk, and A. Nylandsted Larsen, J. Appl. Phys. **88**, 3254 (2000).

[IV] *Irradiation-induced defects in Ge studied by transient spectroscopies*
J. Fage-Pedersen, A. Mesli, and A. Nylandsted Larsen, Phys. Rev. B **62**, 10116 (2000).

[V] *Boron diffusion in strained and relaxed $Si_{1-x}Ge_x$*
N. Zangenberg, J. Fage-Pedersen, J. Lundsgaard Hansen, and A Nylandsted Larsen, to appear in Defect and Diffusion Forum.

Parts of the work in the thesis have been presented by this author at the following conferences:

[1] PHASE: PHysique et Applications des SEmi-conducteurs
[2] CNRS: Centre National de la Recherche Scientifique
[3] KTH: Kungl Tekniska Högskolan

- Materials Research Society Spring Meeting, Symposium Z: "Diffusion Mechanisms in Crystalline Materials", San Francisco, May 1998 (poster presentation).

- Materials Research Society Spring Meeting, Symposium S: "Si Front End Processing – Physics and Technology of Dopant–Defect Interactions", San Francisco, May 1999 (oral presentation).

- Danish Physical Society Annual Meeting (Dansk Fysisk Selskabs Årsmøde), Nyborg, Denmark, June 1999 (poster presentation).

- CIMTEC:[4] "Mass and Charge Transport in Inorganic Materials, Fundamentals to Devices", Jesolo di Lido, Venice, Italy, May 2000 (oral presentation).

Participants in this work

The roles of the people who have contributed to the work presented in the thesis is outlined:

The *author* has performed nearly all the data analysis in articles [I,II,IV], nearly all measurements with SIMS (except those in article [V]) and DLTS, nearly all of the annealings, a large number of the MCTS measurements, most of the van de Graaf electron and proton irradiations, a number of the RBS measurements, and he has participated in most of the TEM investigations. *John Lundsgaard Hansen* has performed the MBE growths, the TEM investigations of article [V] and on the P-spike SiGe samples (Chap. 8), and most of the RBS measurements. *Pia Bomholt* has fabricated diodes, prepared TEM samples, and performed photolithography and chemical etchings (Chap. 8). *Nikolaj Zangenberg* has performed some of the SIMS measurements on the P profiles, as well as most of the work on article [V]. *Peter Gaiduk* performed the TEM measurements in articles [I–III] and most of the work on article [II]. Most of the MCTS measurements were carried out during the authors visits to the CNRS, Strasbourg, in close collaboration with *Abdelmadjid Mesli*, who has also performed a number of the DLTS measurements and played a large role in the discussion of the phosphorus data. A number of the SIMS measurements reported in article [I] were performed in close collaboration with *Margareta Linnarsson* during the authors visit at KTH in Stockholm. *Arne Nylandsted Larsen* has played a major role in the planning and the analysis of all the experiments and has also helped out on experimental issues in Aarhus.

[4] International Conferences, Materials and Technologies

Reading guide to thesis

The author of the thesis has chosen to include as separate chapters three articles, the full text of which was written by the aforementioned. These chapters are numbers 4, 6, and 10. In supplement to these articles, in other chapters, elaboration can be found on specific, selected details that deserve a fuller treatment, or other data that may be pertinent is presented.

This organization of the thesis is chosen over that of rewriting the articles which could have been done to achieve a more homogeneous inclusion of the material in the thesis. The author feels that the present form, despite an unavoidable amount of repetition, is much more useful to the reader since (i) she can skip exactly those parts (articles) with which she might already be acquainted, and (ii) the distinction is convenient as to what has previously been published and what has not.

In the remainder of the thesis, 'we' will generally mean this author, except, of course, within the text of the articles that are presented in chapters 4, 6, and 10.

Chapter 1

Introduction

1.1 Si technology: Perfection and imperfection

It can appear surprising that Si, being the second most abundant element on Earth (surpassed only by oxygen), was not discovered before 1824. This year, Si was isolated and described as an element by Jöns Jacob Berzelius, a Swedish chemist. Undoubtedly, the extreme impact that this material was going to have on society, was unthinkable at that time.

Today, Si crystals represent the highest perfection of material engineering that has ever been achieved, purified routinely to the parts-per-billion level. But fascinating as that is, to make the material of use in microelectronics, one must reintroduce imperfection by adding foreign atoms ('impurities') to the crystal. This must be done in a rather awkward way, since the impurities must be added in a spatially inhomogeneous, yet highly controlled manner.

In microelectronics, Si is by far the dominating material, leaving GaAs in control only of a smaller market for certain specialized applications (e.g., high-speed and light-emitting devices). The reason for the dominance of silicon in VLSI can be expressed very simply: MOS! The *m*etal-*o*xide *s*emiconductor transistor is the dominating device for use in very-large scale integrated circuits (VLSI). A MOS transistor is shown in Fig. 1.1. It has four regions: source, drain, channel, and gate. The source and drain regions are doped to be of the same type, n or p, while the channel must be of opposite type. Beneath the gate is a thin layer of insulating oxide (SiO_2) that acts as an electric capacitor, such that a change of the gate voltage will turn on and off the transfer of charge from the source to the drain. The success of Si is primarily due to the easy production of the high-quality, insulating oxide, and to the low fabrication cost of large single-crystalline Si wafers.

1.2 Downscaling and fast devices

The demand of continuously improving device speed and exponentially downscaling components has come to be known as Moore's law. For example, devices are made today with channel lengths below 150 nm, but the require-

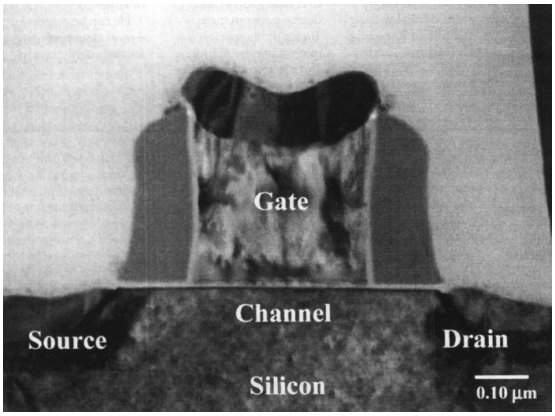

Figure 1.1: Cross section micrograph of a metal-oxide semiconductor (MOS) transistor. From Ref. [1]

ment in year 2008, as assessed in the Semiconductor Industry Association Roadmap [2, 3], is 50 nm. Since device fabrication involves several high-temperature processing steps, it is easily seen that a very precise knowledge of impurity redistribution at elevated temperatures is needed to achieve the optimum design of tomorrow's device.

The device resistance must also be kept low, and to achieve this, it is critical that the layers have very high electrical activity and very abrupt junctions. This puts stringent demands on the understanding of dopant-dopant interactions at high concentrations. Both the electrical deactivation and the redistribution of dopants is controlled by the interaction with point defects (lattice vacancies or self-interstitial atoms). Therefore, processes that can induce non-equilibrium concentrations of point defects, can be detrimental to the device. Examples of these processes are ion implantation, surface oxidation or nitridation, and even reactions between the dopants in the lattice.

Issues concerning dopant redistribution at high concentrations, as well as metastability of doped layers and generation of non-equilibrium point defect concentrations from highly doped layers are addressed in Chaps. 4–7.

As an alternative to downscaling, better device performance can be achieved if the carrier transfer through the device is sped up. As an example, a very fast heterojunction bipolar transistor (HBT) can be made with a B doped SiGe base layer sandwiched in-between the Si source and drain layers [4]. Due to the band gap alteration, the carrier mobility is increased by a factor of two to three relative to that in Si. SiGe HBT's have been in commercial production for a little over a decade, and they are giving increasing challenge to GaAs where high speed is needed, e.g., in wireless technology. However, since an easy-to produce insulator is not available for GaAs, this material fails where there is a

high demand for integration. SiGe, on the other hand, is CMOS[5] compatible and the production cost is only a fraction of that of GaAs.

In heterostructures, impurity diffusion can be anticipated to depend on both the Ge concentration and the inherent strain in the SiGe layers; the strain originates from the 4 % lattice mismatch between Si and Ge. In Chap. 8, precisely these issues are investigated in relation to the diffusion of P and B.

1.3 Irradiation-induced point defects

Much of the knowledge that we have on vacancies, self-interstitials, impurities, and complexes thereof, comes from experiments that do *not* involve heating of the sample to impurity diffusion temperatures ($\sim$ 700–1200 °C). In these experiments, involving temperatures near and below room temperature, it is necessary to manually introduce sufficient concentrations of point defects that their interactions with each other and with impurities can be studied. Often, these defects are introduced by means of proton, electron, or gamma-ray irradiation of the material.

Such is the case for experiments with deep-level transient spectroscopy (DLTS) which is one among several spectroscopic techniques (see Sec. 9.2.1), that can be used to obtain fundamental knowledge about point defects and impurity–point defect complexes in semiconductors. Some of the knowledge obtained with DLTS gives information that is pertinent also to diffusion studies, e.g., information on the charge states of the vacancy [5] and of the E center (the donor atom–vacancy pair) which is known to mediate diffusion of As and Sb at high temperatures. Also, information can be obtained on the evolution of defects, such as, e.g, the interaction of the E center with other defects, once the E center starts to migrate [6].

In the interest of devices, deep levels can be critical for the performance. Since deep levels are highly delocalized in k space, mid-gap levels (whether related to irradiation-induced defects or indiffused defects, such as, e.g., Au [7] or Pt in Si) can act as carrier recombination centers and dramatically reduce minority carrier life times, thereby influencing the switching time.

With respect to microelectronic device fabrication, interest in Ge was lost several years ago, due to the small band gap and the poor insulating property of the Ge oxide. This is one of the reasons why only few DLTS studies have been made on doped Ge. More attention, including DLTS studies [8], has been given to high-purity Ge, which is applied for detector fabrication. However, as was also described in Sec. 1.2, SiGe is becoming a more and more attractive material, and in the pursuit of understanding defects not only in Si, but also in

[5]CMOS: Complementary-metal oxide semiconductor; the logical circuit that is made by pairing n and p channel metal-oxide semiconductor field effect transistors (MOSFETS).

$Si_{1-x}Ge_x$ as a function of composition x, good knowledge must also be established of defects in Ge. Further, since the materials are so alike, Ge can act as a test bed for much of the current knowledge that exists on Si, and Ge may even help to shed new light on defect issues in Si.

In Chaps. 10 and 11, we present an investigation of irradation-induced defects in n type Ge, and we shortly comment on issues concerning the E center in $Si_{1-x}Ge_x$, $0 \leq x \leq 1$.

Chapter 2

Diffusion in silicon: Mechanisms, concepts, and theory

Theory and relevant concepts on diffusion in crystalline silicon are introduced according to the accepted understanding. The basic mechanisms of impurity- and self-diffusion are reviewed, and the role of point defects and their interactions with impurities is described. Values of activation energies of diffusion are also discussed. Highly recommended for a comprehensive overview are the review articles by Fahey, Griffin, and Plummer [9] and by Hu [10].

2.1 Mechanisms of impurity diffusion in Si

2.1.1 The diffusion equation

It is a gratefully simplifying circumstance that most semiconductor research is wafer-based. For this reason, a large fraction of dynamical problems are reduced to a single dimension x (viz. that perpendicular to the surface) with no need to invoke tensors [11]. On a macroscopic scale, the redistribution of an atomic species A is then quantified by the flux equation,

$$J_A = -D_A \frac{\partial C_A}{\partial x}, \tag{2.1}$$

and the continuity equation,

$$\frac{\partial C_A}{\partial t} = -\frac{\partial J_A}{\partial x}. \tag{2.2}$$

The first equation defines the diffusion coefficient D_A in terms of the flux J_A and the concentration C_A of atoms A. The equations combine to the *diffusion*

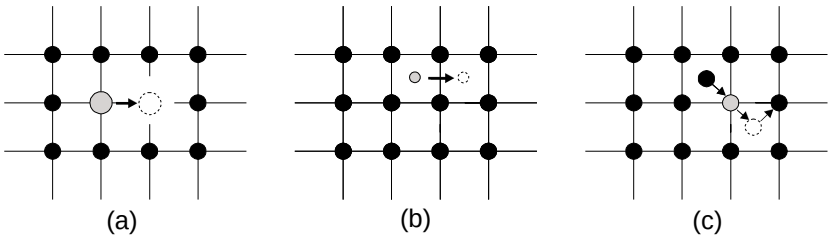

Figure 2.1: Diffusion mechanisms: (a) Vacancy, (b) direct-interstitial, and (c) interstitialcy.

equation:

$$\frac{\partial C_A}{\partial t} = \frac{\partial}{\partial x}\left(D_A \frac{\partial C_A}{\partial x}\right), \tag{2.3}$$

the numerical solution of which will give us the diffusional broadening of a given initial profile $C_A(x)$ for a particular choice of D_A.[6] In general (but, fortunately, not always), one can have a dependence like $D_A = D_A(C_A(x), x, t)$. A time dependence will enter in systems that are not thermodynamically equilibrated, and a position dependence will enter, e.g., if A interacts with a nonhomogeneous distribution of defects in the lattice or with an electric field (such as in a heterojunction, e.g.). Eqs. (2.1) and (2.3) are commonly referred to as Fick's first and second laws.

2.1.2 Microscopic mechanisms

We wish now to describe the atomic mechanism of the diffusion of an atomic species A in Si, A being a dopant atom or a Si tracer atom. The important issue is to determine the nature of the particular *mobile species* that involves A; this species frequently involves a native point defect, i.e., either a lattice vacancy V or a self-interstitial Si atom I.

In the *vacancy mechanism*, Fig. 2.1a, the isolated, substitutional atom A_s must meet with a vacancy

$$A_s + V \rightleftarrows AV \tag{2.4}$$

and then exchange sites with the vacancy in order to accomplish a diffusion step. If sufficient binding exists between A and V, they may diffuse as a *pair*. Owing to the diamond structure of the Si lattice, this pair must partially break up to accomplish a progressive diffusion step; the vacancy must migrate to

[6] For diffusion simulations in this work, the IRENE code [12] or a modification thereof was used.

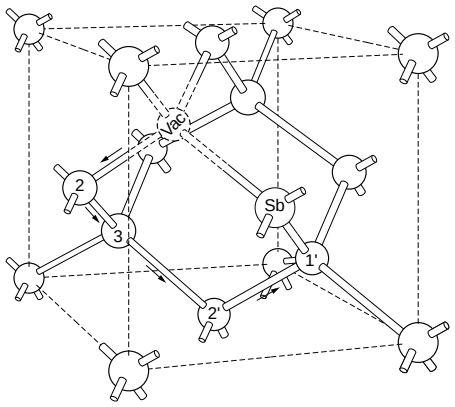

Figure 2.2: The Sb E center (substitutional Sb next to a vacancy) in the Si lattice. The arrows show a possible migration path that the vacancy can take between progressive hops of the Sb atom. Figure by courtesy of Nylandsted Larsen.

a 3rd nearest neighbour (3nn) position from A and back again along another path. This particular mechanism, after the group-V atom–vacancy pair, is often named the *E center mechanism* (Fig. 2.2).

The *direct-interstitial mechanism*, Fig. 2.1b, owes its existence to the large open, interstitial volumes of the silicon lattice. In this mechanism, the atom A which is dissolved mainly as an interstitial defect A_i, hops from one interstice to another and performs a diffusion that is usually very fast and has a low activation energy. Hybrid elements that have a high substitutional solubility but spend *some* of their time out of substitution via the reaction

$$A_\mathrm{s} \rightleftarrows A_\mathrm{i} + V, \tag{2.5}$$

may diffuse via interstitial sites while interstitial (A_i). This is known as the *Frank-Turnbull dissociative mechanism*.

In the *kickout mechanisms*, Fig. 2.1c, A also goes in and out of substitution, but now it is due to the interaction with a Si self-interstitial:

$$A_\mathrm{s} + I \rightleftarrows AI \quad \text{or} \tag{2.6}$$

$$A_\mathrm{s} + I \rightleftarrows A_\mathrm{i}, \tag{2.6$'$}$$

Here, AI denotes a dopant-interstitialcy defect, i.e., it is a bound pair that consists of a non-substitutional impurity atom and a Si self-interstitial and is positioned about a single substitutional lattice site. For most practical considerations, including modelling of dopant/self-interstitial profiles, it is either not possible or it is not important to distinguish between reactions (2.6) and (2.6′).[7]

[7] Frequently, the term 'kickout' is used to describe simply a mechanism where A_s interacts with a self-interstitial and migrates a long distance (several lattice constants) before it rests again in an isolated substitutional configuration. But notice that due to the indistinguishability of self--interstitials, whether this movement is via reaction (2.6) or (2.6′), the same net migration is caused: A dopant atom and a Si self-interstitial atom have moved equal distances in the same direction

Therefore one often refers simply to an *interstitial-related* mechanism. In this thesis, unless distinction is important, that term will be used to refer to either of mechanisms (2.6) and (2.6′). The mechanism, however, should not be confused with the direct-interstitial mechanism, since the latter is the only one of the above mechanisms where diffusion is *not* the result of an interaction with a thermally generated point defect, V or I.

Finally, in the *concerted-exchange* mechanism, two substitutional atoms directly interchange positions in one hop. The mechanism has never been directly observed; instead, rather small upper bounds can be given [13] to its fractional contribution to diffusion.

2.1.3 Mechanisms of different elements

In general it can be expected that the element A can participate in a distribution of different, mobile species $AX = (AI, A_i, AV, ...)$. If we denote by C_A, C_{A_s}, and C_{AX}, respectively, the total, the substitutional, and the mobile concentrations of A (such that $C_{A_s} + \sum_X C_{AX} = 1$) then the total diffusivity of A will be given by

$$D_A C_A = \sum_X d_{AX} C_{AX} = d_{AI} C_{AI} + d_{AV} C_{AV} \tag{2.7}$$

where d_{AX} is the diffusivity of AX. d_{AX} is a nontrivial quantity that depends on jump frequency and correlation.[8] In the last equality above we have restrained the discussion to a mixed vacancy and interstitial-related (interstitial or interstitialcy) mechanism; $X = I, V$, respectively. We define the *fractional interstitial* and *vacancy components*, f_{AI} and f_{AV}, $f_{AI} + f_{AV} = 1$, by the relations

$$D_A^* C_A f_{AI} \equiv d_{AI} C_{AI}^*, \quad D_A^* C_A f_{AV} \equiv d_{AV} C_{AV}^*. \tag{2.8}$$

Important in these relations is the asterisk (*) which denotes thermal-equilibrium quantities. C_{AX}^* and D_A^* will differ from the current quantities C_{AX} and

[8] For example, for impurity diffusion via vacancies in a cubic crystal (see Chaps. II, V of Ref. [14]),

$$d_{AV} = f_{AV} \frac{1}{6} \lambda^2 \zeta \omega_e = f_{AV} \beta a^2 \omega_e,$$

where λ is the hop length (bond length), ζ is the coordination number (4 for Si), ω_e is the A–V exchange frequency, a is the lattice parameter (5.43 Å for Si) and $\beta = 1/8$ for the diamond lattice ($\beta = 1$ for other cubic crystals). $f_{AV} \in [0, 1]$ is the *correlation factor*, sometimes called a geometric factor. It accounts for the fact that if the directions of subsequent impurity hops are correlated, then the diffusion length may be smaller than that expected for the same number of completely random hops. For impurity diffusion, the correlation factor depends on the local frequencies $\{\omega_i\}$ of the various possible vacancy jumps in the vicinity of A, that is, $f_{AV} = f_{AV}(\omega_i)$, and the correlation factor will be temperature dependent.

For Si *self*-diffusion via interstitials and vacancies, $D_{Si}^{self} = f_V^{self} C_V^* D_V + f_I^{self} C_I^* D_I$, where the correlation factors are purely geometric, $f_V^{self} = 1/2$ and $f_I^{self} = 0.73$, respectively.

D_{AX} if point defect concentrations are perturbed. For example, excess interstitials can be introduced by implantation of ions (impurities or Si atoms), and the growth of an oxide, SiO_2, or a nitride, Si_3N_4, causes an injection of interstitials and vacancies, respectively. Such phases are grown from the Si surface if annealing in, e.g., O_2, H_2O, or NH_3 ambiences.

Inserting (2.8) into (2.7) gives

$$D_A = \left[D_A^* \frac{C_{AI}}{C_{AI}^*}\right] f_{AI} + \left[D_A^* \frac{C_{AV}}{C_{AV}^*}\right] f_{AV} \tag{2.9}$$

and the reasonable approximation [13] can be made that

$$D_A = \left[D_A^* \frac{C_I}{C_I^*}\right] f_{AI} + \left[D_A^* \frac{C_V}{C_{V^*}}\right] f_{AV} \tag{2.10}$$

$$\equiv D_{AI} f_{AI} + D_{AV} f_{AV}. \tag{2.11}$$

This equation quantifies the fractional interstitial and vacancy components of diffusion. In thermal equilibrium the equation becomes trivial, but by deliberately introducing point defect *supersaturations* $C_X/C_X^* \neq 1$, bounds can be made on f_{AI} and f_{AV}. This requires either conservative assumptions on the supersaturations, such as, e.g., $1 \leq C_I/C_I^*$, $0 \leq C_V/C_V^* \leq 1$ under interstitial injection [13], or more restrictive assumptions [13, 15, 9, 10] can be made to obtain tighter bounds on f_{AI} and f_{AV}.

In the above manner, it is found that **group-III elements** (B, Al, Ga, In) diffuse primarily via an interstitial-related mechanism [9]. For B,

$$0.97 \leq f_{BI} \leq 1, \tag{2.12}$$

$$0.98 \leq f_{BI} \leq 1 \tag{2.13}$$

were measured at 1000 °C [13], and at ∼ 800 °C [15], respectively. It has further been demonstrated elegantly [16, 17] that B possesses an intermediate, mobile species, that is, BI or B_i of Eqs. (2.6), (2.6′). For **group-V elements** a transition from an interstitial-related to a vacancy mechanism is observed with increasing atomic size:

$$0.96 \leq f_{PI} \leq 1, \tag{2.14}$$

$$0.35 \leq f_{AsI} \leq 0.55, \tag{2.15}$$

$$0 \leq f_{SbI} \leq 0.02 \tag{2.16}$$

have been estimated at 1000 °C [13], and

$$0 \leq f_{SbI} \leq 0.012 \tag{2.17}$$

has been estimated at ~ 800 °C [15]. The latter trend holds also for **group-IV elements**, since

$$f_{\mathrm{Si}I} \approx 0.50\text{–}0.61 \tag{2.18}$$

was measured [18] in the 800–1100 °C range (with a slight decrease of $f_{\mathrm{Si}I}$ with temperature),[9] but

$$f_{\mathrm{Ge}I} \approx 0.3\text{–}0.4, \tag{2.19}$$

$$f_{\mathrm{Sn}I} \approx f_{\mathrm{Sb}I} \ \ (\approx 0) \tag{2.20}$$

at 1050 °C [20] and 1000 °C [21], respectively.

It is commonly assumed that the growing dominance of a V mechanism with increasing atomic size (covalent radius) is due to the increase of the dopant–vacancy attraction for reasons of local stress relief. Whereas this may be true for group-IV and group-V elements, it must be realized that the answer why an I-related mechanism prevails for group-III atoms of all sizes is not agreed upon.

Finally, examples of direct-interstitial diffusers in Si are Li, Na, Ar, He, and H. Most of the transition metals diffuse via the direct-interstitial or a kickout mechanism (see, e.g., refs. in Ref. [22]). Elements such as Au, Pt, S, Cu, and Zn are mainly substitutionally dissolved, but they diffuse as interstitial defects via a kickout mechanism or the dissociative mechanism. Their diffusion properties can be used to extract formation and migration energies of the native point defects in Si [19] and Ge [23].

2.2 Native point defects and their interaction with dopants

It is clear from Sec. 2.1.3 that native point defects play a crucial role in diffusion problems. The 'active' region of a semiconductor, whether in the context of devices or research, is rarely more than a few μm beneath the surface. Hence, the thermal-equilibrium concentrations C_V^* and C_I^* of vacancies and Si self-interstitials are maintained by surface generation and annihilation [10][10]. The surface generation of point defects is called the *Schottky process*, wherein

[9] This result ($f_{\mathrm{Si}I} \approx 0.50$–$0.61$), obtained from injection experiments on Si isotope structures [18], deviates from the results from metal diffusion via the dissociative mechanism. The latter experiments [19] indicate instead a changeover with temperature of the Si self-diffusion mechanism; e.g., $f_{\mathrm{Si}I}(800\ ^\circ\mathrm{C}) \approx 0.15$ and $f_{\mathrm{Si}I}(1100\ ^\circ\mathrm{C}) \approx 0.75$.

[10] We note that it has been suggested [24] that Si self-interstitials in *Czochralski* Si substrates are supplied primarily from the bulk, from oxygen precipitation, such that C_I^* is attained more rapidly than in *floatzone* Si.

H_V^{f} (eV)	H_I^{f} (eV)	$S_V^{\mathrm{f}}\,(k)$	$S_I^{\mathrm{f}}\,(k)$	Ref.
~ 2.0	3.18 ± 0.15	~ 1	4.1 ± 1.3	Experiment, Ref. [19]
2.6	3.8	2.9	9.9	Experiment, Refs. in [9]
3.57–3.69	3.23–3.71			Theory, Refs. [26,27,28,29]

Table 2.1: Formation enthalpies and entropies for the Si vacancy and self-interstitial.

vacancies and self-interstitials are created *independently* of each other (as opposed to the bulk Frenkel-process, $0 \rightarrow I + V$). The defect concentrations are obtained from statistical mechanics. Operating at constant pressure, one minimizes Gibbs' free energy of the crystal and finds, at low defect concentrations $C_X \ll C_S$ (See, e.g., Ref. [25]),

$$\frac{C_X^*}{C_S} = z_X \exp\left(-\frac{\Delta G_X^{\mathrm{f}}}{kT}\right) = z_X \exp\left(\frac{\Delta S_X^{\mathrm{f}}}{k}\right) \exp\left(-\frac{\Delta H_X^{\mathrm{f}}}{kT}\right) \tag{2.21}$$

where ΔG_X^{f}, ΔH_X^{f}, and ΔS_X^{f} are, respectively, Gibbs' free energy, the enthalpy, and the entropy changes related to the formation of one defect X. ΔS_X^{f} has a configurational contribution (mixing entropy) and a vibrational contribution that arises from a change in the lattice vibrational frequency spectrum in the vicinity of X; $\Delta S_X^{\mathrm{f}} = \Delta S_X^{\mathrm{f,m}} + \Delta S_X^{\mathrm{f,v}}$. The degeneracy z_X is the number of equivalent, distinguishable configurations that X can take (per lattice site); for a given lattice site at most one of those z_X configurations that are associated with it can be occupied with a defect at any time. C_S is the concentration of lattice sites; for Si, $C_S = 5 \times 10^{22}$ cm^{-3}.

Selected values related to point defect formation in Si are given in Tab. 2.1. For the vacancy formation enthalpy, it appears that consensus does not yet exist between experiment and theory.

The thermal-equilibrium concentration of impurity–point defect pairs, as formed in reactions (2.4) or (2.6), is given by

$$C_{AX}^* = z_{AX} \frac{C_X' C_{A_{\mathrm{s}}}}{C_S} \exp\left(\frac{\Delta G_{AX}^{\mathrm{b}}}{kT}\right), \tag{2.22}$$

where $\Delta G_{AX}^{\mathrm{b}}$ is the A–X binding energy and C_X' is the concentration of point defects that are not associated with dopants. z_{AX} is the number of different ways that the pair can form. In the general case, we can not expect that $C_{AX}^* \ll C_A$, and therefore we might have $C_{A_{\mathrm{s}}} \neq C_A$. A rigourous analysis [11] gives

the general Fermi-Dirac type expression

$$C^*_{AX} = \frac{zC_A}{\exp\left(\frac{\Delta G^{\mathrm{f}}_{AX}}{kT}\right) + z} \tag{2.23}$$

with $z = z_X z_{AX}$. $\Delta G^{\mathrm{f}}_{AX}$ is the formation energy of the AX complex. To be precise, $\Delta G^{\mathrm{f}}_{AX}$ is the energy required to bring X from the surface to its final position in the AX configuration in the bulk, i.e., $\Delta G^{\mathrm{f}}_{AX}$ is the formation energy of X less the A–X binding energy:

$$\Delta G^{\mathrm{f}}_{AX} = \Delta G^{\mathrm{f}}_{X} - \Delta G^{\mathrm{b}}_{AX}. \tag{2.24}$$

If the pair formation energy is several kT (e.g., $kT = 0.101$ eV at 900 °C), then (2.23) reduces to (2.22) if the approximations $C'_X \approx C^*_X$ and $C_{A_\mathrm{s}} \approx C_A$ are used in (2.23). The first approximation states that most point defects are not associated with defects, but at high concentrations of A this approximation can easily be violated if the A–X binding energy is large.

2.3 Dopant diffusion in the extrinsic regime

We have neglected, up to now, that point defects can exist in different charge states as long as overall charge neutrality is fulfilled. The formation energies, from the principle of energy balance, will depend on the *energy level* in the band gap of the particular defect. For example, in the reaction $X^- + e^- \rightarrow X^=$ we will denote by $E_{X^=}$ the energy gain of capturing an electron from the conduction band to the (initially) singly charged defect X^-. One finds, if assuming defects with five stable charge states:

$$C_{X^0} = z_{X^0} \exp\left(\frac{S^{\mathrm{f}}_{X^0}}{k}\right) \exp\left(-\frac{H^{\mathrm{f}}_{X^0}}{kT}\right) \tag{2.25}$$

$$C_{X^-} = C_{X^0} \frac{z_{X^-}}{z_{X^0}} \exp\left(-\frac{E_{X^-} - E_{\mathrm{F}}}{kT}\right) = C_{X^0}\, \delta^- \left(\frac{n}{n_{\mathrm{i}}}\right) \tag{2.26}$$

$$C_{X^=} = C_{X^0} \frac{z_{X^=}}{z_{X^0}} \exp\left(-\frac{E_{X^=} + E_{X^-} - 2E_{\mathrm{F}}}{kT}\right) = C_{X^0}\, \delta^= \left(\frac{n}{n_{\mathrm{i}}}\right)^2 \tag{2.27}$$

$$C_{X^+} = C_{X^0} \frac{z_{X^+}}{z_{X^0}} \exp\left(-\frac{E_{\mathrm{F}} - E_{X^+}}{kT}\right) = C_{X^0}\, \delta^+ \left(\frac{p}{n_{\mathrm{i}}}\right) \tag{2.28}$$

$$C_{X^{++}} = C_{X^0} \frac{z_{X^{++}}}{z_{X^0}} \exp\left(-\frac{2E_{\mathrm{F}} - E_{X^{++}} - E_{X^+}}{kT}\right) = C_{X^0}\, \delta^{++} \left(\frac{p}{n_{\mathrm{i}}}\right)^2 \tag{2.29}$$

Here, n, p, and n_i are the usual carrier densities, and E_F is the Fermi level.[11] For the right-hand side equalities we have defined the δ's by, e.g.,

$$\delta^{=} = C_{X^0}\frac{z_{X^=}}{z_{X^0}}\exp\left(-\frac{E_{X^=}+E_{X^-}-2E_\mathrm{i}}{kT}\right), \tag{2.30}$$

and we have used the relation $n/n_\mathrm{i} = \exp[-(E_\mathrm{i}-E_\mathrm{F})/kT]$, valid in Boltzmann statistics. In these relations, E_i is the intrinsic value of E_F.

These equations show that negatively charged point defects will dominate in n-type material and vice versa in p-type. One therefore defines the *extrinsic regime* as that where chemically active dopants cause a change of charged point defect concentrations, i.e. where N_D or $N_\mathrm{A} \gtrsim n_\mathrm{i}$.

Relative concentrations of charged vacancies[12] in Si at room temperature and at a typical diffusion temperature are given in Fig. 2.3. When the band gap shrinks with temperature [$E_G(1400\,\mathrm{K}) = 0.6\,\mathrm{eV}$], according to Van Vechten [32], acceptor levels tend to be pinned relative to the conduction band, whereas donor levels will follow the valence band. However, no reliable experimental information exists on energy levels in the high-temperature band, thus, Fig. 2.3 should primarily be considered for its qualitatively picture of the scaling of vacancy concentrations.

To describe the most commonly assumed model of dopant diffusion in the extrinsic regime, we will sketch the derivation by Fahey, Griffin, and Plummer [9]. The task is to put the relevant physics (i.e., rate equations and driving forces) into the flux equation (2.1),

$$J_A = -D_A\frac{\partial C_A}{\partial x}$$

and derive a general expression for D_A. But if we assume, as an example, that the extrinsic condition is brought about by n-type doping, it turns out that the diffusivity takes a more convenient and transparent form D' if one solves instead the equation

$$J_A = -D'_A\frac{\partial C_{A_\mathrm{S}^+}}{\partial x}. \tag{2.31}$$

[11] Strictly speaking, E_F is the *chemical potential*. Conventionally (e.g., in a metal), the Fermi level is defined as the energy level that separates the occupied and the unoccupied one-electron levels when the material is in its ground state. But with this definition, any energy in the band gap would be a 'Fermi level'.

[12] The levels of the single *vacancy* at low temperature are fairly reliably known from DLTS, they are given in the caption of Fig. 2.3. V^+ and V^{++} constitute an Anderson negative-U system [30,5], thus, V^{++} is in fact favoured over V^+. Unlike the vacancy, the *self-interstitial* does not appear after low-temperature irradiations and therefore, the associated levels are not known with certainty [9,10]. In p-type Si, it is possible that the self-interstitial does not appear because it migrates athermally to traps already at liquid-He temperatures. In n-type Si, the appearance of an interstitial-C ($\mathrm{C_i}$) signal at $\sim$ 150 K [31] is possibly an indication that the self-interstitial has become mobile at this temperature, yet, as said, the associated levels are not known.

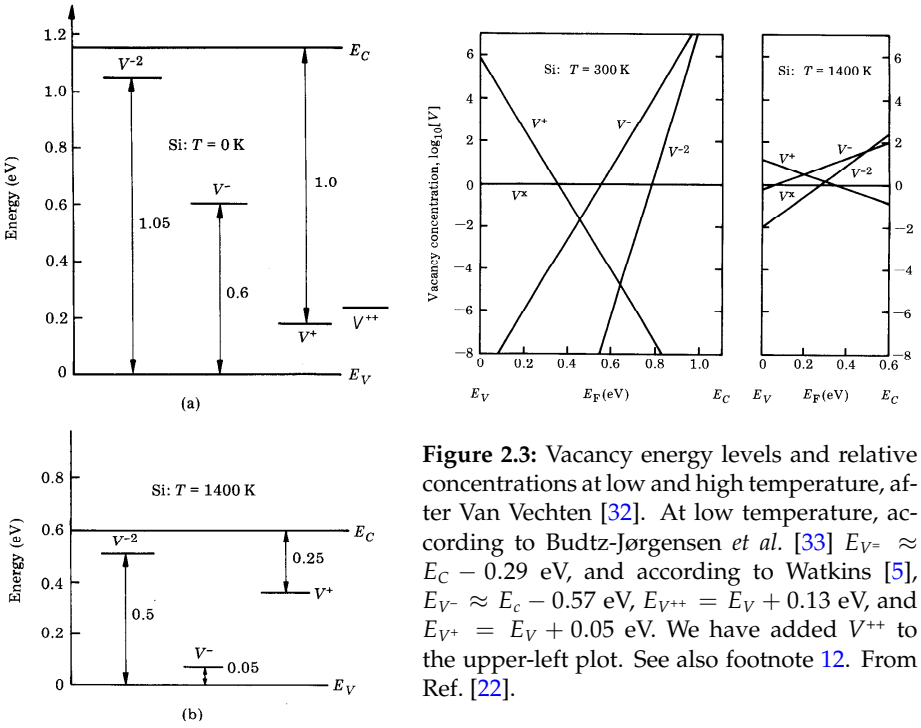

Figure 2.3: Vacancy energy levels and relative concentrations at low and high temperature, after Van Vechten [32]. At low temperature, according to Budtz-Jørgensen *et al.* [33] $E_{V^=} \approx E_C - 0.29$ eV, and according to Watkins [5], $E_{V^-} \approx E_c - 0.57$ eV, $E_{V^{++}} = E_V + 0.13$ eV, and $E_{V^+} = E_V + 0.05$ eV. We have added V^{++} to the upper-left plot. See also footnote 12. From Ref. [22].

This equation is usually a good approximation to (2.1), the requirement being that only a small fraction of dopants are associated with a point defect. For clarity we have used the notation $C_{A_s} \equiv C_{A_s^+}$. For charge states $q = (0, -, =)$ we can foresee the reactions

$$A_s^+ + X^q \rightleftarrows A^+X^q, \tag{2.32}$$

such that

$$C_{A_s^+X^q} = K(T) \times C_{A_s^+}C_{X^q} \tag{2.33}$$

[see Eq. (2.22)]. The total particle flux can be split into a sum of the different charge state contributions, $J_A = J_{A^+X^0} + J_{A^+X^-} + J_{A^+X^=}$. For each case $AX = A_s^+X^0, A_s^+X^-, A_s^+X^=$ we have

$$J_{AX} = -d_{AX}\frac{\partial C_{AX}}{\partial x} + Z_{AX}\mu_{AX}C_{AX}\mathcal{E}. \tag{2.34}$$

The last term is a *drift term* which arises from the electric field that is created by

a gradient in the $E_F - E_i$ and, hence, a gradient in $\ln(n/n_i)$:

$$\mathcal{E} = -\frac{kT}{q}\frac{\partial}{\partial x}\ln\left(\frac{n}{n_i}\right). \tag{2.35}$$

$Z_{AX} = e(1+q)$ is the charge of the mobile pair, and the mobility μ_{AX} is linked to the diffusivity through the Einstein relation

$$\mu_{AX} = \frac{ed_{AX}}{kT}. \tag{2.36}$$

Carrying out the partial derivations, one arrives at the rather simple overall flux equation:

$$\boxed{J_A = -h\left[D^i_{A^+X^0} + D^i_{A^+X^-}\left(\frac{n}{n_i}\right) + D^i_{A^+X^=}\left(\frac{n}{n_i}\right)^2\right]\frac{\partial C_{A_s^+}}{\partial x}.} \tag{2.37}$$

Eq. (2.37) is often denoted the *Fair model* [34]. (See also the comments to this model in Sec. 11.3.) We see that diffusion under extrinsic conditions is enhanced over that in the intrinsic regime. This is due to (i) a Fermi-level rise that influences n/n_i, and (ii) the factor h which is the *electric field-enhancement*:

$$h = 1 + \frac{\frac{C_{A_s^+}}{2n_i}}{\sqrt{\left(\frac{C_{A_s^+}}{2n_i}\right)^2 + 1}}. \tag{2.38}$$

This factor takes on values between 1 and 2, going from the intrinsic to the far-extrinsic case. The D^i_{AX} coefficients in (2.37) are the *intrinsic diffusion components* under equilibrium conditions. For example,

$$D^i_{A^+X^-} = d_{A^+X^-}\frac{C^i_{A^+X^-}}{C_{A_s^+}}, \tag{2.39}$$

and similar expressions apply for $D^i_{A^+X^0}$ and $D^i_{A^+X^=}$.

We have kept a rather precise notation throughout, and a manifold of superscripts and subscripts has been used. The following equation, (2.40), might be of some help to the reader. First, we point out that under intrinsic conditions the thermal-equilibrium quantity C^*_{AX} will be equal to C^i_{AX}, and that most frequently, $C_A \approx C_{A_s}$. Then we can demonstrate the following link:

$$D^*_{AX} \equiv \underbrace{D^*_A f_{AX} = d_{AX}\frac{C^*_{AX}}{C_A}}_{\text{Eq. (2.8)}} \approx \underbrace{d_{AX}\frac{C^i_{AX}}{C_{A_s}} = D^i_{AX}}_{\text{Eq. (2.39)}} \tag{2.40}$$

It is realized from (2.39) that each of the D^{i}_{AX} coefficients must be thermally activated. Hence, the impurity diffusion coefficient that was defined in Eq. (2.31) can in general be written on the form

$$D'_A = h\left[D_{\mathrm{x}}\exp\left(-\frac{Q_{\mathrm{x}}}{kT}\right) + D_{-}\exp\left(-\frac{Q_{-}}{kT}\right)\left(\frac{n}{n_{\mathrm{i}}}\right) + D_{=}\exp\left(-\frac{Q_{=}}{kT}\right)\left(\frac{n}{n_{\mathrm{i}}}\right)^2\right], \tag{2.41}$$

where the Q's are activation energies of diffusion for the different charge-state contributions (Sec. 2.4).

In practice, in intrinsic material over large temperature spans, diffusivities are often well described by a *single* Arrhenius expression with no break in the $\log D$-vs. $1/T$ plot. This is either because one term in Eq. (2.41) dominates over the others, or it is due to the inherent 'deceitful' nature of Arrhenius plots. Several extrinsic-doping experiments have been dedicated to the separation of the individual terms in (2.41). But contrary to what is sometimes assumed, *with the best of our belief, unambiguous evidence has not been presented for the existence of an $(n/n_i)^2$ or $(p/n_i)^2$ term for any group-V or group-III dopant in Si*. For group-V dopants, a linear n/n_i behaviour seems well established [35, 36] and can be followed up to the $\sim 2\times10^{20}$-cm^{-3} doping level. But above this level, *collective phenomena* set in [37] and further accelerate the diffusion, and it is not evident that an $(n/n_{\mathrm{i}})^2$ term [34, 38, 39] is needed to account for the concentration dependence. In Ge, on the other hand, As diffusion was recently seen to be enhanced more strongly than n/n_{i} already at very low concentrations $C_{\mathrm{As}} \lesssim 10^{19}$ cm^{-3} [40].

2.4 Activation energies of diffusion

2.4.1 Self-diffusion

Let us keep in mind that point defects (X) can exist in different charge states. The self-diffusion activation enthalpies[13] are given by

$$Q^{\mathrm{self}}_{X^0} = H^{\mathrm{f}}_{X^0} + H^{\mathrm{m}}_{X^0} \tag{2.42}$$

$$Q^{\mathrm{self}}_{X^-} = H^{\mathrm{f}}_{X^-} + H^{\mathrm{m}}_{X^-} = H^{\mathrm{f}}_{X^0} + [E_{X^-} - E_{\mathrm{F}}] + H^{\mathrm{m}}_{X^-} \tag{2.43}$$

$$\vdots$$

where the formation enthalpies $H^{\mathrm{f}}_{\mathrm{X}}$ are deduced from Eqs. (2.25–2.29) and $H^{\mathrm{m}}_{\mathrm{X}}$ are the migration enthalpies. We stress here that even if self-diffusion experiments are carried out under intrinsic conditions, it is *not* certain which is the

[13] Though somewhat sloppy, activation enthalpies are most commonly referred to as 'activation energies'.

B[(81)] 3.25–3.51[a]		
Al[(125)] 3.36[a]	Si[(117)] 4.75[b] 4.76[g] 4.1–4.2[c1] 4.8–5.1[c2]	P[(110)] 3.51–3.67[a]
Ga[(125)] 3.75[a]	Ge[(122)] 5.33[h] 3.92[i1] 4.97[i2]	As[(121)] 4.1–4.3[a]
In[(150)] 3.60[a]	Sn[(140)] 4.91[d] 4.8[e]	Sb[(141)] 3.9–4.1[a] 4.08[f]
		Bi[(146)] 4.12[a]

Table 2.2: Measured activation energies of diffusion under intrinsic conditions in eV. The dominant mechanisms are indicated: Vacancy, mixed, or interstitial--related. The covalent radii of the elements in pm are given in parentheses.
[a] Refs. in Fahey *et al.* [9], p. 320.
[b] 850–1400 °C, Bracht *et al.* [41]
[c1] T $\lesssim$ 1100 °C, Refs. in Hu [10], p. 111
[c2] T $\gtrsim$ 1100 °C, Refs. in Hu [10], p. 111
[d] Kringhøj *et al.* [42]
[e] Kringhøj *et al.* [21]
[f] Nylandsted Larsen *et al.* [43]
[g] Ural *et al.* [18]
[h] 876–1388 °C, Dorner *et al.* [44]
[i1] 855–1000 °C, Hettich *et al.* [45]
[i2] 1030–1302 °C Hettich *et al.* [45]

dominating (lowest-energy) charge state of the point defects; see Fig. 2.3 and accompanying discussion. Unfortunately, due to this shortcoming of knowledge it is not uncommon practice to fully neglect the distinction between point defect charge states.

Selected measured activation energies of diffusion are given in Tab. 2.2. A number of experiments have indicated that Si self-diffusion proceeds mainly via vacancies below $\sim$ 1100 °C, with Q_V^{self} = 4.1–4.2 eV, and via interstitials above $\sim$ 1100 °C, with Q_I^{self} = 4.8–5.1 eV (see refs. in Hu [10], p. 111). In consistency with these observations, first-principles calculations have lead to $Q_V^{\text{self}} = 4.0, 4.2$ eV [46, 47]. From analysis of zinc diffusion profiles [19], $Q_V^{\text{self}} = 3.80$ eV and $Q_I^{\text{self}} = 4.95$ eV were extracted. In a recent isotope diffusion experiment [41], there was *no* break in the Arrhenius plot; a single activation energy $Q^{\text{self}} = 4.75$ eV described self-diffusion from $\sim$ 850 to 1400 °C. But the data could be reconciled with the aforementioned since, by subtracting the D_I^{self}-values obtained from zinc-diffusion [19], only D_V^{self} remained and thus, $Q_V^{\text{self}} = 4.14$ eV was obtained. From this data it was suggested that the interstitial domination over vacancies in self-diffusion begins already at $\sim$ 890 °C.

However, in remarkable opposition to the metal-diffusion experiments are the results of the injection experiment that was very recently conducted by Ural *et al.* [18] on Si isotope-structures. This experiment revealed *equal I* and *V* contributions to self-diffusion, $f_V^{\text{self}} \approx f_I^{\text{self}}$, in the temperature range from 800 °C to 1100 °C, and it was concluded that $Q_V^{\text{self}} = 4.86$ eV and $Q_I^{\text{self}} =$

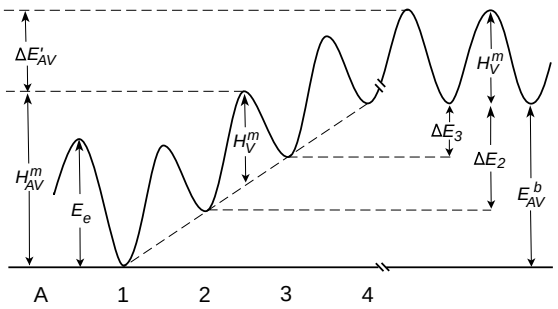

Figure 2.4: Vacancy potential as a function of neighbour distance from dopant atom, as assumed by Hu [48, 49] and by Dunham and Wu [50]. Binding energies in 1st, 2nd, and 3rd neighbour separations are, respectively, $\Delta E_1 \equiv E^{\mathrm{b}}_{AV}$, ΔE_2, and ΔE_3. E_{e} is the A–V exchange barrier.

4.68 eV. See also the comments following Eq. (2.18).

Many indications exist that *Ge* diffusion in Si is reminiscent of self-diffusion in Si, as is indeed expected from the similarity of the two atoms. Injection experiments [20] show that the mechanism has both I and V contributions. As in the case of Si self-diffusion, Ge diffusion coefficients have either displayed a break in the Arrhenius plots near 1000 °C [45], or the data could be fitted with just one activation energy from 876–1388 °C. [44]. The discrepancy between these findings is not well understood.

2.4.2 Impurity diffusion

Now consider diffusion via a reaction of the type $A_{\mathrm{s}} + X \rightleftarrows AX$. As a special case of (2.7), we can write

$$D_A = d_{AX}\frac{C_{AX}}{C_A}. \tag{2.44}$$

Since d_{AX} and C_{AX} are thermally activated, we can put D_A on the form $D_A(T) = D^0_{AX}\exp(-Q_{AX}/kT)$ where the measured activation enthalpy of diffusion is the sum of the *migration enthalpy* and the *formation enthalpy* of the diffusing complex:

$$Q_{AX} = H^{\mathrm{m}}_{AX} + H^{\mathrm{f}}_{AX}. \tag{2.45}$$

2.4.3 Vacancy mechanism

It was mentioned in Sec. 2.1.2 that in-between progressive diffusion steps the vacancy must migrate to a 3nn distance from the dopant atom. For illustration, we will use the linear dopant–vacancy potential of Fig. 2.4, as applied originally by Hu [48, 49]. H^{m}_V in the figure is the migration enthalpy for Si self-diffusion via vacancies, i.e. it is the Si–V exchange barrier. H^{m}_{AV} is the migration enthalpy for the AV complex, i.e. it is the highest barrier (the saddle

point energy) that the vacancy must surmount in the course of each diffusion step.

The activation energy of diffusion for an AV pair can be decomposed as

$$Q_{AV} = \underbrace{H_V^{\mathrm{f}} - E_{AV}^{\mathrm{b}}}_{H_{AV}^{\mathrm{f}}} + H_{AV}^{\mathrm{m}} \tag{2.46}$$

where the brace contains the effective formation enthalpy of a vacancy in a 1nn position to A. We will denote by $\Delta E'_{AV}$ the size of the A–V attraction when the vacancy is at the saddle point of the diffusion event. $\Delta E'_{AV}$ is indicated in Fig. 2.4 We can then write

$$Q_{AV} = \underbrace{H_V^{\mathrm{f}} - \cancel{E_{AV}^{\mathrm{b}}}}_{H_{AV}^{\mathrm{f}}} + \underbrace{H_V^{\mathrm{m}} + \cancel{E_{AV}^{\mathrm{b}}} - \Delta E'_{AV}}_{H_{AV}^{\mathrm{m}}} \tag{2.47}$$

The two expressions (2.46) and (2.47) are quite general,[14] but for the particular, linear potential of Fig. 2.4, $\Delta E'_{AV} = (\Delta E_2 + \Delta E_3)/2$ [50] (and not ΔE_3 as originally assumed by Hu [48]).

Eq. (2.47) provides a fundamental link between the activation energy of impurity diffusion and that of self-diffusion. For completeness, let us allow for specific charge states of the AV pair. In that case, Eq. (2.47) predicts that the activation energy of impurity diffusion via the E center mechanism should be lower than that of vacancy-mediated self-diffusion via the same charged point defect:

$$Q_{A^+V^0} = Q_{V^0}^{\mathrm{self}} - \Delta E'_{A^+V^0} \tag{2.48}$$

$$Q_{A^+V^-} = Q_{V^-}^{\mathrm{self}} - \Delta E'_{A^+V^-} \tag{2.49}$$

$$\vdots$$

The potential diagram of Fig. 2.4 formed the basis of lattice Monte-Carlo simulations [50]. Although these simulations gave a good reproduction of the high-concentration diffusion of As and P (see also Chap. 5), recent total-energy calculations by Pankratov *et al.* [27] revealed a somewhat different shape of the donor atom–vacancy potential. The calculations were performed for As, and the result is shown in Fig. 2.5. As is more or less customary in supercell calculations, a charge-neutral pair (As^+–V^-) was assumed. It is particularly worth

[14] In Eq. (2.47) we implicitly assume that the A–V exchange barrier E_{e} is small. Were this not the case, the migration barrier would be given instead by $H_{AV}^{\mathrm{m}} = E_{\mathrm{e}}$. As an example, B has a very high barrier for interchange of position with a vacancy: $E_{\mathrm{e}}(\mathrm{B}V)$ = 2.49 eV [26]. Combining with the small binding energy, $E_{\mathrm{B}V}^{\mathrm{b}} = 0.17$ eV [26], it can be understood why B does not diffuse via vacancies.

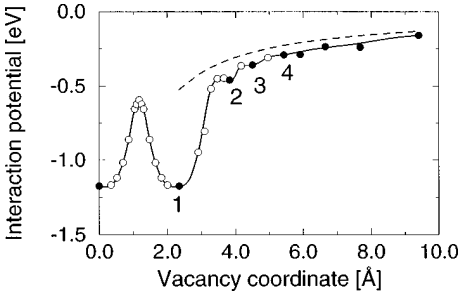

Figure 2.5: As^+–V^- interaction potential, from density-functional theory. The binding energies are $E^b \equiv \Delta E_1 = 1.17$ eV and $\Delta E_3 = 0.36$ eV. The dashed line is the screened Coulomb potential $V_{Coul}(r) = 1/\epsilon_0 r$ ($\epsilon_0 = 11.7$ for Si). From Pankratov *et al.* [27].

noticing that the potential asymptotically approaches that of a long-ranged, screened coulomb potential. This has important implications since the A^+–V^- potentials from separate donor atoms will overlap at very high donor concentrations, as will be discussed in Chaps. 4 and 5. Interestingly also, there is almost no barrier for vacancy jumps from the 3nn to the 2nn position. We may therefore use the results of Pankratov *et al.* to extract, with the use of (2.47)

$$Q_{As^+V^-} = (H^f_{V^-} - E^b_{As^+V^-}) + (E^b_{As^+V^-} - \Delta E_3) \tag{2.50}$$
$$= 3.24 \text{ eV} + (E_{V^-} - E_i), \tag{2.51}$$

since they found $H^f_{V^0} = 3.6$ eV and $\Delta E_3 = 0.36$ eV. In comparison, Xie and Chen [28] calculate $Q_{AsV} = 3.56$ eV.

Measured activation energies of impurity diffusion in the intrinsic regime were listed in table 2.2. For diffusers with a large vacancy component (i.e., $Q_A \approx Q_{AV}$) we find $Q_A \approx 4.1$ eV in group V (As, Sb, Bi) and $Q_A \approx 4.9$ eV in group IV (Sn). The activation energy in Eq. (2.51) (see Fig. 2.3 and the associated discussion regarding the term $E^-_V - E_F$) falls slightly below the quoted experimental values. Thus, there is still a modest discrepancy between *ab initio* methods and experiment.[15] The discrepancy could, in principle, be reduced if one made the assumption that As diffusion is in reality dominated rather by As^+V^0 pairs: For this system, the interaction-potential would be weaker, $\Delta E'_{As^+V^0} < \Delta E'_{As^+V^-}$ (Fig. 2.4) and a higher activation energy would be calculated. However, at room temperature the E center has charge states (0) and (–), and it is *not* known to posses a (+) charge state.

A more fundamental inconsistency is noted: In Sec. 2.4.1, we cited typical activation energies of self-diffusion via vacancies, $Q^{self}_V \approx 4.1$ eV. But conversely to the prediction of Eqs. (2.48) or (2.49), the impurity-diffusion activation energies Q_{AV} in Tab. 2.2 are either comparable to or *higher* than Q^{self}_V.

[15] One should remember that As has a mixed I and V-mediated diffusion mechanism (p. 9). But since a break is not reported in the Arrhenius plots, and since the I and V contributions are comparable, one will suspect that $Q_{AsV} \approx Q_{AsI}$.

Again, if one made the assumption that impurity diffusion is primarily accounted for by neutral vacancies (A^+V^0), one could possibly accept, within experimental accuracy, that comparable activation energies are observed. But in particular, the large value of $Q_{\mathrm{Sn}} = 4.8$–4.9 eV [42, 21] still makes an incoherent picture: Since Sn is isoelectronic to Si, one would have expected that Q_{Sn} be comparable to or slightly smaller than Q_V^{self}, but certainly not larger, as experiment shows. The paradox could in principle have been resolved if a remarkably large Sn–V exchange barrier had existed (that is, $E_{\mathrm{e}} = 4.8$–4.9 eV see Fig. 2.4), but this is not the case: Watkins [51, 52] proposed that the Sn–V pair can easily flip from the E center configuration ($\mathrm{Sn_sV}$) to a configuration of D_{3d} symmetry, where the Sn-atom resides in a bond-centered position in-between two 'half-vacancies'. *Ab initio* calculations performed by this author[16] show that the 'Watkins configuration' is in fact the lowest-energy configuration with a total binding energy of 1.3 eV. The E center configuration has a higher energy of almost 0.7 eV relative to the Watkins configuration[17], but there is either very little or no barrier involved when the vacancy, to exchange sites with the Sn atom, goes from an E center configuration to the Watkins configuration. The calculations have very recently been reproduced by Kaukonen *et al.* [54] with density functional theory.

On the basis of these reflections, it is tempting to *reconsider* the accepted value of Q_V^{self}: As was already pointed out, one isotope-structure injection experiment [18] yielded values $Q_V^{\mathrm{self}} = 4.86$ eV and $Q_I^{\mathrm{self}} = 4.68$ eV. The possibility should therefore be borne in mind that other obtained values ($Q_V^{\mathrm{self}} \approx 4.1$ eV, $Q_I^{\mathrm{self}} \approx 4.9$ eV) could suffer from unfortunate experimental circumstances or from yet unclear artifacts of the analysis method (e.g. for metal-diffusion experiments).

2.4.4 Interstitial-related mechanisms

The **interstitialcy** kickout-type mechanism ($A_{\mathrm{s}} + I \rightleftarrows AI$) can be analysed in much the same way as the vacancy mechanism since the keystone is still the formation of an impurity–defect pair with a finite binding energy. We have

$$Q_{AI} = \underbrace{H_I^{\mathrm{f}} - E_{AI}^{\mathrm{b}}}_{H_{AI}^{\mathrm{f}}} + H_{AI}^{\mathrm{m}}. \tag{2.52}$$

[16] For the calculations, neutral SnV pairs were assumed and the VASP code was used (Vienna Ab-Initio Simulation Package [53]). The code is based on density-functional theory, and ultra-soft pseudopotentials are used in plane-wave basis sets. A 64-lattice site supercell and $4 \times 4 \times 4$ Monkhorst-Pack k-point sampling was employed. Same results were obtained whether the ions were relaxed via a quasi-Newton or a conjugate-gradient algorithm.

[17] Thus, one might even talk of a *negative* Sn–V exchange barrier, $\Delta E_{\mathrm{e}} = -0.7$ eV.

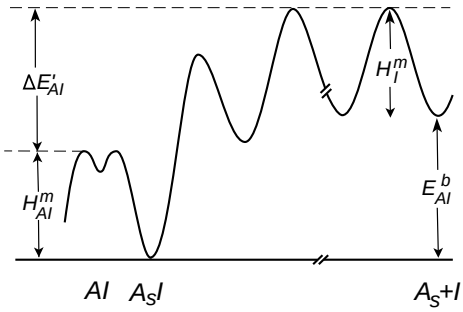

Figure 2.6: Schematic interaction potential between the silicon self-interstitial I and a dopant atom A.

H^{m}_{AI} is the migration energy of the diffusing pair, it is illustrated in Fig. 2.6. H^{m}_{AI} is the height of the saddle point that must be overcome when switching from the lowest-energy A_sI configuration to the AI local-minimum configuration. To closely parallel the vacancy mechanism analysis, we can even write

$$Q_{AI} = \underbrace{H^{\mathrm{f}}_I - \cancel{E^{\mathrm{b}}_{AI}}}_{H^{\mathrm{f}}_{AI}} + \underbrace{H^{\mathrm{m}}_I + \cancel{E^{\mathrm{b}}_{AI}} - \Delta E'_{AI}}_{H^{\mathrm{m}}_{AI}} \tag{2.53}$$

where the quantity $\Delta E'_{AI}$ is illustrated in Fig. 2.6. Since $Q^{\mathrm{self}}_I = H^{\mathrm{f}}_I + H^{\mathrm{m}}_I$, we can relate to the self-diffusion activation energy via interstitials:

$$Q_{AI} = Q^{\mathrm{self}}_I - \Delta E'_{AI}, \tag{2.54}$$

where $\Delta E'_{AI}$ was in fact defined by

$$\Delta E'_{AI} = E^{\mathrm{b}}_{AI} + (H^{\mathrm{m}}_I - H^{\mathrm{m}}_{AI}). \tag{2.55}$$

As can be seen in Tab. 2.2, experiments show that $Q_A \sim 3.5$ eV for diffusers with a predominantly interstitial-related mechanism (i.e., $Q_A \approx Q_{AI}$ or $Q_A \approx Q_{A_i}$; P, B, Al, In). Thus, the activation energies are lower than Q^{self}_I by almost 1.5 eV, and if these elements diffuse as interstitialcy defects, it means that $\Delta E'_{AI} \sim 1.5$ eV. Such a large value of $\Delta E'_{AI}$ will be owed, in part, to a substantial binding energy of the complex, E^{b}_{AI}. But the question which quantity is the larger of H^{m}_I and H^{m}_{AI} in Eq. (2.55) does not have a simple answer since there is no fundamental relationship that links the two.

One should recognize the significant difference from the E center mechanism that a large value of $\Delta E'_{AI}$ does *not* come about by requiring that the A–I binding is of long-range nature: On the contrary, the range of interaction is not of significance since, in the course of a diffusion step, A and I are separated at most $\sim$ half a neighbour distance.

As an example of interstitialcy-type diffusion, we plot in Fig. 2.7 an inter-

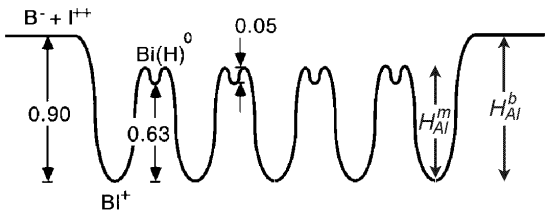

Figure 2.7: Calculated energies during migration of the Si self-interstitial and a boron atom (A–I = B$^-$–I^{++}), by Sadigh *et al.* [29]. Binding energy $H^{\rm b}_{AI} = 0.90$ eV, migration barrier $H^{\rm m}_{AI} = 0.68$ eV. After Ref. [29]

action potential diagram for the boron–self-interstitial pair, BI. The diagram was calculated from first principles with density functional theory (DFT) by Sadigh *et al.* [29]. They proposed that the BI defect, in the intrinsic regime, diffuses with lowest energy as a B$^-$–I^{++} pair. In each migration step the pair is suggested to change charge state and switch from substitutional $\mathrm{B_s^-}$ next to a tetrahedral $\mathrm{Si^{++}}$ self-interstitial ($\mathrm{B_s^-}I^{++}$) to interstitial $\mathrm{B_i}^0$ in a hexagonal position ($\mathrm{B_i^0Si^0}$). The calculated activation energy of diffusion, when we add the correction $E_{I^{++}}$ on the self-interstitial formation energy, is

$$
\begin{aligned}
Q_{\mathrm{B}^-I^{++}} &= H^{\rm f}_{I^{++}} - E^{\rm b}_{\mathrm{B}^-I^{++}} + H^{\rm m}_{\mathrm{B}^-I^{++}} && (2.56)\\
&= (3.23\ \mathrm{eV} + 2E_{\rm i} - E_{I^{++}} - E_{I^+}) - 0.90\ \mathrm{eV} + 0.68\ \mathrm{eV} && (2.57)\\
&= 3.01\ \mathrm{eV} + 2E_{\rm i} - E_{I^{++}} - E_{I^+}, && (2.58)
\end{aligned}
$$

only slightly lower than experiment.[18] Calculations such as these are complicated by the fact that many combinations of interstitial configurations and charge state must be probed [29] in order to find the most favourable. To our knowledge, first-principles calculations on other interstitial-related diffusers than B have not been performed.

For the **interstitial** kickout mechanism ($A_{\rm s} + I \rightleftarrows A_{\rm i}$), the usual definition applies:

$$
Q_{A_{\rm i}} = H^{\rm f}_{A_{\rm i}} + H^{\rm m}_{A_{\rm i}}. \qquad (2.59)
$$

A diagram similar to Fig. 2.6 for the interstitial*cy* mechanism can be constructed. However, the formation enthalpy $H^{\rm f}_{A_{\rm i}}$ of the interstitial impurity is no longer related to $H^{\rm f}_I$ by a simple binding-energy term, since $H^{\rm f}_{A_{\rm i}}$ accounts not only for the formation of self-interstitials, but also for the kickout displacement of $A_{\rm s}$ into interstitial $A_{\rm i}$. The migration energy $H^{\rm m}_{A_{\rm i}}$ is the barrier for jumps between interstices.

[18] Actually, 3.01 eV is obtained with the local-density approximation and 3.49 eV is obtained with the gradient-corrected approximation [29].

Chapter 3

Diffusion studies: Experimental aspects

A description is given of the experimental techniques that have been utilized in the diffusion studies. Emphasis is put on MBE sample fabrication, of central importance as it is, and on SIMS profiling, performed extensively by the author. RBS spectrometry and TEM microscopy are briefly described.

3.1 Molecular-Beam Epitaxy (MBE)

Overview

Epitaxy, in general, refers to any of several processes in which atoms are deposited on a crystalline substrate that acts as a seed, such that a thin film is grown with a specific lattice structure that is governed by that of the substrate. The term 'epitaxy' is adopted from Greek *epi*, meaning 'on' and *taxis*, meaning 'arrangement' or 'order', together: 'arranged upon'. Epitaxial techniques on Si, compared with ion implantation, offer unique control of the dopant chemical profiles (down to a few lattice constants) and also reduces problems of lattice damage. Recommendable reading on physical as well as technological issues of MBE is Kasper and Bean [55].

MBE is an ultra-high vacuum (UHV) process wherein beams of particles (atoms or molecules) impinge on a heated substrate. The incorporation of an element (Si or dopant) is determined by the particle flux ϕ, and the sticking coefficient s, which is the probability that the relevant atom, now in an adsorbed state, remains on the epilayer. From a molecular beam, ad-atoms can be formed when molecules decompose on the surface. The sticking coefficient depends on the competing processes of spontaneous desorption of the ad-atom, on the one side, and surface diffusion to kinks at terrace edges, or to other ad-atoms (island formation) where bonding reactions can take place, on the other side. At typical growth temperatures, $\sim$ 400–800 °C for Si MBE, the sticking coefficient for Si is near unity, $s_{\mathrm{Si}} \sim 1$ (hence the very low vapour pressure of Si). But for many dopants, such as Sb and Ga (Ref. [55], vol. I, p. 95) the sticking coefficient

is very small, $s \ll 1$, and it obeys a Boltzmann expression such that the higher the temperature, the lower the sticking coefficient.

For deposition from a thermal gas, the Maxwell-Boltzmann particle velocity distribution is relevant. It follows [56] that the incident flux of particles (molecules or atoms) is given by

$$\phi = p(2\pi mkT)^{-1/2} \tag{3.1}$$

where m and p is the mass and the partial pressure of the particles. The time t_1 to deposit a layer of N_1 atoms per unit area is then given by

$$t_1 = \frac{1}{sz}\frac{N_1}{\phi}. \tag{3.2}$$

where z is the number of atoms per molecule (e.g., $z = 2$ for H_2). Detrimental crystal contamination will result if residual gases deposit at a rate that is not negligible compared to the growth rate. For example, in a worst-case scenario ($s = 1$) one finds for residual CO that the time to deposit one monolayer of C at 1000 K (if we simply use the Si {001} surface atoms density, $N_1 = 6.79 \times 10^{14}$ cm^{-2}) is

$$t_1 \approx \begin{cases} 1 \text{ s} & \text{at } p = 10^{-6} \text{ Torr} \\ 3 \text{ h} & \text{at } p = 10^{-10} \text{ Torr.} \end{cases} \tag{3.3}$$

Since typical growth rates are in the range 0.1–10 Å/s, we see from Eq. (3.3) that the requirement of UHV is strict and nonnegotiable to avoid high contamination levels. And the lower the growth rate, the more critical is the vacuum. In the Aarhus MBE, dominant background gases are H_2, CO_2, CO, N_2, and H_2O, and the contamination levels of C and O are $\lesssim 10^{18}$ and 10^{16} cm^{-3}, respectively. Commercial bulk Si has C and O concentrations of 10^{16}–10^{17} and 10^{17}–10^{18} cm^{-3}, respectively; higher in Czochralski Si than in float-zone Si.

Concerning the growth temperature (i.e. substrate temperature), a high one can be chosen if the sticking coefficient and the flux of the dopant is sufficiently high. A high temperature is often desirable in order to achieve high crystalline quality with a small density of grown-in lattice imperfections. A high temperature also facilitates full relaxation in $Si_{1-x}Ge_x$ growths; more about this in Chap. 8. However, a compromise temperature must be found since dopant diffusion through the bulk must also be kept low.

Apparatus

The Aarhus MBE is a commercial VG-80 from VG Semicon. Wafers are loaded in a cassette into the preparation and storage chamber. In this chamber, surface contaminants such as H_2O, C, and B are outgassed with a low-temperature

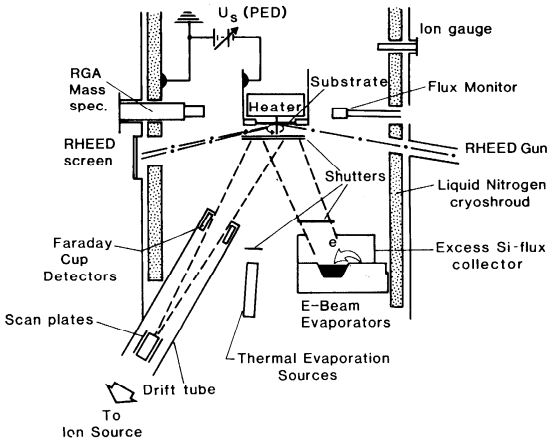

Figure 3.1: Schematic of a VG Semicon MBE deposition chamber. From Ref. [55].

(400 °C) bake. In the deposition chamber, the native SiO_2 on the wafer is then removed under a Si flux at 850 °C, by the formation of gaseous SiO via the reaction $Si + SiO_2 \rightarrow 2SiO$. The deposition chamber itself is depicted in Fig. 3.1 in schematic form. The walls of the chamber are cooled with liquid nitrogen to reduce their outgassing. The wafer is fixed to a substrate holder which is rotatable to ensure spatial homogeneity, and which is positioned underneath a graphite heater.

Elements are deposited from one of three different sources: (i) An *electron-beam* evaporator is used for Si and Ge. Here, an electron beam is steered onto a large, solid block of Si (or Ge) to induce a localized (few cm) heating and evaporation, at around 1700 °C for Si. The block is placed in a water-cooled Cu hearth. (ii) *Effusion cells* are used to thermally evaporate B, Sn, and Sb. Source materials elemental B, Sn, and Sb, respectively, are placed in a pyrolytic boron-nitride (pBN) crucible inside the cylindrically-shaped cell. The crucible is heated radiantly to temperatures of 1400–1900 °C (B), 1000–1200 °C (Sn), or 200–400 °C (Sb), and molecules evaporate into the chamber through a small-diameter aperture; hence the name 'effusion'. The desired flux is obtained by choice of temperature. (iii) A plasma *ion source* is used to obtain As and P doping. The ion source is fitted on a low-energy ion implanter that came in operation in the late fall of 1998. After ionization the beam is accelerated to ~ 10 keV and magnetically mass filtered. It is then passed through a set of deceleration plates and slowed to typically 0.5–1 keV, with which energy the beam is electrostatically bent into the deposition chamber and is scanned across the growing wafer. The sticking coefficient is essentially unity. Ion damage effects are partially self annealed, but a 'wind' of Si self-interstitials has been observed [57] to arise (since a deeper-lying B spike was broadened) during 1 keV As implantation to a 4×10^{20} cm^{-3} doping level. This wind, however, may be due either

to implantation damage or to complex formation [58, III]. In any case, formation of {311} defects [59, 60] should be considered as a possibility. Presently, P and As beam currents of ~ 30 μA can be achieved, giving a maximum doping level of $\sim 5 \times 10^{20}$ cm^{-3} at a 0.1-Å/s growth rate.

Notice that the mean free path at 10^{-10} Torr is hundreds of kilometers ([55], vol. I, p. 34). Therefore, from all of the above doping sources the dopants will flow in an unobstructed and non-viscous beam, and with shutters in front of each evaporation source, the beams can abruptly be switched on and off.

3.2 Secondary-Ion Mass Spectrometry (SIMS)

In SIMS, a *primary* ion beam of typical energy between 1 and 10 keV is rastered over a small region of the sample surface. A fraction of the resulting displacement cascade will overlap with the surface, and *secondary* ions are ejected with an energy peak distribution at less than 10 eV. The mass distribution of these ions is followed as a function of the sputtered depth; in practice as a function of time. For practical concerns on SIMS, refer to the handbook by Wilson, Stevie, and Magee [61], and for details on ion collisions and theory of sputtering yield see, e.g., Woodruff and Delchar [62] or Feldman and Mayer [63] and references therein. Useful SIMS resources are also found on the internet [64].

Sputtering parameters (i.e. primary ion species, beam energy E, and angle of incidence away from normal, θ) are chosen with the aim of obtaining high depth resolution and/or high dynamic range (peak-to-background intensity ratio) for a particular dopant. The latter is determined by the sputtering yield and the background counts. Below, a quick SIMS tutorial is given!

Sputtering yield

The *sputtering yield* can be defined and written as

$$Y(E) \equiv \frac{\text{no. of emitted ions}}{\text{incident particle}} \tag{3.4}$$

$$= \Lambda F_{\mathrm{d}}(E) \tag{3.5}$$

where $F_{\mathrm{d}}(E)$ is the deposited energy density and Λ collects material properties. For particles incident at keV energies, as in SIMS, sputtering yields $Y \sim 0.5$–20 are normal. MeV ions, used in Rutherford backscattering, have sputtering yields $Y \sim 10^{-3}$. According to Sigmund [65],

$$\Lambda = \frac{0.042}{N_{\mathrm{S}} U_0} \text{Å/eV}, \tag{3.6}$$

U_0 being the surface binding energy and N_S the matrix atomic density. The energy density may be written

$$F_d(E) = \alpha N_S S_n(E) \propto 1/\cos\theta. \tag{3.7}$$

$S_n(E)$ is the stopping power (– since sputtering is with low-energy ions, nuclear stopping dominates over electron stopping). The proportionality factor α increases with the mass ratio of the beam and target particles, M_b/M_t, and, as hinted in (3.7), α increases (roughly) as $1/\cos\theta$ since more energy is deposited at the surface for oblique bombardment. Therefore, fast sputtering is facilitated by high primary energy, high primary mass, and oblique incidence.

Experimentally, only ionized secondaries are collected. If impurity species i has partial sputtering yield Y_i (total number of sputtered i per primary particle), then the *positive secondary ion yield* of i is

$$Y_i^+ = \gamma_i Y_i, \tag{3.8}$$

where γ_i is the ionization efficiency of i. A similar relationship holds for Y_i^-. The variation of Y_i with element i (e.g., due to different surface binding energies), i = host or impurity atom, is the cause of transient, preferential sputtering. Implantation into the sample surface of *reactive primaries*, namely O or Cs, rather than noble-gas primaries, strongly enhances the ionization efficiency for electropositive and electronegative elements, respectively. Therefore, positive secondaries are emitted with an O_2^+ beam and negative secondaries are emitted with Cs^+. Y_i^+ and Y_i^- are matrix dependent, but they generally drop exponentially with respectively the ionization potential and the electron affinity of the element i (see Wilson *et al.* [61]). With O_2^+ primaries, Y_i^+ will generally decay with increasing values of θ since less surface oxide forms at oblique bombardment. Therefore, a high count rate can be at the price of depth resolution (see below).

Depth resolution

With present-day epitaxial techniques, layers can be embedded in Si with a sharpness of only few atomic layers; this sharpness exceeds the resolution that is obtainable with any profiling technique. A SIMS profile of a sharp delta layer will, in general, exhibit a rapid rise at the leading edge and a comparatively slow falloff at the trailing edge. An example (Sb in Si) is given in Fig. 3.2 The falloff of the count rate I on the trailing edge of the profile (the edge starting at x_0) is described by a decay length λ_d

$$I(x) \propto \exp\left(-\frac{x - x_0}{\lambda_d}\right) \tag{3.9}$$

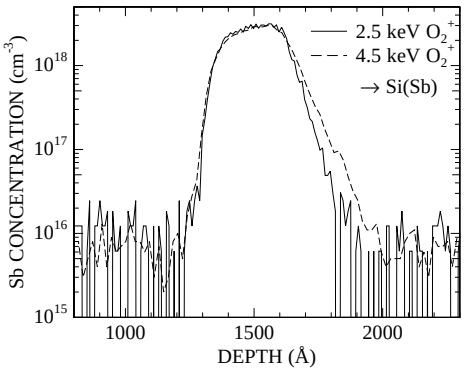

Figure 3.2: SIMS profiles of an Sb spike, obtained at two different primary ion energies at an incident angle of 20°. Absolute depth was not measured for the 2.5 keV profile; the SIMS spectrum was simply scaled by a factor to match the depth of the 4.5 keV profile.

and a similar expression applies for the rise on the leading edge, with up-slope parameter λ_u. The *rise* of the SIMS profile is only approximately described by the exponential dependence and the significance of λ_u is not well documented. λ_u has only little dependence on the dopant element but it is rather sensitive to initial and beam-induced surface roughness [66]. Regarding the *decay*, λ_d has a contribution λ_i from the physical (*i*ntrinsic) decay of the profile, and a contribution λ_b that is beam induced;

$$\lambda_d^2 = \lambda_i^2 + \lambda_b^2. \tag{3.10}$$

In general, λ_b is set by (i) ion-beam mixing and (ii) beam-induced change (roughening) of the surface morphology. λ_b will depend on the choice of primary beam, the host matrix, and the dopant species, and a small λ_d is obtained at low primary beam energy E and (usually) at high angle of incidence θ away from normal (grazing angle). As an example, the Sb structure that is shown in Fig. 3.2, sputtered at 20° off-normal with O_2^+, has $\lambda_u \approx 12$ Å for the up-slope, almost independent of energy, whereas the down-slope is given by $\lambda_d \approx 40$ and 58 Å, respectively, at 2.5 and 4.5 keV primary energy.

For a Si host matrix, surface roughening can be ignored in most cases. However, with a low-energy O_2^+ beam, rapid ripple growth will occur at oblique angles. For example, at $E = 1$ keV, B delta profiles are broadened due to this effect for ($\theta \geq 36°$), and as another consequence the sputtering rate becomes depth-dependent [67, 68]. With Cs^+ at $\theta \approx 23°$, surface roughening increases linearly with decreasing E such that decay lengths in P profiles were not reduced for $E < 2.5$ keV [69]. A surface roughening leads to a Gaussian broadening, the width of which grows linearly with average sputter depth [62].

Ion-beam mixing (generally thought to dominate over direct recoil implantation) provides a contribution to λ_b that will be independent of sputtered depth after an initial, transient period[19]. In the model of Zalm and

[19] In this transient surface region of ∼ 5–200 Å, depending on sputtering conditions (see, e.g.,

Vriezema [70] (neglecting surface roughening),

$$\lambda_b = \left(\frac{\mathcal{H} N_S^{1/3} U_0}{\langle \Delta H_{coh} \rangle^2} \right)^{1/2} \sqrt{E} \cos\theta, \tag{3.11}$$

where $\mathcal{H}$ is an efficiency of mixing, N_S is the host atomic density, U_0 is the surface binding energy, and $\langle \Delta H_{coh} \rangle$ is the weighted average over the cohesive energies of target and impurities. The $\sqrt{E}\cos\theta$ dependence has previously been predicted for cascade mixing [71], but two features are uniquely for the above model: (i) λ_b has no dependence on primary ion species and (ii) λ_b has only modest dependence on impurity type. Eq. (3.11) has good agreement with experiment for bombardment with $^{40}Ar^+$, $^{131}Xe^+$, and $^{133}Cs^+$ (see [70,72] and refs. therein), but for $^{16}O_2^+$ bombardment, superior depth resolution can be obtained. The latter observation has been related [72] to the well-known beam-induced oxidation ('swelling') of the Si surface and changes in chemical bond strength. A semiempirical correction factor can be attached to Eq. (3.11) [72,73]; this incorporates the fact that oblique angles of O_2^+ incidence result only in thin, non-stoichiometric oxides. It is found [74] that an O_2^+ beam induces significantly larger λ_d for Sb profiles than for B (and other) profiles at $\theta < 40°$. This may be caused by rapid redistribution of Sb within the thickness of the beam-induced oxide [74].

To minimize effects of finite depth resolution in diffusion studies, long diffusion lengths l [$\approx (2Dt)^{1/2}$] are desirable. But often, $\lambda_b \ll l$ cannot be achieved due to compromise between depth resolution and erosion rate. To minimize errors it is then crucial to use identical sputtering parameters for the as-grown and the diffused profile, as has been done throughout this work. If very precise knowledge of the profile is needed, methods of *deconvolution* can be applied [75,76].

Shifts of the apparent delta layer *peak position* x_{peak} can be caused by sputter-rate changes (due to the transient region or to beam-induced surface roughening [68,67]), preferential mass transport, or swelling of the matrix; see Ref. [75] and references therein. For a normal-incident O_2^+ beam, a B peak has a differential shift towards the surface of $\partial x_{peak}/\partial E \approx 10$–$13$ Å/keV [75,66], whereas the shift for an Sb spike is hardly detectable [75].

Ref. [68] and references therein), secondary-ion intensities have not yet equilibrated with dopant concentrations due to preferential sputtering yields. The transient region is critical primarily for profiling ultra-low energy implants, the demand of which is continually pushed to meet the Roadmap [2,3] requirements.

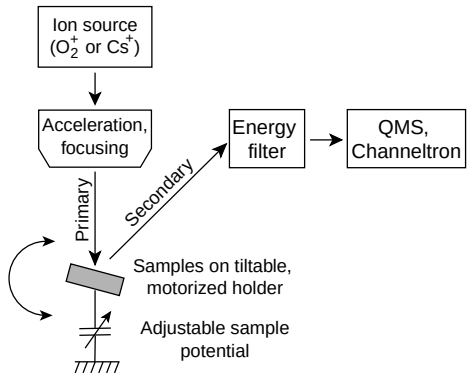

Figure 3.3: Schematic of the Atomika 4000 SIMS instrument

Instrumentation

Most measurements in this thesis were performed with the Atomika 4000 microprobe[20]at the Microelectronics Center (MIC), Technical University of Denmark (DTU). The instrument (schematic on Fig. 3.3) has two choices of primary beam: An O_2^+ beam can be produced from a duoplasmatron ion source that operates at a pressure of $\sim 2 \times 10^{-6}$ Torr, and a Cs^+ beam can be produced from a surface-ionization ion source. An accelerated and mass-filtered O_2^+ beam can be focused to a diameter of ~ 25 μm at typical operating conditions with primary beam energy 3.5 keV and current 100 μA. Rastered areas are square with typical side length 200–300 μm, and by means of electronic gating the lateral distribution of secondary-ion intensities can be obtained. Thus, from a given depth profile, different portions can be shown that were collected from central regions of various fractional sizes of the rastered area (the inner 25 % and less), and it is easily verified whether crater effects do not occur. The sputtered secondary ions are electrostatically energy-filtered and directed through a quadrupole mass spectrometer (QMS). In a QMS, the beam trajectory oscillates along the centerline of four parallel rods, and by proper combination of combined DC and RF potentials on the rods, only ions with a selected mass-to-charge (m/q) ratio will form a stable trajectory and be transmitted through the QMS, to the Channeltron detector. A QMS, compared with a double focusing instrument (electrostatic followed by magnetic deflection) has greater ease of use and almost instant switching between different masses (no magnetic hysteresis), but it has smaller transmission efficiency (roughly an order of magnitude) and it does not allow high-mass resolution to separate different atomic and/or molecular ions that are mass-degenerate. The main-chamber pressure of the Atomika is $< 5 \times 10^{-10}$ Torr.

[20] The lowest-concentration Sb spikes that were used in Ref. [I] were measured on a Cameca ims 4f magnetic sector instrument which has a lower detection limit than the Atomika.

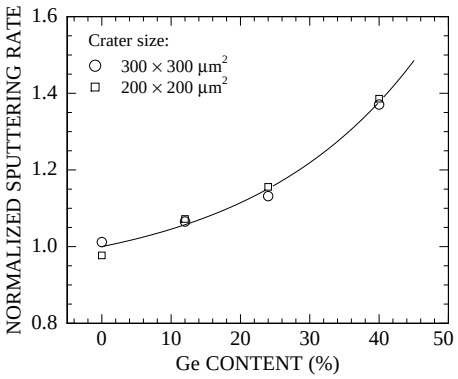

Figure 3.4: SIMS sputtering rates in $Si_{1-x}Ge_x$. Data sets were obtained with two different crater sizes, each with 3.5 keV O_2^+ at 20° off-normal, and the two sets were scaled to match each other. In each cases it was ascertained that a fixed beam current was maintained throughout the sample set. The solid line is a guide to the eye. In pure Si, the sputtering rate is approximately 5000 Å/h when a 3.5 keV O_2 beam, beam current 100 nA, is rastered over 200×200 μm^2.

Depth conversion

Conversion from sputtering time to absolute depth in the sims spectra is performed by measuring the crater depths with a Dektak 3030 profilometer. Here, a diamond stylus with a 12.5 μm tip diameter is scanned over the sample with gentle pressure ($\sim$ 5 mN). If the matrix changes with depth (as in heterostructures), it must be accounted for that sputtering rates also change with depth. Relative sputtering rates for different Ge contents x must then be obtained from uniformly doped $Si_{1-x}Ge_x$ crystals (Fig. 3.4).

3.3 Transmission-Electron Microscopy (TEM)

The purpose of TEM investigations in this work has been to detect extended defects; precipitates [I–III], threading dislocation, and misfit dislocation ([V], Chap. 8). In TEM (see, e.g., [77]), a beam of electrons is scattered as it is directed through a thin sample specimen. By means of electric-field lenses, either a direct image or a diffraction pattern is obtained when the electrons, after passage, are collected on a fluorescent screen. The microscope employed is a Philips CM20, operating with 200 keV electrons from a LaB_6 filament. For sufficient electron transmission, samples must be no thicker than a few thousand Å at maximum. Samples for cross-section view were prepared by first gluing together two samples face-to-face, then performing dimpling followed by ion milling. Most plan-view samples were prepared by chemical thinning with sample rotation, and wedge-shaped plan-view samples were prepared by tripod polishing followed by ion-beam milling.

3.4 Rutherford-back scattering spectrometry (RBS)

In this work, RBS has been used primarily to measure the chemical compositions of certain structures: The concentrations in the Sn [I] and Sb [II,III] box profiles have been measured with RBS, as has the Ge content in $Si_{1-x}Ge_x$ structures ([V], Chap. 8). RBS theory is covered by several authors; see, e.g., Ref. [63].

In RBS, a primary beam of a light element (typically H or He) is directed at the sample. The ions will scatter at nuclei at different depths in the sample, and the flux and energy distribution of the back-scattered ions (that is, H or He) is measured. Analytical expressions exist [63] for the energy of the backscattered particle as a function of the penetration depth, the mass of the scatterer, and the composition of the target.

In the current investigations, a 2 Mev He^+ beam from a Van de Graaff accelerator has been used. The sample holder is mounted on a double-axis goniometer. Near-normal incidence is usually applied, and a random spectrum (non-channelled) is obtained by setting the sample holder to slowly precesses around the beam axis (typically 2° off the axis). The energy distribution and the flux of the backscattered ions is always recorded simultaneously with two solid-state detectors: One positioned near glancing-angle (typically at a 110° scattering angle) which gives high depth resolution, and one positioned at a 161° scattering angle, which gives high mass resolution. It is checked that the spectra from the two detectors are in agreement. Typically, the accumulated charge of He^+ is between 20 and 100 μC per spectrum; to ensure measurement of the true He^+ beam current, escape of secondary electrons from the target is suppressed with an electric field. The spectra are analysed with the simulation software 'RUMP'. The chemical peak concentrations are usually reliable within $\sim \pm 5$ %.

Chapter 4

Article: Sb diffusion in a high Sn-background concentration in Si

Jacob Fage-Pedersen, Arne Nylandsted Larsen, Peter Gaiduk, John Lundsgaard Hansen, and Margareta Linnarsson, Phys. Rev. Lett. ***81****, 5856 (1998)* [I].[21]

Abstract

The diffusion of Sb in Si has been studied as a function of Sn-background concentration, and enhanced Sb diffusion is observed for backgrounds higher than $C'_{Sn} \approx 5 \times 10^{19}$ cm^{-3}. This concentration for the onset of enhanced diffusion is significantly lower than in other reports of high-concentration vacancy-mediated diffusion in Si. These reports, however, have up to now been concerned with donor impurities, whereas Sn is an electrically neutral impurity. Some Sn precipitation occurred, and the influence upon the diffusion is estimated from experiment to be small. A number of proposed models of high-concentration diffusion are discussed on basis of the data.

4.1 Introduction

Atomic diffusion in Si at very high dopant concentrations has been a subject of intensive investigations in recent years [78, 38, 37, 79, 80, 50, 81, 82]. The field, besides being of crucial importance in device processing, provides a new way of improving fundamental knowledge of dopant-dopant and dopant-point defect interactions. So far both experiment and theory have focused mostly on vacancy mediated diffusion in high background concentrations of the donor impurities As and P, and experimentally, strong diffusion enhancement is observed for concentrations exceeding $\sim 2 \times 10^{20}$ cm^{-3} [37, 83].

[21] In this reproduction of the published paper, we have divided the text into sections.

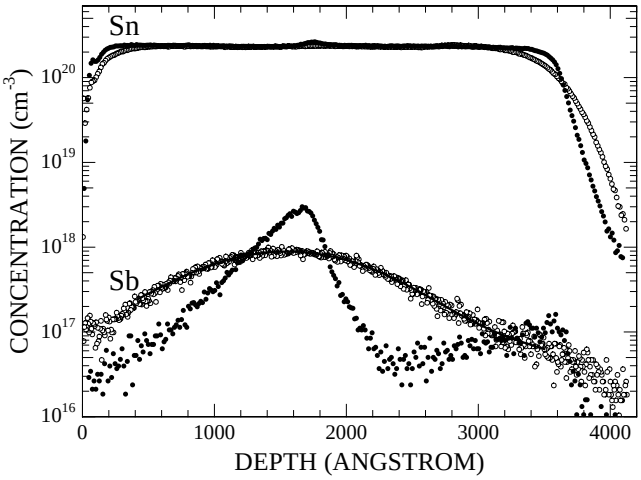

Figure 4.1: SIMS profiles of an Sb spike contained within a Sn box; as-grown (filled symbols) and diffused at 995 °C for 2 hours (open symbols). The solid curve is a Fick's law fit.

We present here a study of Sb diffusion in high background concentrations of Sn. Being isovalent to Si and having a large covalent radius, Sn interacts with vacancies by strain-relief only, whereas donor atoms have a long range Coulomb-type interaction with negatively charged vacancies. At the same time Sn enables a diffusion study with no change of Fermi level to influence the concentration of charged vacancies. Since Sb is known to diffuse predominantly by a vacancy-assisted mechanism this system is considered a rather simple one, suitable for critical tests of the diffusion theories in Si.

4.2 Experimental details

Samples were grown on Si <001> substrates in a VG-80 molecular-beam epitaxy (MBE) system. Structures were made with thin Sb spikes placed either in pure Si, inside Sn-box profiles in Si or next to Sn-box profiles in Si. A typical sample containing an Sb spike inside a Sn box is shown in Fig. 4.1.[22] Sb peak concentrations were low enough to not affect the Fermi level, i.e. $C_{\mathrm{Sb}}^{\mathrm{peak}} < n_{\mathrm{i}}$, where the intrinsic carrier density at 1000 °C is $n_{\mathrm{i}} \approx 5 \times 10^{18}$ cm^{-3}.

Annealings were performed at 995 °C in a flow furnace using an inert Ar

[22] Very abrupt Sb profiles cannot be obtained within Sn backgrounds in Si, the presence of Sn causing Sb to float at the growing surface.

ambient, and the diffusion times were corrected for furnace ramping-up and -down times.[23]

Depth profiles were measured with secondary-ion mass spectroscopy (SIMS), and two instruments were used: An Atomica 4000 magnetic quadrupole instrument with a primary O_2^+ beam of impact energy 4.5 keV and incidence angle 20° off-normal, and a Cameca ims 4f magnetic sector instrument with an O_2^+ beam, impact energy 5.5 keV and a mechanical angle of 30° off-normal. The Cameca was used to profile one series of samples that contained Sb spikes inside Sn boxes, with $C_{\mathrm{Sb}}^{\mathrm{peak}} \approx 5 \times 10^{17}$ cm^{-3} and Sn concentrations 1×10^{18} cm$^{-3} \leq C_{\mathrm{Sn}} \leq 9.9 \times 10^{19}$ cm^{-3}. All other samples had $C_{\mathrm{Sb}}^{\mathrm{peak}} \approx 3 \times 10^{18}$ cm^{-3} and were profiled with the Atomica. Depth calibrations were made by measuring the crater depths using a Dektak profilometer with a relative accuracy better than 3 %.

Extraction of diffusion coefficients was done by numerically diffusing the SIMS profile of the as-grown sample according to Fick's 2nd law and minimizing the error between the simulated diffused profile and the measured diffused profile with respect to the diffusivity D_{Sb}.

4.3 Experimental results

The main result is presented in Fig. 4.2: At low Sn concentrations a constant Sb diffusivity $D_{\mathrm{Sb}}(995°\mathrm{C}) = 1.18 \times 10^{-15}\mathrm{cm}^2/\mathrm{s}$ is observed, in perfect agreement with the intrinsic value [43]. Enhanced Sb diffusion occurs at Sn concentrations higher than $C'_{\mathrm{Sn}} \approx 5 \times 10^{19}$ cm^{-3}, and at $C_{\mathrm{Sn}} = 4.7 \times 10^{20}$ cm^{-3} the enhancement is a factor of 3 relative to the intrinsic value.

We may note, from analyzing the box profiles, that also Sn diffusivity increased with concentration. No systematic investigation was made, however, since this diffusion was not under isoconcentration conditions.

We first demonstrate that the observed enhancement can not be explained by lattice strain, nor by point defect injection related to Sn precipitation. The latter topic received special attention, the solid solubility limit of Sn being $\sim 5 \times 10^{19}$ cm^{-3} at 1000 °C [84].

Biaxial, compressive *lattice strain* may in general exist in $Si_{1-x}Sn_x$ layers that are grown epitaxially upon Si substrates. Kringhøj *et al.* [85] recently showed, from a $Si_{0.91}Ge_{0.09}$ system, that a compressive strain s causes an Sb-diffusivity

[23] In each annealing the temperature T_i is recorded as a function of time t_i. An effective diffusion time t_{eff} is then calculated by summing all time steps $\Delta t_i = t_{i+1} - t_i$ with weights, according to $t_{\mathrm{eff}} = \sum_i \Delta t_i \exp\left(-\left[\frac{Q}{kT_i} - \frac{Q}{kT}\right]\right)$. Here T is the temperature at the plateau (995 °C), and the activation energy of intrinsic Sb diffusion, $Q = 4.08$ eV [43], was used in all cases. Typically t_{eff} is less than 10 minutes longer than the nominal, preset heating time, so that corrections are insignificant at all but the shortest annealing times.

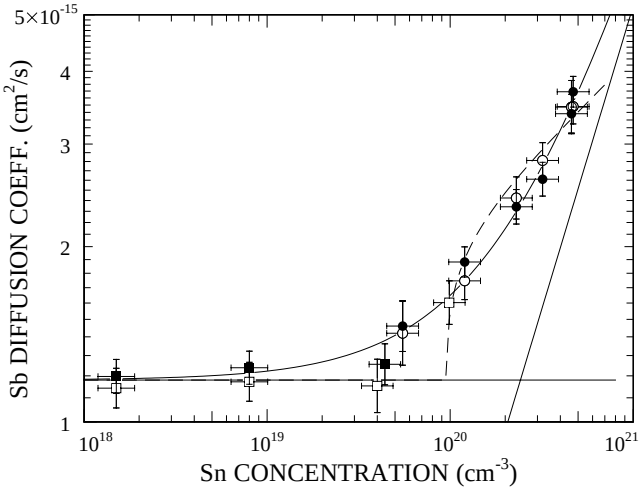

Figure 4.2: Sb diffusivity at 995 °C vs. Sn-background concentration in samples of the type shown in Fig. 4.1. The solid curve is Eq. (4.3) of which the two straight lines are the individual terms. The dashed curve is Eq. (4.1). Samples were diffused for 2 hours (filled symbols) or 3 hours (open) and profiled with an Atomika (circles) or a Cameca (squares). Identical symbols also correspond to samples that were annealed simultaneously, under exact identical conditions. Vertical errors here and in Fig. 4.4 are from fitting and depth calibration. Horizontal errors stem from scaling of SIMS signals relative to calibration samples that were measured with Rutherford backscattering.

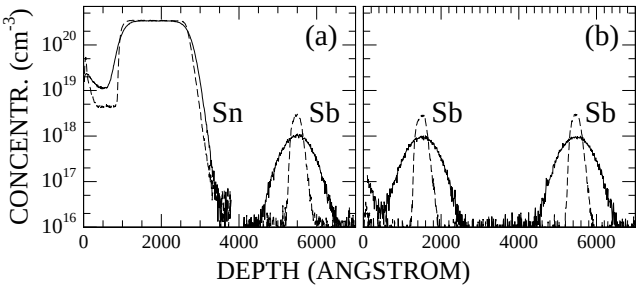

Figure 4.3: MBE structures for testing Sb diffusion (a) with and (b) without a Sn-box; as-grown (dashed) and annealed at 995 °C for 1 hour (solid). The two spikes in (b) have the same diffusivities, showing that surface effects are unimportant.

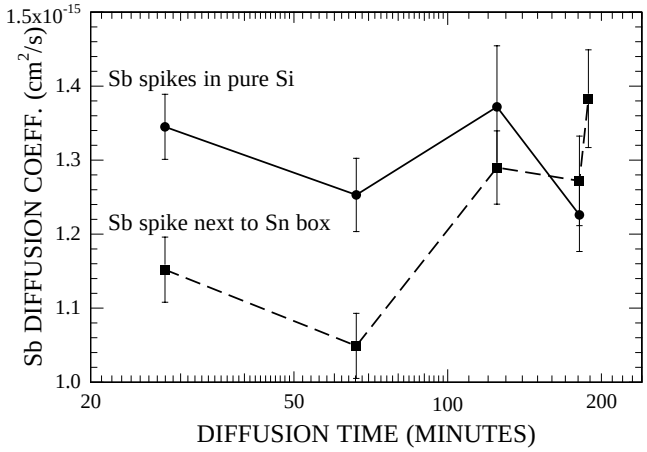

Figure 4.4: Diffusion coefficients at 995 °C of the Sb profiles in Fig. 4.3, vs. annealing time. Points that are vertically above each other represent samples that have been annealed simultaneously, under exact same temperature and time conditions.

enhancement $F_{\text{strain}} = \exp(Q's/kT)$ with $Q' = 13 \pm 3$ eV. This value does not include chemical effects specifically related to Ge. The strain in epitaxial $Si_{1-x}Sn_x$ layers on Si is determined with great precision [86] from Vegard's linear interpolation between the lattice parameters of Si ($a_{\text{Si}} = 5.4311$ Å) and α-Sn ($a_{\text{Sn}} = 6.4890$ Å), so that $s = (1 - a_{\text{Sn}}/a_{\text{Si}})x = 0.1948x$. Supposing that the Sn layers were fully strained under diffusion and inserting $x = 0.01$, corresponding to the highest Sn-concentration, we find an upper limit $F^{\text{max}}_{\text{strain}} = 1.26$. Thus lattice strain can at most account for a small contribution to the diffusivity enhancement, the major effect still being specifically related to the chemical nature of Sn.

To reveal whether *Sn precipitation* would create an injection of point defects and thereby affect Sb diffusion, two MBE structures were grown that contain respectively two Sb spikes in pure Si and one Sb spike positioned next to a high concentration (3.3×10^{20} cm^{-3}) Sn box in Si, see Fig. 4.3. As shown in Fig. 4.4, Sb diffusivities were then measured in these two samples at 995 °C after different annealing times. We see that at short times (1/2 h, 1 h) Sn precipitation leads to a slight retardation of Sb diffusion. Sb being a vacancy-assisted diffuser, this suggests that Si self-interstitials are injected. At long diffusion times (2h, 3h), however, the retardation is no longer significant, indicating that the injection is only transient.

This is in accordance with plan view transmission-electron microscopy (TEM) investigations of Sn precipitates in samples of the type shown in Fig.

4.1, after respectively 1 and 3 hours of annealing at 995 °C. After 1 hour precipitates had formed in samples with $C_{Sn} \geq 1.2 \times 10^{20}$ cm^{-3}, all of a distinct size of approximately 10 nm. After 3 hours sizes ranged from $\sim$ 5-18 nm, the evolution in sizes probably taken place by Ostwald ripening. A rough estimate of precipitate volumes gives the important result that the fraction of Sn atoms that have gone into precipitates is very small, less than 1% in any sample (assuming that all precipitates are seen by TEM and that precipitates are pure Sn). Moreover, this fraction did not increase from from 1 to 3 hours of annealing.

One should be cautious when generalizing the results of Fig. 4.4 to Sb diffusion *inside* a Sn box, but we still estimate that diffusivities extracted from long diffusion times (2h, 3h), are only slightly influenced by point defect injection from Sn precipitation. In any case, such an injection can at most have a retarding - not enhancing - effect.

Important also, *dislocations* were low enough in density to not play any part in the diffusion. At $C_{Sn} = 4.7 \times 10^{20}$ cm^{-3} the density of misfit dislocations was estimated from TEM on plan-view and cross-sectional samples, both before and after annealing, to be $\sim 10^6$ cm^{-2} or less. The far majority were located at the SiSn/Si interface. Threading dislocations were seen at a density that was at least one order of magnitude lower. Hardly any dislocations were found at $C_{Sn} = 3.2 \times 10^{20}$ cm^{-3}, and none below this concentration.

4.4 Discussion

For the system at hand a comparison is relevant with Sb diffusion in relaxed $Si_{1-x}Ge_x$. Here an enhancement also occurs [43,85], but the mechanism seems to be fundamentally different, since it sets in only in alloys that are increasingly Ge-like; e.g., a factor of 2 enhancement requires $x \leq 0.10$ [43]. The small-size group-IV impurity C is known to retard B diffusion by inducing an undersaturation of Si self-interstitials [87], but effects of high C concentrations upon vacancy diffusers have, to our knowledge, not been studied.

In the following we will discuss a number of proposed models for high--concentration diffusion in Si.

Mathiot and Pfister [78,88,89] put forward a *vacancy-percolation model*. The idea is that the dopants will set up a vacancy-percolation network when their concentration exceeds a critical value C^*. In this limit vacancies will namely feel a simultaneous attraction to two or more dopant atoms, which leads to a lowered barrier for vacancy migration and a vacancy concentration increase. For any atoms that may diffuse via vacancy-exchange the effective diffusivity then has two contributions, D^{perc} and D^{norm} ($= 1.18 \times 10^{-15}$ cm^2/s for Sb), from diffusion inside and outside percolation regions:

$$D^{eff} = P_\infty D^{perc} + (1 - P_\infty) D^{norm}. \tag{4.1}$$

Here P_∞ is the probability that an atom belongs to an 'infinite' percolaton cluster:

$$P_\infty = \begin{cases} 0 & \text{for } C < C^* \\ \min\left[1, K\left(\frac{C}{C^*} - 1\right)^\beta\right] & \text{for } C > C^* \end{cases}, \tag{4.2}$$

$\beta = 0.4$ and K is a constant. Diffusion in Sn backgrounds is particularly simple, since Sn induces no Fermi-level shift, so D^{norm} and D^{perc} have no doping dependence.

In Fig. 4.2 the data was fitted according to Eq. (4.1) (dashed curve). From the fit $K = 0.44 \pm 0.02$. A fixed value of $D^{\text{perc}} = 4 \times 10^{-15}\text{cm}^2/\text{s}$ was used, since this value is slightly above the highest measured value of D_{Sb}. The experiment, however, does not indicate that D_{Sb} reaches a plateau (equal to D^{perc}) at high Sn concentrations, and the Sb-diffusivity increase is not as sudden as predicted.

The fitted percolation threshold is $C^*_{\text{Sn}} = 9.6 \pm 0.5 \times 10^{19}$ cm^{-3}, considerably lower than thresholds observed for diffusion in group-V backgrounds. Theory gives $C^* \approx 2 \times 10^{20}$ cm^{-3} [90], corresponding to the limit above which a vacancy that escapes to a 3rd neighbour position from one dopant will be a 2nd neighbour to another dopant, and this value has been in good agreement with group-V diffusion experiments [78,37,83,88,89].

In the above framework the fact that C^* is lower for Sn than for a group-V background would suggest that the Sn-V potential (V denotes vacancy) has a longer range than donor atom–vacancy potentials. But in conflict one will expect *a priori* that the purely elastic Sn-V potential falls off more rapidly than a Coulomb-like donor atom–vacancy potential. (Such a potential was calculated by Pankratov *et al.* [27] for As.) If the Sn-V potential had indeed been long-range it would have a strong binding energy ΔE_2 at the 2nd neighbour separation, and this would have caused a much stronger diffusivity enhancement $F = D^{\text{perc}}/D^{\text{norm}} = \exp(\Delta E_2/kT)$ [88] than seen.

Thus it is likely that a different scenario is needed to explain enhanced diffusion of Sb in a Sn background. But vacancy percolation (despite the crudity of the model - see, e.g., [91]) may still provide a good starting point for discussion of high concentration group-V diffusion, and it might also be important at higher Sn concentrations.

Ramamoorthy and Pantelides [80] recently performed *first-principles* calculations on As complexes in Si. They found that not only are As impurities bound strongly (with ~1.5 eV per As atom) in $\text{As}_n V$ complexes, $1 \leq n \leq 4$, but also that $\text{As}_2 V$ is highly mobile, with a diffusion activation energy of only 2.7 eV. They suggest therefore that $\text{As}_2 V$ complexes play a significant role in enhanced As diffusion at high concentrations, and that the complexes may dominate diffusion at concentrations below the percolation threshold. In possible support hereof Sb diffusion in isoconcentration diffusion studies [82] in the

concentration range $2.3 \times 10^{18} - 2.5 \times 10^{19}$ cm^{-3} was enhanced more strongly than was expected from Fermi-level effects. (At higher concentrations diffusion was retarded due to precipitation.) Here Sb_2V, due to the similarity of Sb and As, could be the dominating diffusing species.

A corresponding complex for mediating Sb diffusion in a Sn background would be Sb-Sn-V, where one of the group-V atoms has been swapped with Sn. The formation of such a complex will benefit from the lack of Coulomb repulsion between Sb and Sn. At the same time one can expect that the vacancy is bound to the two dopants during diffusion because of the positively charged Sb^+ and because of strain, considering the large sizes of Sn and Sb atoms. In first order reaction kinetics the number of such complexes will increase linearly with C_{Sn}, giving a contribution with a slope $a = 1$ in a log-log plot of diffusivity vs. Sn concentration. Indeed, such behaviour is supported by the solid curve fit of Fig. 4.2, where we used the expression

$$D = D_0 + D_1 \left(\frac{C_{Sn}}{C_S} \right)^a \tag{4.3}$$

From the fit $a = 1.04 \pm 0.05$ and $D_1 = 3.1 \pm 0.8 \times 10^{-13}$cm^2/s. $D_0 = 1.18 \times 10^{-15}$cm^2/s was used for intrinsic Sb diffusion via Sb-V pairs, and $C_S = 5 \times 10^{22}$ cm^{-3} is the Si atomic density.

For Eq. (4.3) to hold the vacancy concentration must not increase abruptly, since this itself would cause a diffusivity enhancement. Also, in Eq. (4.3), in thermodynamical equilibrium the fraction of Sb atoms that are in Sb-V pairs is not affected by formation of Sb-Sn-V complexes. This can be expected to be fulfilled, requiring only that the number of Sb-V pairs and Sb-Sn-V complexes is low relative to the number of Sb atoms.

A number of authors [50, 81, 92] used *Monte-Carlo* methods to model high--concentration group-V diffusion. Dunham and Wu [50] obtained good agreement with data from [37] by assuming a linear dopant–vacancy potential with a range to the 3rd coordination order and no dopant-dopant interactions. List and Ryssel [81] performed similar simulations, but with a much larger number of diffusion hops. They found that diffusion would retard at high concentrations due to clustering of dopants as a by-product of the dopant–vacancy attraction. Good results were obtained only with a *non*-attractive potential with low vacancy migration barriers near the dopant atom. It appears that Monte-Carlo simulations are still to be improved, incorporating *ab initio* potentials, where possible, and allowing for mobile two-atom complexes.

An alternative model has been proposed by Antoncik [79]. In this model diffusion is enhanced when the dopant concentration approaches the solubility limit, the argument being that decay of diffusing dopant–vacancy pairs should slow down. The model cannot explain the enhancement in the Sn system though, since even at $C_{Sn} = 4.7 \times 10^{20}$ cm^{-3} we have effectively not reached a

limit on the number of Sn atoms that can be incorporated substitutionally.

Summarizing, we have presented data that show diffusion enhancement at 995 °C of Sb in Si when Sn-background concentrations exceed $\sim 5 \times 10^{19}$ cm^{-3}. It was made probable that Sn precipitation causes injection of self-interstitials, but that the effect upon the Sb diffusion at diffusion times of $\sim$ 2-3 hours is small, though possibly retarding. We argued from the diffusion data that the vacancy percolation model can not be applied to explain the diffusivity enhancement in the present system, but that a likely diffusion mechanism to prevail at high concentrations is diffusion via Sb-Sn-V complexes.

Acknowledgements

This work was funded by the Danish Natural Science Research Council, and one of us (M.L.) has received support from the Swedish Foundation for Strategic Research.

Chapter 5

Vacancy-mediated diffusion at high dopant concentrations

This chapter relates to the experimental article [I] that was presented in the preceding chapter. Here, we critically review relevant literature on vacancy-mediated diffusion at high impurity concentrations and, in particular, we address the issue of percolation vs. complex formation. We also provide an elaborated discussion on the interpretation of the diffusion data of Chap. 4, and we give experimental details on the issue of Sn precipitation.

5.1 Introduction

The need for insight into mechanisms of diffusion in general and of diffusion at high dopant concentrations in particular, was thoroughly motivated in the introductory chapter and in Chap. 4. For the particular case of varying Sn-background concentrations in Si we found that the diffusion of Sb was enhanced at concentrations $C_{\mathrm{Sn}} \gtrsim 5 \times 10^{19}$ cm^{-3} according to Eq. (4.3),

$$D = D_0 + D_1 \left(\frac{C_{\mathrm{Sn}}}{C_S} \right)^a .$$

Here, D_0 is the intrinsic diffusion coefficient of Sb (via E centers), the power dependence $a \approx 1.0$, D_1 is a prefactor factor, and $C_S = 5 \times 10^{22}$ cm^{-3} is the host atomic density.

The 'Sb in Sn' system as such is not of direct technological interest, but the above finding is important for fundamentals of diffusion since it is a possible indication of the existence of mobile two-atom clusters. The linear dependence on Sn concentration hints, namely, that a fraction of the Sb-atoms are contained within mobile SbSnV triple complexes ($C_{\mathrm{SbSn}V} \propto C_{\mathrm{Sn}}$). Over the years, various models have been invoked to explain concentration dependence of diffusion in various systems, and whereas our experiments do not irrefutably give proof of mobile triple complexes, no other model is readily compatible with

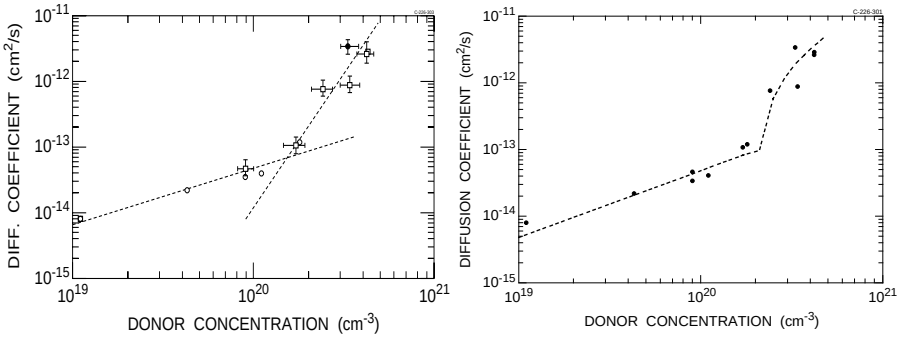

Figure 5.1: Sb diffusion coefficient at 1050 °C as a function of P-background concentration. The same data is presented with a straight-line fit (left) and a percolation-model fit (right). From Nylandsted Larsen *et al.* [37].

the data. E.g., we argued briefly on p. 42 that the solubility-limit model of Antoncik [79,93] can not explain the observed [I] diffusion enhancement of Sb in a Sn background in Si. And the model of Walukiewicz [94] is based on the onset of degenerate carrier statistics, thus, it is not pertinent to Sn, but only to electrically active dopants (and even so it appears to be of most use in *p*-type GaAs).

In the following, we will critically review parts of the existing literature on high-concentration impurity diffusion via vacancies.

5.2 Vacancy percolation in group-V backgrounds in Silicon

5.2.1 Background

High-concentration furnace-annealed implants of As and P impurities were found to diffuse rapidly in the peak region [88,95,89]. As a result, profiles were produced that had a modest slope at the top and a much steeper slope towards the bulk and could not be fitted in agreement with the Fair model (Eq. 2.37). These profiles could be reproduced by Mathiot and Pfister (MP) within the *vacancy-percolation model* [88,95,89]. Also, peak concentrations of a range of As implants decreased rapidly ($\sim$ 15 s) at 1050 and 1090 °C to the same 'magic' concentration, 2.5×10^{20} cm^{-3} [83]. Below this concentration level, only little redistribution took place even after 1 min. Later, the vacancy-percolation model was successfully applied to isoconcentration diffusion experiments of Nylandsted Larsen *et al.* (LL) [78,37], with implanted P backgrounds. Results from those experiments are reproduced in Fig. 5.1.

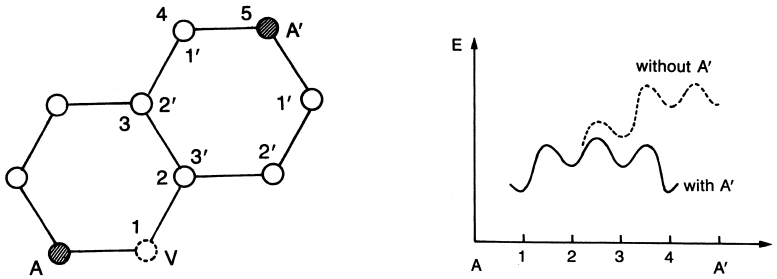

Figure 5.2: The phenomenon of vacancy percolation: A vacancy V migrates near substitutional impurities A and A' in the Si lattice, and the vacancy potential energy is shown as a function of distance from A, under the assumption that A and A' have a 5nn separation. From Ref. [9], after Ref. [88].

From the experiments cited here, it would seem that the percolation model, despite some crude assumptions (see Sec. 5.2.3), provides a good foundation for understanding and modelling of vacancy-mediated diffusion, at least in some high-concentration group-V systems.

5.2.2 Review of the vacancy-percolation model

The model requires that an attractive potential exists between dopants and vacancies. At least a 3nn interaction range can be assumed for diffusion via the E center mechanism, and therefore, if two dopants are placed at a 5nn separation of each other, a number of lattice sites will exist in which a vacancy will experience a simultaneous attraction to more than one dopant atom. In these sites of overlapping potentials, as illustrated in Fig. 5.2, the effective potential energy of the vacancy can be taken as a superposition of the interaction potentials with the individual dopant atoms. At sufficiently high dopant concentrations, those lattice sites that are affected simultaneously by at least two dopant atoms will constitute an infinite, connected network. Inside this network, (i) the effective vacancy formation enthalpy is lowered, and (ii) the vacancies can freely *percolate* since the barrier is lowered for a vacancy to escape to at least a 3nn distance from one dopant atom and be ready to accomplish a new migration step with this or another dopant.

Due to vacancy percolation, *any* diffuser that has a significant vacancy component will experience enhanced diffusion inside the network. The enhancement takes place as a collective phenomenon when the E centers can no longer be considered as isolated entities.

At the time, MP arrived at the conclusion [89] that P (and even B) diffusion

is essentially vacancy-assisted at high concentrations.[24] Inasmuch as we know today that intrinsic P diffusion proceeds primarily via Si *self interstitials* (see p. 9), it is well established (from DLTS, EPR, and other techniques) that P-V pairs do form, e.g., under irradiation. *So it is not unexpected that P layers can attract large concentrations of vacancies, and it need not be a conceptual problem if P itself, at high concentrations, diffuses via vacancies – but we should mention that the latter point has no solid experimental evidence.*

The analogy to vacancy percolation, of a liquid flow through a maze of pipes can be used. In *bond* and *site* percolation problems, respectively, the bonds (pipes) or the sites (intersections) are randomly open for current flow with some probability p and blocked with a probability $1-p$. In the Si lattice, vacancy flows will go predominantly between those lattice sites that contain dopant atoms. Thus, as an example of site percolation, the effect of adding a dopant atom A' to a lattice site in adequate proximity of other dopant atoms $\{A\}$ is to allow vacancies to migrate through the A' site (that is, to 'open' the site).

In standard percolation theory it is believed [96] that precisely one infinite percolation network will exist when p exceeds the *percolation threshold* p^*. In the formulation of MP [88], the percolation threshold corresponds to a *critical concentration* C^* of dopant atoms. At $C_A = C^*$, a sufficiently large fraction (not all!) of the dopant atoms will have at least one other dopant situated within the volume of a 5nn 'shell'. Therefore, the 5nn percolation problem can be transformed into a 1nn problem on a suitable lattice, on which p^* is tabulated [96]. Along slightly different lines of approach, MP [88] and Christensen [97] calculate, respectively

$$C^* = \quad 3 \times 10^{20}\ \mathrm{cm}^{-3}, \tag{5.1}$$

$$C^* = 1.85 \times 10^{20}\ \mathrm{cm}^{-3}. \tag{5.2}$$

For visualization: a concentration of 2×10^{20} cm^{-3} corresponds to a density of 1 impurity per 250 Si atoms or an approximate impurity separation of ~ 17 Å.

Above C^*, the fraction P_∞ of lattice sites that belong to this infinite percolation cluster grows with dopant concentration [Eq. (4.2) of the preceding chapter],

$$P_\infty = \begin{cases} 0 & \text{for } C < C^* \\ \min\left[1, K\left(\frac{C}{C^*} - 1\right)^\beta\right] & \text{for } C > C^* \end{cases},$$

P_∞ vs. C_A is shown in Fig. 5.3. The slope of the curve above C^* is determined

[24] MP argued [89] that the mobile interstitialcy PI is positively charged. Therefore, the interstitial-related diffusion component will not increase with Fermi level, whereas the (under intrinsic conditions, small) vacancy component may increase with Fermi level.

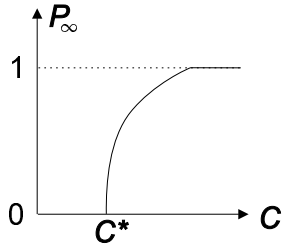

Figure 5.3: The probability P_∞ that a given lattice site belongs to the infinite percolation cluster, as a function of dopant concentration. The curvature of the curve above $C = C^*$ is set by the critical exponent β.

by the critical exponent β; in three dimensions $\beta = 0.4$ is obtained numerically [96]. K is a proportionality factor. The effective diffusion coefficient [78] is then given by [Eq. (4.1)]

$$D^{\text{eff}} = P_\infty D^{\text{perc}} + (1 - P_\infty) D^{\text{norm}}.$$

D^{norm} accounts for the normal E center diffusion in regions outside the percolation cluster; to a good approximation[25] it can be written on the form of Eq. (2.41). D^{perc} accounts for the diffusion within the percolation cluster. It is given by

$$D^{\text{perc}} = F D_V C_V, \quad \text{where} \quad C_V = C_{V^0} \left[1 + \delta^- \frac{n}{n_{\text{i}}} + \delta^= \left(\frac{n}{n_{\text{i}}} \right)^2 \right]. \tag{5.3}$$

The square brackets, with the δ's defined on p. 13, represent the vacancy increase due to a shift of Fermi level, and the vacancy diffusivity D_V is assumed to be charge-state independent. F is an enhancement factor that is due to the lowering of the vacancy potential inside the cluster [88]. Since a vacancy inside the cluster is always created within a 2nn distance of some dopant atom,

$$F = \exp\left(\frac{\Delta E_2}{kT} \right). \tag{5.4}$$

In Fig. 5.1 we showed a set of data (Sb in a P background) that is in good agreement with the percolation model. At background concentrations below $\sim 2 \times 10^{20}$, the increase of D_{Sb} is very close to linear, indicating that diffusion takes place via singly negatively charged point defects, i.e., the diffusing defect is Sb^+V^-. At background concentrations above $\sim 2 \times 10^{20}$ the diffusion is seen (with no specific physical rationale) to roughly obey a power law,

$$D_{\text{Sb}} \propto C_{\text{P}}^{3.5}. \tag{5.5}$$

[25] In the derivation by MP, D^{norm} was derived to fit the general flux equation $J_A = -D^{\text{norm}} \partial C_A / \partial x$ for normal E center diffusion. Thus, D^{norm} has a more complicated expression [Ref. [78], Eq. (8)] than D'_A given by Eq. (2.41), since the latter obeys instead (2.31): $J_A = -D'_A \partial C_{A_s^+} / \partial x$. On close inspection, D'_A of course does approximate D^{norm}.

A power of 1, or perhaps even 2, would have been compatible with pair diffusion via singly or doubly charged vacancies, but *the high power of 3.5 very strongly implies that a mechanism other than simple pair diffusion prevails* (see also p. 56). The important point should be brought to attention that in this high--concentration regime, several different vacancy diffusers (Sb, As, Sn, Ge) were found to have almost the same diffusion coefficient [37] – even though Sn and Ge diffuse much slower under intrinsic conditions. Therefore, *the diffusion is determined primarily by the interaction between background atoms (P) and vacancies, and only to a lesser extent by the chemical nature (group IV or V) of the diffusing element*. The diffusing element acts merely as a marker of the vacancy percolation.

Diffusion of both Sb and As in a P-background concentration was fitted [37] with the use of

$$C_{\mathrm{P}}^{*} = 2.2 \times 10^{20}\ \mathrm{cm}^{-3}. \tag{5.6}$$

Furthermore, profiles of high-concentration P and As implants were simulated well with $C_{\mathrm{P}}^{*} = 2.5\text{–}3 \times 10^{20}\ \mathrm{cm}^{-3}$ [88, 89], $C_{\mathrm{As}}^{*} = 1.3 \times 10^{20}\ \mathrm{cm}^{-3}$ [89], and for Sb in an homogenous P background, with $C_{\mathrm{P}}^{*} = 2.5 \times 10^{20}\ \mathrm{cm}^{-3}$ [78]. The values for P are in excellent agreement with calculated values. The lower value of C_{As}^{*} was unexpected and the value was tentatively explained with a non-random As distribution due to long-range interactions. But possibly, the result could be considered anomalous since As peak concentrations decreased rapidly only down to $\sim 2.5 \times 10^{20}\ \mathrm{cm}^{-3}$ [83], almost independent of anneal time, and the diffusivity of P in an As background [36] increased with concentration linearly all the way up to $n = 1.8 \times 10^{20}\ \mathrm{cm}^{-3}$, hinting that in fact $C_{\mathrm{As}}^{*} > 1.8 \times 10^{20}\ \mathrm{cm}^{-3}$.

5.2.3 Some critical remarks

Convincing as the vacancy-percolation model may seem, some crude aspects of it should still be mentioned.

(i) Were finite-size clusters also taken into account, a somewhat more gradual increase of diffusivity with dopant concentration could possibly be expected. (ii) In percolation theory, the value $\beta = 0.4$ of the critical exponent is applicable only very near C^{*} [96]. (iii) In the hindsight where we have a better feeling for the shape of the donor atom–vacancy potential (Fig. 2.5) and have confirmation of a long range of interaction, one could have anticipated that already at *lower* dopant concentrations (e.g., corresponding to a 6nn separation or larger) is a vacancy in any site simultaneously affected by two or more dopant atoms, thus leading to the percolation effect. (iv) The use of a fixed enhancement factor $F = \exp(\Delta E_2/kT)$ can be questioned; it can be argued that F should gradually increase with impurity concentration when more dopant

atoms become within a 4nn distance of each other, rather than 5nn. (v) On the possibility of a breakup, during diffusion, of the percolation network into isolated patches, one can only speculate. Some of these aspects are also discussed by van Opdorp [91].

A refined and full model should take into account the above deficiencies. Alas, this would be on the expense of an analytical approach to diffusion modelling, and to test against experiments would necessitate *Monte Carlo simulations*. But even this technique has limitations since (i) many degrees of freedom will be involved, resulting in a set of parameters far larger than can realistically be assessed when comparing with experiment [81], and (ii) in the concentration regime where collective phenomena set in, lattice Monte Carlo simulations presently tend to overestimate the role of dopant clustering [50,81]. In this respect, a proper statistical-mechanical formalism must be incorporated [98]. For lattices with realistic vacancy concentrations, present-day calculation times allow only simulation of a fraction of an Ångström diffusion lengths [50,81].

Given the above reservations on some quantitative matters of the percolation model, we still wish to make the concluding remark that the model indeed does a very good job of predicting the observed diffusion enhancements. The fact remains that the calculated values of the critical concentration have a good correspondence with experiment, and we consider the model to be a useful framework for a phenomenological understanding of diffusion enhancements in certain high-concentration group V systems. In Sec. 5.4 we will comment more on the applicability of the model.

5.3 Impurity–vacancy complexes

5.3.1 Findings in the literature

Other experimental and theoretical findings do not, or do only partially, conform with the picture of percolation. These works suggest dopant–vacancy cluster formation – either with an enhancing [80] or a retarding [35,99,28] effect upon diffusion. Most work has been done on As, but since focus is on the interaction with vacancies, the findings are pertinent to other vacancy diffusers also, including Sn. Below, we collect the central results of several works; many of these works are of high relevance also for the complex formation of Sb and vacancies, to be discussed in Chaps. 6 and 7.

(i) Fair and Weber (FW) [35] analysed As profiles that were indiffused with 1000 °C furnace annealings. In initially-p-type Si, they reported a diffusivity increase with total As concentration C_T, up to a maximum at $C_T \approx 38n_i$, corresponding to $C_T \approx 2.8 \times 10^{20}$ cm^{-3},[26] and above that a

[26] Rather odd, in initially-n-type Si at 1058 °C, a D_{As} maximum was obtained already at $C_T \approx$

diffusivity *decrease* up to at least $C_T \approx 8 \times 10^{20}$ cm^{-3}. The data could be modelled under the assumptions that As^+V^- was the mobile species and that all electrically inactive As (assumed to be As_2V [35]) was *immobile* (i.e., the diffusivity increase was linear in n/n_i). It is worth to point out that only resistivity profiles were measured, thus, the total As profiles were always indirectly obtained. And D_{As} vs. C_T curves were obtained from a Boltzmann-Matano (BM) analysis [100].

(ii) Solmi and Nobili (SM) [99], by using furnace annealings at 900–1050 °C, indiffused P and As from surface layers of monoclinic SiP and SiAs precipitates, respectively. This technique should ensure optimum fulfilment of the boundary condition for a Boltzmann-Matano analysis, viz. that time-independent P and As concentrations are upheld at the interface between the Si matrix and the precipitated phase. (This situation is opposed to indiffusion from low-energy implantations, doped poly-silicon or doped oxides.) In agreement with FW [35], SN observed a maximum both in the P and the As diffusivity. The maxima occurred at dopant concentrations that correspond closely to the highest equilibrium value n_e that can be achieved of the carrier density at the given temperatures; $D_P^{max}(900, 1000\ ^\circ\text{C}) \approx 3.0 \times 10^{20},\ 5.1 \times 10^{20}$ cm^{-3}, $D_{As}^{max}(900\ ^\circ\text{C}) \approx 2.2 \times 10^{20}$ cm^{-3} and $D_{As}^{max}(1050\ ^\circ\text{C}) \gtrsim 5 \times 10^{20}$ cm^{-3} (D_{As} saturates). SN did *not* find evidence for a strong [i.e. more rapid than $(n/n_i)^2$] diffusion enhancement like percolation or As_2V/P_2V diffusion. Since diffusivities *decreased* for $C_A > n_e$ (A = As, P), SN concluded that deactivating clusters had formed in this concentration region, most types of which are *not* mobile.

(iii) Ramamoorthy and Pantelides (RP) [80] performed DFT total-energy calculations on AsV_n complexes ($n = 1...4$) and As_2V_n complexes ($n = 2, 4, 6$). They proposed that As_2V clusters form at high concentrations and *accelerate* As diffusion. The movement of As_2V is illustrated in Fig. 5.4. The calculated activation energies of diffusion via E centers, via triple complexes, and in a percolation network are, respectively,

$$Q_{AsV} = 2.5 + 1.4 = 3.9 \text{ eV} \tag{5.7}$$

$$Q_{As_2V} = \underbrace{0.8}_{H^f} + \underbrace{1.9}_{H^m} = 2.7 \text{ eV} \tag{5.8}$$

$$Q_{AsV,5nn} \sim 2.9 \text{ eV} \tag{5.9}$$

Following those authors [80], a percolation network will break up immediately ($\sim$ few seconds) into As_2V complexes. Over RTA times ($\lesssim$1 min),

$5n_i$ [35], corresponding to $C_T \approx 4 \times 10^{19}$ cm^{-3}. Both n and p-type material were initially 1-Ω cm ($N_D = 4 \times 10^{15}$ cm^{-3}, $N_A = 1.2 \times 10^{16}$ cm^{-3}).

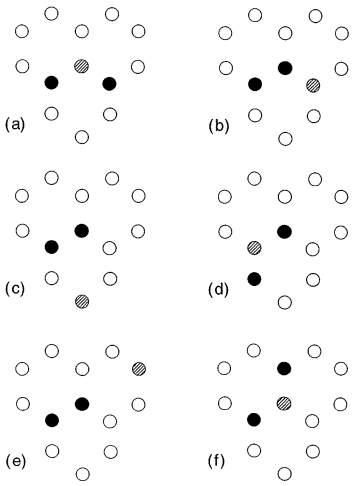

Figure 5.4: Schematic of the migration of the As_2V defect in Si. The hops proceed either as (a) → (b)→ (c) → (d) or as (a) → (b)→ (e) → (f). From Ref. [80].

these complexes (or AsPV complexes for As in a P background) are responsible for high-concentration *enhanced* diffusion, but over furnace annealing times, extensive clustering will result from As_2V migration, and, thus, cause retarded diffusion and deactivation.

(iv) Somewhat akin to the work of RP [80], but with dissimilar conclusions, Xie and Chen (XC) [28] very recently performed total-energy calculations on As–V–As configurations of various As-As separations. XC conclude that As diffusion is greatly enhanced due to *collective interaction* (percolation) when As atoms are at 5nn or 6nn separations. It is helpful to draw up the following results [28]:

$$Q_{AsV} = 2.37 + 1.19 = 3.56 \text{ eV} \tag{5.10}$$

$$Q_{As_2V} = 1.02 + 2.0 = 3.02 \text{ eV} \tag{5.11}$$

$$Q_{AsV,5nn} = \underbrace{2.06}_{H^f} + \underbrace{0.45}_{H^m} = 2.51 \text{ eV}. \tag{5.12}$$

In the 5nn percolation situation, the formation and migration energies are obtained simply by repeating the AsV calculation with an additional As atom situated as a 5nn to the first one. XC suggest that a percolation network persists for typical RTA times, but at furnace annealing times it breaks up into As_2V complexes, driven by the low energy of formation of As_2V. These slow-moving complexes (high migration barrier) are argued by XC to cause a diffusion *retardation* at the very highest concentrations in furnace annealings [35, 99]. Supposedly [28], a diffusion retardation can potentially be caused by (large) clusters that have a *low* activation energy

of diffusion, since XC argue that $Q_{\mathrm{As}_m V} < Q_{\mathrm{As}_{m-1} V}$ for $m \leq 4$. In their discussion, XC do not discriminate between As and P backgrounds.

(v) Many experiments show that vacancies accompany group-V atoms after deactivation (As, Sb) or high-concentration diffusion (Sb in P backgrounds). After 750-°C deactivation of 8×10^{20}-cm^{-3} As material, Lawther *et al.* [101] measured the vacancy concentration with positron annihilation. By assuming $\mathrm{As}_n V$ complexes, it was found that on the average, $\bar{n} = 2.5 \pm 0.7$ after 15 s and $\bar{n} = 3.2 \pm 0.8$ after 2 h. Rousseau *et al.* [58] attributed a flux of Si self-interstitials, generated during As deactivation, to the formation of $\mathrm{As}_n V$ complexes ($n = 1...4$). We found that an interstitial flux from annealed Sb layers probably originated from $\mathrm{Sb}_2 V$ formation [III] (see Chaps. 6 and 7). Very-high concentration Sb layers contained precipitates as well as Sb–vacancy complexes after laser annealing, supposedly with two vacancies, as estimated with extended x-ray fine structure absorption (EXAFS) [102]. And with Mössbauer spectroscopy after RTA of Sb implants in highly doped P backgrounds [103, 104], the existence was inferred of SbV pairs (isomer shift 2.32 mm/s) and SbPV clusters (2.66 mm/s). These lines, of comparable intensities, accounted together for more than half the Sb atoms in 4.2×10^{20}-cm^{-3} P doped Si. See also Chaps. 6 and 7.

(vi) Nylandsted Larsen *et al.* performed Sb isoconcentration diffusion experiments with isotope tracer atoms in MBE samples [82]. In 1019-°C furnace anneals, D_{Sb} was enhanced with concentration by a factor of 2.0 over the concentration range $C_{\mathrm{Sb}} = 2.5$–8×10^{18} cm^{-3}. (Above $\sim 2 \times 10^{19}$ cm^{-3}, extensive Sb precipitation and clustering started to retard the diffusion.) In comparison, literature values from Sb diffusion in As or P backgrounds predict only a factor-1.2 enhancement [38, 105]. Therefore, the observed D_{Sb} enhancement is in clear excess of that expected from a shift of Fermi level.

5.3.2 Comments

Prior to the discussion in the next section, a few comments on the above findings on impurity–vacancy clusters are due. The comments relate to item (i) and (ii) above, primarily to the latter.

Neither for P nor As nor Sb diffusion did SN [99], with the use of furnace anneals, see very a large ($> C^2$) diffusivity increase with concentration. In contrast, the very large enhancements that were reported [37] of vacancy-mediated diffusion in P backgrounds up to approximately 4×10^{20} cm^{-3} after RTA, could in fact *also* be observed after furnace anneals at comparable temperatures [106]. This fact supports the assumption that implantation damage had

not been the cause of the enhancement. And an inspection of data shows that the enhancement that was seen of Sb tracer atom diffusion in Sb backgrounds with intermediate concentrations [item (vi)] was not reproduced by SN either. Therefore, *for P and Sb backgrounds, a discrepancy seemingly exists between results extracted from indiffusion/BM analysis [99] and from the ion implantation or MBE isoconcentration-diffusion experiments [37, 106]. At the same concentrations ranges, the latter experiments reveal stronger diffusivity increases*. We see that the discrepancy is *not* a result of different annealing times or annealing types[27] as has been suggested [99, 28, 80].

For the case of Sb, the discrepancy is not easily resolved.

For the case of P, it may of course be questioned whether one should indeed expect the same strong enhancement in high-concentration P diffusion [99] as is observed for other diffusers (As, Sb, Sn, Ge) in an isoconcentration P background [37].[28] But the reason is not very clear why SN see no large enhancement with a BM analysis, whereas it was necessary for MP [88, 89] to invoke percolation in order to fit indiffused P profiles in the high-concentration regions. And it is also unclear why SN [99], at 1000 °C, obtain an n/n_{i} dependence of P diffusion that is far below linear up to as much as $\sim 3 \times 10^{20}$ cm^{-3}.

For the case of As backgrounds, isoconcentration experiments with P [36] and Sb [38] tracers have been carried out only up to $C_{\mathrm{As}} \approx 1.8 \times 10^{20}$cm^{-3}; alas, this type of experiment is not available to either corroborate or oppose the BM results [99,35] that indicate retardation at C_{As} slightly above 2×10^{20} cm^{-3}. But we do remind that other studies [95, 89, 83] indicated fast diffusion above this limit.

In view of the above, we feel that an open mind should be kept on the question of the precise equivalence between an indiffusion/BM analysis and the straight-forward isoconcentration experiments. The BM experiment [100] must meet the difficult requirement of a constant surface concentration, and the analysis rests on the assumption that $D = D(C)$ has no time dependence at any point of the profile. That is, during redistribution, local-equilibrium distributions between isolated dopants, point defects, dopant-point defect clusters, and precipitates, must adjust rapidly according to the local dopant concentration at each point of the profile. *If the equilibration time is not sufficiently short, the BM analysis may not yield the true equilibrium diffusivity as a function of concentration*. In this respect, the inherent catch-22 [107] is noted: At any point of the profile, the equilibration time should be short relative to some characteristic time that describes the change of dopant concentration – but unfortunately,

[27] Incidentally, it is not surprising if RTA diffusion does allow the same amount of thermal equilibration as furnace diffusion does: At least, the diffusion lengths of hundreds of Å [37] greatly exceed the typical dopant–dopant distance of, e.g., ~ 15 Å at 3×10^{20}-cm^{-3} doping.

[28] It would be intriguing to perform an isotope isoconcentration experiment with P, but unfortunately, all P has mass 31 so the experiment will remain a Gedanken experiment. The same goes for As with mass 75.

these two quantities are closely linked to each other, since they are both controlled by the dopant diffusivity.

5.4 Percolation or clustering?

5.4.1 Discussion

It is a central issue to clarify in which systems a collective phenomenon may dominate diffusion, and in which systems triple complexes (e.g., As_2V or $SbPV$) may be present in sufficient concentrations to either retard or enhance diffusion relative to that via the E center and/or percolation mechanisms.

Let us recall that the diffusivity of A is given by the product $D_{A_nX}C_{A_nX}$ of the diffusivity and the concentration of the mobile species (e.g., $A_nX = As_2V$). The prefactor for a given mechanism will depend on several properties: If more than one atoms are involved in A_nX, the prefactor will depend on the dopant density to a suitable power, $(C_A/C_S)^m$; for dilute solutions in thermodynamical equilibrium, $m = n - 1$. The prefactor will depend on the degeneracy z of the mobile complex, and on the entropy of diffusion as $\exp(\Delta S/k)$ where $S = S^{\mathrm{m}} + S^{\mathrm{f}}$ has both a migrational and a formational part. Also, effects of correlation goes into the prefactor: to move a large complex, a high number of A–V exchanges must be realized, the higher number, the lower the effective diffusivity. So in view of of the complexity of the prefactor for the diffusion of complexes, let us first make the point that *the relative contribution of a given mechanism can not be estimated solely on account of the enthalpy of diffusion*. Enthalpies of diffusion from theoretical work were given in Sec. 5.3.1.

To emphasize the complexity of assessing different diffusion mechanisms, we may mention that Berding and Sher [98] calculated that As_2V possesses a single and a double acceptor level in the lower and upper half of the band gap, respectively. If these levels indeed exist, the formation energy of the doubly charged $As_2V^{=}$ will be close to zero in highly n-type material [98]. But the serious shortcoming must be reminded of, that neither present-day theory nor experiment has satisfactorily shown how donor or acceptor levels scale relative to their low-temperature values, when the band gap shrinks with increasing temperature. This circumstance adds much uncertainty to defect concentrations (native defects or complex defects). Above all these considerations is still the question whether *kinematic limitations* allow true equilibration of the size distributions of impurity–vacancy complexes, such as the distributions calculated by Berding and Sher [98], e.g.

Let us now turn to experiments that may give hint to the predominance of a mechanism other than E center diffusion. Attention can first be drawn to the fact that in high-concentration P backgrounds, diffusivities obeyed approximate C_{P}^b power laws with $b \approx 3.5, 4.5, 4.4$, and ~ 5 for Sb, As, Sn, and Ge,

respectively [37] (Fig. 5.1). On account of the high power dependencies, we ruled out on p. 50 that the diffusion could be mediated via isolated E centers. We can add now that the high power dependencies can not be reasonably accounted for with a thermal-equilibrium formation of isolated *triple complexes* either: Since these must be formed through a first-order reaction, such as

$$\mathrm{Sb}V + \mathrm{P} \rightleftarrows \mathrm{SbP}V \tag{5.13}$$

or opposite (with Sb $\leftrightarrow$ P), their concentration will increase with background concentration with at most a power of $1 + 2 = 3$, where 1 is the order of the reaction and 2 is a (questionable) Fermi-level contribution.[29] Therefore, *that the diffusivities increase faster than a power 3 with P concentration is a strong indication that the diffusion is not mediated by isolated entities. Rather, the diffusion is governed by a collective phenomenon that is caused by the P-background doping*.

At the very highest dopant concentrations ($\gtrsim$ 3–5 $\times$ 10^{20} cm^{-3}), both P and As diffusion decreases [99,35] (or saturates; As at 1050 °C [99]) in furnace annealings, due to heavy clustering. It is then a dispute whether triple complexes, such as As_2V, contribute to this retardation [99,35,28] or if they form already at lower concentrations with an enhancing effect [80]. Calculated formation and migration energies for various As–vacancy configurations were summarized in Eqs. (5.7–5.12). In particular, As_2V has a very low energy of formation (0.8–1.0 eV), but a high migration energy (1.9–2.0 eV), thus, it is a *slow* migrator that may be present in *large concentrations*. If we assume at time zero of the annealing a random distribution of As, a high-diffusivity percolation network must necessarily exist at this point. But the reasoning [80,28] is of course justified from consideration of the calculated formation energies, that in the approach to thermal equilibrium, a relative shift will take place from {As atoms in AsV pairs that are members of a percolation network} to {As atoms in $\mathrm{As}_n V$ clusters, $n = 2$ (or higher)}.[30]

In agreement with the latter conclusion (that some fraction of impurity atoms must move into complexes), the probable existence of SbPV complexes was inferred [103,104] with Mössbauer after RTA of Sb implants in 4.2 $\times$ 10^{20}-cm^{-3} P backgrounds [item (v) on p. 54]. It is expected that the SbPV cluster has a low formation energy, similar as it is to As_2V. But it was argued strongly above, from the $C_\mathrm{P}^{3.5}$ dependence of D_Sb, that diffusion is dominated by percolation. So *the concentration of {Sb atoms in SbPV complexes} may be large and possibly even comparable to the concentration of {Sb atoms in SbV pairs that are members*

[29] Due to the large Coulomb repulsion, we do not consider the existence of triply charged acceptor levels. Nor do we consider it likely that complexes involving more than two atoms contribute to diffusion.

[30] Here, we use the picture that an impurity within the percolation network associates with a vacancy, AV, in order to diffuse. It should be realized that this is not the same as an *isolated* AV pair, present at low impurity concentrations (e.g., an E center). Above C^*, the vacancy is expected to spend only a relative short amount of time with each impurity.

of a 5nn percolation cluster}, – and yet, it is the much more mobile 'percolation'-SbV that is the main cause of the strongly enhanced diffusion. On the one hand, a large number of SbPV triple complexes have formed, but on the other hand, the percolation cluster is upheld with time because enough substitutional background atoms and tracer atoms (P_s and Sb_s) exist that diffusion can still proceed as a vacancy-percolation phenomenon via the vacancies that are not bound in triple complexes.

By positron annihilation [101], an indication was given of As_3V formation in very highly doped Si [item (v) on p. 54]. That result does hint that As_2V diffusion can become significant, since the As_3V formation can be conceived as

$$\underbrace{As_2V}_{\text{mobile?}} + As_s \rightleftarrows As_3V. \tag{5.14}$$

But one cannot exclude alternative formation channels that do not require mobile As_2V, for instance:

$$2\ \underbrace{AsV}_{\text{mobile}} + As_s \rightleftarrows As_3V + V. \tag{5.15}$$

Moreover, if a large portion of As had in fact deactivated by forming immobile *donor-pair* (DP) defects [108] that do *not* involve vacancies, then the concentration of As that had deactivated due to *vacancy* interaction would be smaller. As a result, one would get an average $\bar{n}$ that was smaller than the 3.2 value cited above. So *from the positron annihilation study [101] it is tenable, though not certain, that As_2V contributes to diffusion at very high As concentrations (approaching $\sim 8 \times 10^{20}\ cm^{-3}$)*.

Particular attention should finally be cast on the Sb isoconcentration experiments [82] that were mentioned in item (vi) on p. 54. At concentrations below $\sim\ 8 \times 10^{18}$ cm^{-3}, D_{Sb} was enhanced in clear excess of that expected from a shift of Fermi level. Considering the very low Sb concentrations, this enhancement can not be related to a percolation phenomenon. Instead, we note that the large-size Sb atom, for reasons of stress-compensation, has a high tendency to cluster (this is reflected in the very low solid solubility of Sb in Si, e.g. $\sim 2 \times 10^{19}$ cm^{-3} at 1000 °C [109]). For this reason, *it is very plausible that the observed enhancement of D_{Sb} with concentration [82] can be explained by increasing numbers of mobile Sb_2V complexes.* Certainly, no other mechanism can currently explain the observation.

5.4.2 Concluding remarks

Let us summarize on the above considerations: In *phosphorus* backgrounds, the large enhancements of vacancy-mediated diffusion (after both furnace annealing and RTA) [37, 106] provide good support of vacancy percolation above

2×10^{20} cm^{-3}. For *arsenic*-doped Si, possible indications of percolation enhancement are seen [83, 89] (Sec. 5.2.1), but isoconcentration experiments have not been carried out at concentrations above the percolation threshold. – At typical processing temperatures, the electrical solubility [110] of As is comparable to the percolation threshold [Eq. (5.2)], and vacancies are known to accompany deactivated As and probably also form As_3V clusters [101] at very high concentrations, thus, the significance of As_2V diffusion is not untenable. *Antimony* diffusion was accelerated significantly faster than expected from the Fermi-level change [82] already at $C_{Sb} \gtrsim 5 \times 10^{18}$ cm^{-3}. A plausible explanation is an increased dominance of diffusion via Sb_2V complexes. We pointed out apparent mismatch between diffusivities extracted from indiffusion/Boltzmann-Matano analysis and from isoconcentration diffusion experiments, respectively.

Based upon these considerations, we propose the following: A fraction of large-size atoms (Sb) will cluster into mobile Sb_2V already at low concentrations ($\lesssim 5 \times 10^{18}$ cm^{-3}), thereby enhancing the diffusion. Mid-size atoms (As) represent an intermediate case, and at the other end, the highly lattice-matched P atoms will stay in solution during diffusion such that above $\sim 2 \times 10^{20}$ cm^{-3}, they create a strongly accelerating percolation network for vacancy diffusers. At concentrations $\gtrsim$ 3–6 $\times 10^{20}$ cm^{-3} (depending on temperature and atomic size), all donor-atom species will be immobilized through extensive clustering. These conclusions stand for both furnace anneals and RTA.

5.5 The case of a Sn background

5.5.1 On the analysis

On account of the extended discussion of high-concentration diffusion (Secs. 5.2–5.4), we can carefully review and add comments to the Sn-background experiments [I] that we presented in Chap. 4. It is apparent that variations of the Fermi level has been a complicating factor in all of the above group-V experiments: The precise role of the acceptor levels of the vacancy and/or the migrating species is not well determined, and scaling the concentrations with $(n/n_\mathrm{i})^m$ ($m = 1, 2$) is performed *ad hoc* to fit the given set of data. Regarding the vacancy-percolation model, some crude simplifications were mentioned in Sec. 5.2.3. But even if accepting these simplifications, it is still critical that many assumptions must be made in order to quantify all parameters in P^∞, D^norm, and D^perc in Eq. (4.1). For example, with the parameters assumed by MP [89], in P diffusion at 1000 °C the $(n/n_\mathrm{i})^2$ term is *assumed* to become the dominant charge state term for $n/n_\mathrm{i} \gtrsim 20$ ($C_\mathrm{P} \gtrsim 1.0 \times 10^{20}$ cm^{-3}). But for P diffusion in As-backgrounds up to $n/n_\mathrm{i} = 30$ [36], no evidence was found for a diffusion component faster than the (n/n_i) term that corresponds to singly-charged de-

fects. Therefore, the Sn-background experiments are very well motivated from the fact that Sn is on the one hand known to attract vacancies (see Ref. [111] and refs. therein) but on the other hand it induces no shift of Fermi level.

Let us turn to the plot of Sb diffusivity vs. Sn-background concentrations (Fig. 4.2 of the previous chapter). We could rule out that point defect injection or strain effects could have been the cause of the observed enhancement in D_{Sb}. A fit according to the percolation model was attempted to the data of Fig. 4.2. Three features are conspicuous:

(i) The diffusivity enhancement is not as abrupt as is predicted by the percolation model

(ii) With the best possible fit according to the percolation model, a particularly low threshold is obtained:

$$C^*_{\mathrm{Sn}} = 1.0 \times 10^{20}\ \mathrm{cm}^{-3}. \tag{5.16}$$

(iii) The Sb-diffusivity increase is smaller in a Sn background than in a P background [37]. One can use Figs. 4.2 and 5.1 to extract approximately the maximum enhancement factors F [Eq. (5.3)] when C exceeds C^*. One finds in the respective systems,

$$F_{\mathrm{Sn}} \approx 3.5 \ \text{ and } \ F_{\mathrm{P}} \approx 30. \tag{5.17}$$

Points (i) and (ii) lead us to conclude that a mechanism other than vacancy percolation is responsible for the Sb-diffusivity increase. In particular, in the percolation framework, a low threshold C^* could have been envisaged if the impurity–vacancy potential had been of extraordinary *long* range – such that, e.g., the barrier for V escape from impurity A was lowered by the presence of impurity A' in a 6nn rather than a 5nn position. Obviously, the interpretation that a collective vacancy phenomenon sets in at a lower concentration for a Sn-background concentration than for a P one, would be controversial since the Sn–V potential is only elastic and expected to be of short range. In contrast, we know for a fact (from the Fermi-level diffusivity increase) that the E centers are either neutral or singly negatively charged at high concentrations, such that we have Coulomb-type P^+V^- or even $\mathrm{P}^+V^=$. The *ab initio* binding energies for P^+–V^- are $\Delta E_{i,PV} = 1.05, 0.59$, and 0.47 eV for neighbour separations $i = 1, 2, 3$, respectively (see reference in [112]).

From the diffusion-enhancement factor [point (iii)] and Eq. (5.4), we can follow MP and make an experimental estimate of the 2nn binding of the PV pair: $\Delta E_{2,PV} \approx 0.39$ eV. This value is not very dissimilar from the 0.59 eV cited above. If the E center is in reality negatively charged at high doping levels, 0.39 eV will be an underestimation of $\Delta E_{2,PV}$. For Sn, we can use the reverse

line of thought: *If* the Sn–V range of interaction were of sufficient range, then percolation would be induced. So if we did assume percolation, we could use $F_{\mathrm{Sn}} \approx 3.5$ to estimate the Sn–V 2nn binding to $\Delta E_{2,\mathrm{Sn}V} \sim 0.14$ eV. However, since we *reject* the idea of percolation, the value rather represents an upper limit:

$$\Delta E^{\mathrm{max}}_{2,\mathrm{Sn}V} \sim 0.14 \text{ eV}. \tag{5.18}$$

This is a small value; it shows that the potential must fall off rapidly with Sn–V separation. $\Delta E_{3,\mathrm{Sn}V}$ will be even smaller, so at a 3nn separation the Sn–V binding will be much weaker than that of a group-V atom–vacancy pair. We therefore conclude, cf. Eq (2.47), that *the activation energy of Sn–vacancy pair diffusion should be larger than that of group-V diffusion via vacancies*, and this is indeed in accordance with experiment [42, 21].

The paradox that we discussed on p. 21 is drawn up again: The short-range Sn–V binding lead us to expect that Q_{Sn} be equal to or slightly smaller than the activation energy for Si self-diffusion via vacancies, Q^{self}_V. Yet, accepted values are $Q_{\mathrm{Sn}} = 4.91$ eV and $Q^{\mathrm{self}}_V = 4.1$–$4.2$ eV (Secs. 2.4.3 and 2.4.1). On p. 21 we hinted at the possibility that Q^{self}_V is in reality higher than 4.1–4.2 eV; this was also the conclusion of Ural *et al* [18].

Very recently, density-functional supercell calculations were performed by Kaukonen *et al.* [54] on the interaction potential of the neutral Sn–V pair. In agreement with the calculations by this author (p. 21), Kaukonen *et al.* obtain $E^{\mathrm{b}}_{\mathrm{Sn}V} = 1.2$ eV for the binding energy and find that the lowest energy-configuration is the (D_{3d}-symmetry) Watkins configuration. For the binding energies at different neighbour separations, Kaukonen *et al.* obtain $\Delta E_{1,\mathrm{Sn}V} = 0.6$ eV, $\Delta E_{2,\mathrm{Sn}V} = 0.3$ eV, and $\Delta E_{3,\mathrm{Sn}V} \sim 0.03$ eV. So indeed, the Sn–V interaction is very short-range. Moreover, the calculated value $\Delta E_{2,\mathrm{Sn}V} = 0.3$ eV is in fair agreement with the experimental estimate $\Delta E^{\mathrm{max}}_{2,\mathrm{Sn}V} \sim 0.14$ eV, not least considering the simplicity of the estimate.

5.5.2 A final word on Sn precipitation

It is in place to elaborate somewhat on the matter of *Sn precipitation* (– and reassure that it does not play a role for the diffusion experiments!). After the 995-°C anneals, precipitates had formed in all samples that had $C_{\mathrm{Sn}} \geq 1.2 \times 10^{20}$ cm^{-3}. TEM micrographs showing precipitates are given in Fig. 5.5. We demonstrated (Figs. 4.3 and 4.4, pp. 38, 39) that the Sn precipitation did not cause a vacancy injection, hence we could exclude that the precipitate formation had contributed to the observed D_{Sb} enhancement. Moreover, rough statistics on the sizes and densities of the precipitates are presented here, in Tab. 5.1. These quantities are sufficiently small that the far majority of Sb

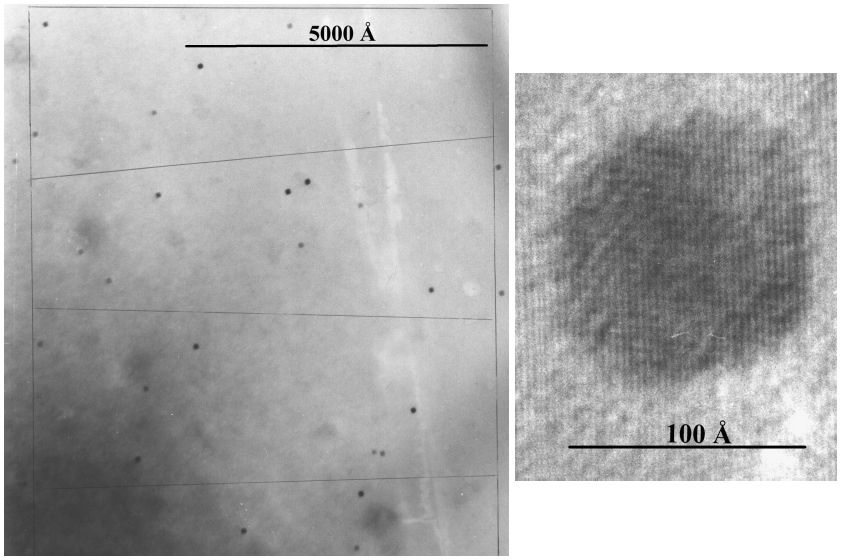

Figure 5.5: TEM micrographs from plan-view samples showing Sn precipitates after annealing at 995°C/1h. The sample had $C_{\mathrm{Sn}} = 4.7 \times 10^{20}$ cm^{-3}. Left: Low magnification (the lines are pencil marks). Right: Closeup of one precipitate; the vertical direction is $\langle 110 \rangle$.

C_{Sn} (cm^{-3})	as-grown	1 h anneal		3 h anneal	
	f (%)	f (%)	d (nm)	f (%)	d (nm)
5.5×10^{19}	0	0		0	
1.2×10^{20}	0	$\sim$ 0.02–0.1	$\sim$ 8	$\sim$ 0.001–0.003	$\sim$ 3–5
2.3×10^{20}	0	$\sim$ 0.5–0.6	$\sim$ 10	$\sim$ 0.6–0.7	$\sim$ 5–15, 15–18
3.3×10^{20}	0	$\sim$ 0.7–0.8	$\sim$ 10	$\sim$ 0.6–0.8	$\sim$ 5–15, 15–18
4.6×10^{20}	0	$\sim$ 0.7–0.8	$\sim$ 10	$\sim$ 0.3–0.6	$\sim$ 5–15, 15–18
4.7×10^{20}	0	$\sim$ 0.3–0.4	$\sim$ 10	$\sim$ 0.7–0.8	$\sim$ 5–15, 15–18

Table 5.1: Sn precipitation after annealing at 995 °C, estimated from plan-view TEM micrographs. C_{Sn} is the Sn concentration in the box profile, f is the precipitated fraction of Sn atoms, and d is the typical precipitate dimension. (For calculation of f, it was assumed that the atomic density in precipitates is $\rho = \rho_{\alpha\text{-Sn}} = 2.92 \times 10^{22}$ cm^{-3}.)

atoms can be considered to diffuse freely, interacting seldom with the precipitates. For example, consider the sample with $C_{\mathrm{Sn}} = 4.6 \times 10^{20}$ cm^{-3}: After a 1-h/995°C anneal, roughly 0.7–0.8 % of the Sn atoms have gone into the precipitates, which have been formed with a typical dimension (side length) of 10 nm. Incidentally, the density of precipitates after this annealing is roughly 1.1×10^{14} cm^{-3}, which corresponds to an inter-precipitate distance of $\sim 2.1 \times 10^3$ Å. This distance is large compared with the corresponding diffusion length $l_{\mathrm{Sb}} \sim (2D_{\mathrm{Sb}}t)^{1/2} = 5.0 \times 10^2$ Å.

After 3 h annealing, precipitates have ripened and the overall density seems to be slightly reduced relative of that after 1 h. Of the precipitates that exist after the 3-h anneal, a significant fraction have grown to a size of 15–18 nm, but others have dissolved partially or they are still growing (sizes 5–15 nm). Of the smallest precipitates, the density is higher near the depth of the Sn box profile and near the sample surface; this is inferred from the comparative study of thick and thin regions of specially prepared, wedge-shaped plan-view samples. This depth effect is due to the reduced Sn concentration after diffusion into the bulk and dose loss at the surface, as is seen in the Sn profile of Fig. 4.1. Irrespective of the above details, however, the relevant conclusion of the TEM study is that the fraction of Sn atoms that have precipitated does not increase significantly with time; at all times and in all samples the fraction remains below 1 %.

In relation to the Sn precipitation, one conclusion from the article [I] that was presented in the previous chapter needs slight adjustment: A short-time ($\lesssim$ 1 h) retardation of Sb marker-layer diffusion on the deep side of a 3.3×10^{20} cm^{-3} Sn box was observed (Fig. 4.4). – This need not, as first stated [I], be an indication that the Sn precipitation process causes injection of Si self--interstitials [which was thought to reduce the vacancy concentration near the Sb marker layer through interstitial–vacancy (I–V) recombination]. The I–V recombination time at 995 °C is namely on the order of days, so a perturbation of C_I should not change C_V over the experimental times of a few hours. Therefore, the observation instead shows that the Sn layer rapidly ($\lesssim$ 1 h) attracts vacancies, as a result of which the equilibrium vacancy concentration C_V^* in the *vicinity* of the Sn box is only slowly attained. It is probable that the vacancies are attracted due to the generation of SnV pairs and Sn$_2V$ complexes, similarly to the case of Sb complex formation that is discussed in Chaps. 7 and 6.

Chapter 6

Article: Si self-interstitial injection from Sb complex formation in Si

J. Fage-Pedersen, P. Gaiduk and A. Nylandsted Larsen, J. Appl. Phys. **88**, *3254 (2000)* [III].

Abstract

It has recently been established that Si self-interstitials are generated during annealing of high-concentration Sb layers in Si. In the present work we make use of samples grown with molecular-beam epitaxy (MBE). We monitor, at different times and temperatures, the diffusion enhancement or retardation of deep B or Sb marker layers next to a 1.1×10^{20} cm^{-3} Sb box, as well as the formation of Sb precipitates within the box. It is concluded that the interstitials are not associated with precipitate growth, but that they are generated from formation of Sb–vacancy complexes, primarily involving 2 Sb atoms.

6.1 Introduction

The understanding of complex formation and precipitation in highly doped Si has proved to be a perpetual challenge in microelectronic research. Samples with above-solubility concentrations of substitutional dopants can be prepared by standard techniques (e.g., molecular-beam epitaxy [113], chemical vapor deposition [114] or laser melt annealing [58]), but unfortunately these layers are meta-stable, hence at elevated temperatures complex formation and precipitation may (i) put a limit to the maximum level of electrical activation, and (ii) potentially generate excess point defects, thereby affecting dopant diffusion in the vicinity of the highly doped layer.

Physically, the pursuit is for the microscopic structure of the compensating defects and the behaviour of these in terms of formation and/or migration ki-

netics. For the case of group-V dopants, as dealt with in this paper, increasing amounts of evidence indicate that formation of small impurity–vacancy complexes plays the strongest role, but the picture is complicated by the coexistence of precipitates within high concentration layers of Sb [115] or As [110].

Most work on complex formation has been done on As in Si. According to theory, As_3V [116,80] and, in particular, As_4V [116,80,98] clusters (V denoting a vacancy) are energetically favoured over isolated As, and As_2V has a positive, but low energy of formation [80]. On the experimental side, extended x-ray fine structure (EXAFS) measurements [117] of laser-annealed, highly As-implanted Si, showed that the average number of Si nearest neighbours to As-atoms dropped from $\sim$ 4 to $\sim$ 3 after annealings below $\sim$ 650 °C. It has recently been suggested, from positron annihilation experiments [118], that the dominant vacancy defect in Cz-grown 1×10^{20} cm^{-3} As-doped Si, is As_3V. (Somewhat surprisingly, 1×10^{20} cm^{-3} P-doped Cz-Si contained no vacancy defects.) Also with the use of positron annihilation, an increase of vacancy concentration was observed after 750 °C deactivating anneals of 8×10^{20} cm^{-3} laser-annealed As layers in Si [101]. The increase was attributed to the formation of As_nV clusters, where an average $\bar{n} > 2$ was estimated from comparison of the vacancy complex concentration with the deactivated As-concentration. In another experiment [58], a release of Si self-interstitials was observed from laser-annealed As layers in a range of concentrations above 2.3×10^{20} cm^{-3}. At 750 °C the interstitial generation had good temporal correlation with the As deactivation, and the generation and the deactivation was explained via interstitial kick-out from As_nV cluster formation, $n = 1...4$.

Sb differs from As by having a much lower solubility limit in Si [119, 109], and electrically inactive Sb consists simultaneously of precipitates and vacancy-related clusters [115]. A 2.66 mm/s Mössbauer line of Sb implants in high P backgrounds was attributed to Sb-P-V complexes [104] since it increased with P concentration. In 2×10^{15} cm^{-2} and 5×10^{15} cm^{-2} implanted Sb samples, a 2.32 mm/s line from one Sb atom in vacancy surroundings coexisted with a broadened precipitate line of 2.74 mm/s, but in view of the above, it seems likely that the 2.74 mm/s precipitate line contains also a contribution from Sb_2V. EXAFS [102] has revealed large concentrations of Sb–vacancy complexes (supposedly with two vacancies) as well as precipitates, present already after laser-annealing of 5×10^{16} cm^{-2} Sb implants. We previously demonstrated [II] that interstitial fluxes were released from high-concentration Sb layers, but whereas we speculated that the interstitials may be generated from formation of Sb–vacancy complexes, the data allowed only the conclusion that the generation occurred in those samples where the Sb concentration was high enough for precipitates to form. We may note that on the basis of EXAFS, a novel class of donor-pair defects (DP(2) and DP(4)), involving neither vacancies nor Si self-interstitials, have been suggested to dominate the deactivation

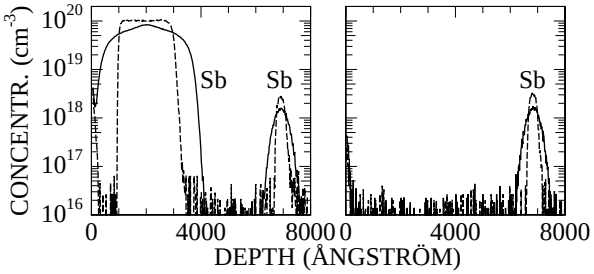

Figure 6.1: Examples of MBE structures; as-grown (dashed lines) and diffused at 950 °C for 2 h (solid lines). Profiles of a B spike next to an Sb box were shown in Ref. [II].

in *as-grown*, 1.5×10^{21} cm^{-3} Sb-doped low-temperature ($\lesssim$300 °C) molecular-beam epitaxy (LT-MBE) samples [108]. That the majority of defects could have been the particularly stable Sb_4V was ruled out, but this still allows for formation of Sb_nV complexes after annealing.

In this article, with refined experiments and analysis, we extract new information from diffusion studies of B or Sb marker layers situated on the deep side of high-concentration Sb box profiles in Si [II]. Typical profiles are depicted in Fig. 6.1. In most measurements in Ref. [II] a 1.6×10^{20} cm^{-3} Sb box was employed, and transmission electron microscopy (TEM) showed that some fraction of the large interstitial flux agglomerated in interstitial dislocation loops within the Sb layers. Presently, we use samples with a 1.1×10^{20} cm^{-3} Sb box, in which no interstitial loops are observed after annealing at any temperature. Therefore, if we neglect the possibility of self-interstitial trapping in small clusters [120] then the diffusivity enhancement D/D^* in the B spikes, assumed to be equal to the local interstitial supersaturation C_I/C_I^*, can now be used as a good indicator of the injected number of interstitials. Also, we perform a thorough count of precipitates and demonstrate that B diffusion, particularly at low temperatures, is enhanced on a time scale much smaller than that on which the Sb atoms form precipitates. From this fact, and from simple estimates of the injected number of interstitials, we conclude that the interstitials are not generated from Sb precipitation, but from Sb_nV-complex formation, where $n = 2$, on the basis of our data, is believed to dominate.

6.2 Experiment and results

The samples, used also in Ref. [II], were MBE-grown on <100> Si, at a substrate temperature of 550 °C. They were diffused in an N_2 ambience in a flow

furnace, at temperatures ranging from 822 °C to 1020 °C and durations between 10 min and 12 h. Chemical profiles were measured with an Atomika 4000 secondary-ion mass spectrometry (SIMS) instrument, sputtering the samples with 3.5 keV O_2 molecules at an angle of 30° off-normal, and crater depths were measured with a Dektak profilometer. A number and size count of Sb precipitates, as well as a search for interstitial dislocation loops and voids was performed with TEM, using a Philips CM20 microscope operating at 200 kV.

After various anneal times t_i at each fixed temperature, the total time-averaged diffusion coefficient D_{0,t_i} was extracted by numerically letting the as-grown, measured profile evolve into the diffused one, according to Fick's 2nd law. The specific diffusion coefficient D_{t_{i-1},t_i} within time interval $[t_{i-1}, t_i]$ was then calculated from the relation

$$D_{0,t_i} t_i = D_{0,t_{i-1}} t_{i-1} + D_{t_{i-1},t_i}(t_i - t_{i-1}).$$

Fig. 6.2 shows B marker layer diffusivities vs. time, in samples with and without the 1.1×10^{20} cm^{-3} Sb box. The Sb box causes an interstitial injection that transiently enhances the B diffusion above the intrinsic value;[31] at 822 °C the transient dies out within ~ 8 h, and at 971 °C within $\sim 2\frac{1}{2}$ h.

In Fig. 6.3, in the temperature range 822-1020 °C, we present the 30 min time-averaged diffusion coefficients of B, under intrinsic and under interstitial-injection conditions, respectively. The measured diffusivity under injection conditions, $D_{0,30\text{min}}$, has been split into a sum of two components: The intrinsic component $D^*_{0,30\text{min}}$ is from a B spike in plain Si, and the injection component is then $D_{0,30\text{min}} - D^*_{0,30\text{min}}$. Assuming the injection component to be thermally activated, a fit to the data gives an activation energy for $D_{0,30\text{min}} - D^*_{0,30\text{min}}$ of only 0.52 ± 0.34 eV.

From a comparison between the B diffusion enhancement and the number $N_{\text{Sb}}^{\text{prec}}$ of Sb-atoms that have gone into precipitates after various temperatures, we may now establish that the interstitial generation is not a consequence of the Sb precipitate formation:

$N_{\text{Sb}}^{\text{prec}}$ was investigated from a precipitate size- and density count performed with plan-view TEM after 30 min annealings in the temperature range 850-1000 °C (fig. 6.4). Apart from an effect of saturation at the highest temperature, $N_{\text{Sb}}^{\text{prec}}$ displays Arrhenius behaviour with activation energy 4.07 ± 0.18 eV. This value being identical to that of Sb diffusion [43] demonstrates that Sb precipitation in Si is diffusion limited. After 30 min at, e.g., 822 °C (extrapolating from

[31] The measured values of the B diffusion coefficient in pure Si are slightly higher than reported in the literature [121], and the reason is currently not understood. However, the constancy with time of the diffusion coefficient indicates that our MBE material contains no in-grown point defects, as may exist in LT-MBE samples [122]. And if any effect upon B diffusion, of the rather high C contamination in MBE material (in ours, typically $C_C \lesssim 10^{18}$ cm^{-3}), it would rather have been a *retarding* one due to I trapping [87]

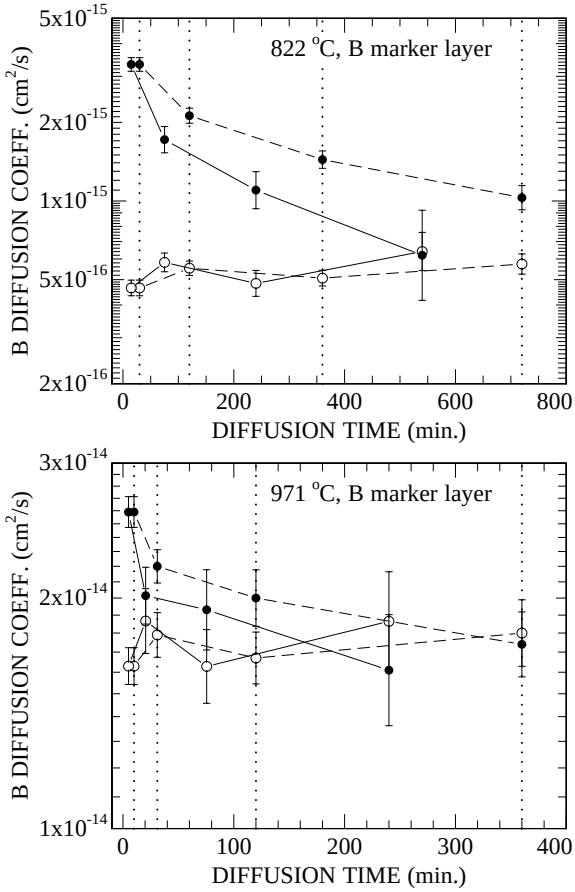

Figure 6.2: B diffusion vs. time, at 822 °C and 971 °C in samples with (•) and without (○) an 1.1×10^{20} cm^{-3} Sb box. Dashed lines are total, time-averaged diffusion coefficients and solid lines are specific diffusion coefficients within the indicated time intervals. Error bars are from the fitting procedure only; uncertainties in time, temperature, and depth calibration are not included since samples with and without an Sb box were always co-annealed, and for each structure all the diffused profiles were adjusted to agree with the same as-grown profile.

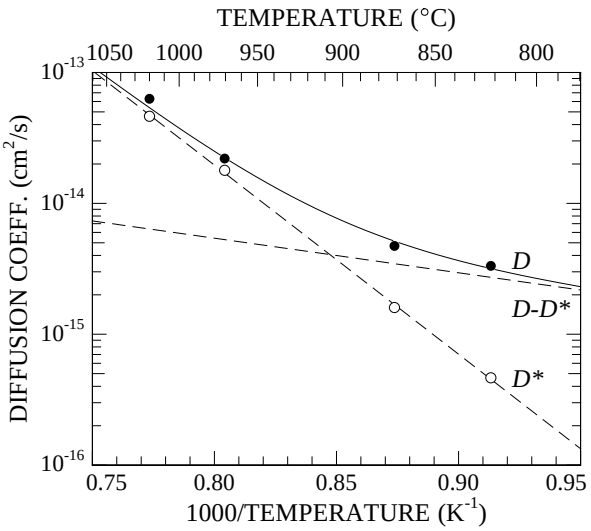

Figure 6.3: 30 min time-averaged diffusion coefficients of B, vs. temperature, in structures with (•) and without (○) an Sb box. The solid curve is a sum of the two dashed lines.

the figure) the total precipitate volume is 2 orders of magnitude below that at which the growth starts to saturate, hence at this temperature the growth is expected to proceed steadily for days. In comparison, the B diffusion enhancement at 822 °C has died out completely after $\sim$ 8 h (fig. 6.2). Moreover, it is apparent that the temperature dependence of $N_{\mathrm{Sb}}^{\mathrm{prec}}$ (fig. 6.4) is far stronger than that of $D_{0,30\mathrm{min}} - D^*_{0,30\mathrm{min}}$ (Fig. 6.2). Some care should be taken here though, since the small activation energy of $D_{0,30\mathrm{min}} - D^*_{0,30\mathrm{min}}$ is in part due to fast interstitial loss to the surface at high temperatures, as detailed below. From this discussion we conclude that the self-interstitial injection is not caused by Sb precipitation.

It is natural, then, to suggest that the interstitials are generated during an Sb-point defect complex formation that may take place at an early stage of annealing, as a precursor to precipitate formation. Similar to the As deactivation mechanism suggested by Rousseau *et al.* [58], one may picture a donor-assisted Frenkel-pair generation via

$$\mathrm{Sb}_n\mathrm{Si} \rightarrow \mathrm{Sb}_n V + I, \tag{6.1}$$

where n Sb atoms ($n = 1...4$) kick out a Si atom and make it a self-interstitial I, as illustrated in Fig. 6.5. It is clear that the process is beneficial if the Sb atoms

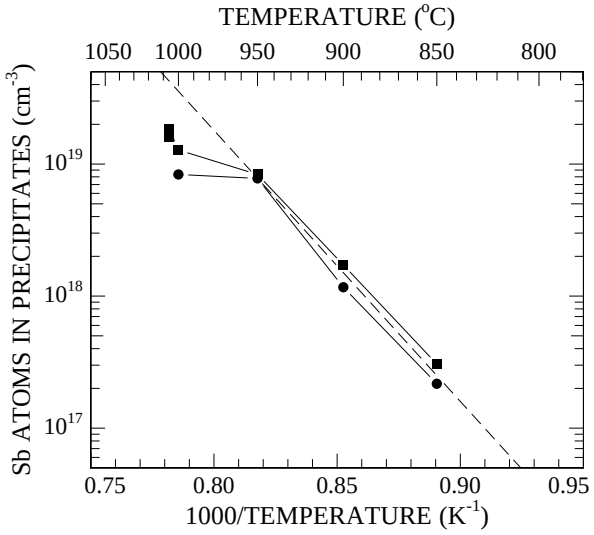

Figure 6.4: Number of Sb atoms in precipitates after 30 min annealings. Samples had an Sb box with a concentration of either 1.1×10^{20} cm^{-3} (●) or 1.6×10^{20} cm^{-3} (■).

can revert the ionized, fourfold coordinated $5sp^3$ state to the native, threefold $5s^2p^3$ neutral state in the vicinity of the vacancy. Relative to As, the large-size Sb atom will additionally gain from a larger stress-relaxation. E.g., the formation energy of As_2V is 0.82 [80], but for for Sb_2V it may be close to zero, or process (6.1) may even be exothermic. (In comparison, AsV and SbV binding energies differ by approximately 0.3 eV [26].)

Assuming that the Sb atoms have a purely random distribution in the as-grown layers, we may calculate the statistically expected number N_{Sb_n} (n=1...4) of Sb_n configurations per cm^3 that will potentially participate in (6.1). N_{Sb_n} can then be compared with an estimate of the number N_I^{inj} of interstitials that are injected per cm^3 in the Sb box. The random-distribution assumption will be reasonable for epi-layers grown at intermediate and low temperatures, and for laser-annealed layers: On the one hand, Sb atoms do not clump together from growth with a non-random distribution, since MBE layers with as much as 3×10^{20} cm^{-3} Sb could be fully activated upon 10 s anneals at 600 °C or 800 °C [113]. For As, laser-annealing has provided very high electrical activity [58]. And on the other hand, these highly doped layers are metastable at long times or high temperatures [113, 58], which means that the dopant distribution during fabrication of the materials has been frozen in before it was fully

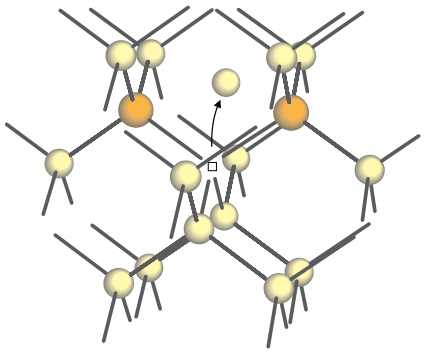

Figure 6.5: Sb_nV complex formation by interstitial kick-out, illustrated for $n = 2$. Atoms up to 2nn sites from the vacancy (□) have been drawn.

equilibrated through dopant-dopant and/or dopant-point defect interactions.

It is likely that an Sb_2V complex will be formed by interstitial kick-out whenever 2 Sb atoms in the as-grown sample form a configuration of either 1st or 2nd nearest neighbours (1nn or 2nn). Taking into account that each site has 4 1nn-sites and 12 2nn-sites (Fig. 6.5) and dividing by 2 since each pair may equally well be related to 2 sites, the number of such Sb_2 configurations is then

$$\begin{aligned} N_{Sb_2} &\approx \left(\frac{4p^2}{2} + \frac{12p^2}{2}\right) C_S \\ &= 1.9 \times 10^{18}\ \mathrm{cm}^{-3}, \end{aligned} \tag{6.2}$$

where $p = C_{Sb}/C_S$, $C_{Sb} = 1.1 \times 10^{20}\ \mathrm{cm}^{-3}$ and $C_S = 5 \times 10^{22}\ \mathrm{cm}^{-3}$.

Of Sb_3 configurations that may turn into Sb_3V with relative ease, let us consider (i) those in which all three Sb atoms are within {some lattice site i or one of i's 4 1nn sites}, and (ii) those in which the Sb atoms occupy site i and a 1nn site to i, plus one of those 9 2nn to this site that is not also a 1nn to i [otherwise the configuration would fall under (i)]. Thus,

$$\begin{aligned} N_{Sb_3} &\approx \left[\binom{5}{3} p^3 + 4 \times 9 \times p^3\right] C_S \\ &= 2.5 \times 10^{16}\ \mathrm{cm}^{-3}. \end{aligned} \tag{6.3}$$

On the other hand, we can estimate the generated number N_I^{inj} of interstitials per cm^3, integrated from time 0 to time t. This can be done since the majority of the interstitials that are generated in the box will be lost to the surface rather than to the bulk, and we can estimate the interstitial out-flux from the box towards the surface: If the surface acts as a perfect sink for interstitials, the flux will be given roughly by $D_I(C_I - C_I^*)/R$, where D_I is the Si self-interstitial diffusivity, $C_I - C_I^*$ is the concentration of excess interstitials near the Sb box,

Table 6.1: Number N_I^{inj} of generated Si self-interstitials (10^{18} cm^{-3}) after various times and temperatures. Errors are from $D_{0,t}/D^*_{0,t}$ uncertainties.

	822 °C	871 °C	971 °C	1020 °C
10 m			1.1±0.1	4.3±1.0
30 m	0.08±0.01	0.23±0.02	1.4±0.4	11.5±5.0
2 h	0.15±0.02	0.42±0.05	4.5±2.3	
6 h	0.29±0.04	0.35±0.18	-2.3±5.0	
12 h	0.25±0.07			

and $R \approx 1840$ Å is the average depth of the Sb box, measured from the surface. Since the interstitial gradient towards the *depth* of the sample will be much smaller, we may ignore the loss of interstitials in this direction, and substitute for C_I/C_I^* at the Sb box, the measured D/D^* values in the B spike (fig. 6.2). The integrated flux must then equal $N_I^{\text{inj}}d$, where $d \approx 1800$ Å is the thickness of the Sb box, i.e.

$$\begin{aligned} N_I^{\text{inj}} &\approx \int_0^t \frac{D_I\,(C_I(t') - C_I^*(t'))}{Rd}\,dt' \\ &= \frac{D_I C_I^*}{Rd}\int_0^t \frac{D(t') - D^*(t')}{D^*(t')}\,dt' \\ &= \frac{D_I C_I^*}{Rd}\,\frac{D_{0,t} - D^*_{0,t}}{D^*_{0,t}}\,t, \end{aligned} \tag{6.4}$$

where $D_I C_I^* = 3 \times 10^{25} \exp(-4.8\text{ eV}/kT)$ cm^{-1}s^{-1} [10].

In view of the simple analysis, the results (Table 6.1) should be taken with some precaution, but they show that N_I^{inj} increases with both annealing time and temperature, and after the longest annealing times, $N_I^{\text{inj}} \sim (0.25 - 12) \times 10^{18}$ cm^{-3}. At 822 °C and 871 °C some saturation takes place with time. It is likely that the injection at 971 °C and 1022 °C have indeed saturated within the time windows used, but the data has large uncertainties.

The expected number of Sb_2V complexes that are likely to be formed by an interstitial kick-out process, Eq. (6.2) falls well within the measured numbers of injected interstitials (Table 6.1). Conversely, the number of Sb_3V, Eq. (6.3), is lower by almost two orders of magnitude at the Sb concentration used in our experiments. In fact, using Eqs. (6.2) and (6.3) we would require $C_{\text{Sb}} = 9 \times 10^{21}$ cm^{-3} before $N_{\text{Sb}_3} = N_{\text{Sb}_2}$, i.e. even though Sb_3V has a low formation energy, the statistical abundance of Sb_3 configurations will be too small to sig-

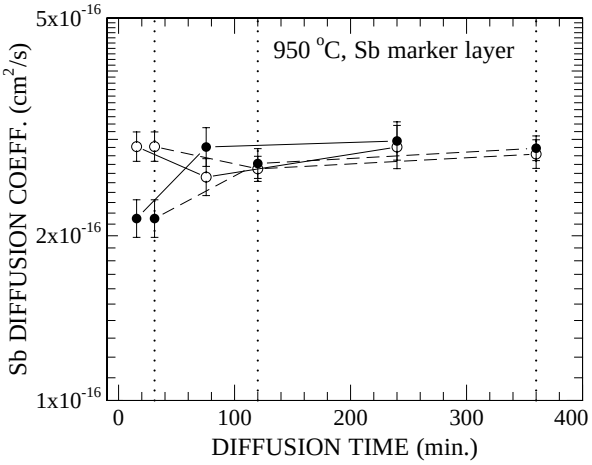

Figure 6.6: Sb diffusion at 950 °C, vs. time. Comments as in Fig. 6.2.

nificantly contribute to interstitial kick-out, even at the highest-obtainable Sb concentrations.

One unresolved question remains: Following the rapid complex formation and interstitial release, the slower build-up of a precipitated Sb phase proceeds via SbV and probably also Sb_2V migration (this precipitation mechanism, as has been discussed [II], differs fundamentally from the well-studied one of oxygen precipitation). As the number of these pairs and complexes decreases, a corresponding release of vacancies should then take place, and it could be anticipated that diffusion in an adjacent Sb marker layer be enhanced at long times. But as is evident from fig. 6.6, at 950 °C this vacancy release either does not occur or is too slow to significantly affect the diffusion of an Sb marker at long times (6 h). With TEM a search for vacancy accumulation in the form of voids gave no result either. What is seen in fig. 6.6 is an initial ($<$ 30 min) diffusivity *decrease*. This can be due either to I-V recombination, since C_I is initially high, or, perhaps more likely as discussed below, to a transient vacancy drainage in the neighbourhood of the Sb box.

6.3 Discussion

Let us first address the fact that the equilibrium concentration of free vacancies outside the box is perturbed. Since the highly doped Sb-layer attracts vacancies to a high concentration, a vacancy drainage in the neighbourhood of the Sb box

(Fig. 6.6) is quite conceivable. We need therefore emphasize that the very long I-V recombination times (of at least a few days at 950 °C, e.g. [123]) ensures that C_I and C_V should be considered as being essentially independent of each other. Therefore, even if a V drainage occurs, this drainage is *not* the cause of the significant increase in C_I.

The statistically expected number N_{Sb_2} of Sb_2 pairs that may perform donor-assisted Frenkel-pair generation is in agreement with the estimated number N_I^{inj} of released interstitials. At $C_{\mathrm{Sb}} = 1.1 \times 10^{20}$ cm^{-3} only a very small fraction of Sb deactivates upon annealing [124], possibly consistent with the precipitated fraction, but at higher concentrations a considerable fraction of inactive Sb will be formed, both as vacancy-related complexes and as precipitates [115].

But it is clear from Eqs. (6.2) and (6.3) that at no concentration will enough $\mathrm{Sb}_n V$ complexes, $n \geq 2$, be created by I kick-out to account for a measurable deactivation of Sb; not even if one considers mobile $\mathrm{Sb}_n V$ to subsequently pair with isolated Sb atoms.[32] So the scenario is that a number of $\mathrm{Sb}_n V$ clusters (the majority with $n = 2$) are indeed formed by I kick-out, but the bulk of the deactivating Sb–vacancy clusters can only be formed from vacancies that are Schottky-generated at the surface in order to approach thermodynamic equilibrium concentrations of $\mathrm{Sb}_n V$, $n = 1...4$. Mobile $\mathrm{Sb}V$ pairs are continually formed as the first step; they will then pair with substitutional Sb to form mobile $\mathrm{Sb}_2 V$ and subsequently $\mathrm{Sb}_3 V$ and/or $\mathrm{Sb}_4 V$ if permitted by kinetics.

The discussion whether vacancies are supplied from the surface or from I kick-out is of course equally valid for As in Si. Now, in the experiment of Rousseau *et al.* [58], the time transients of As deactivation rate and B diffusion enhancement were found to be closely correlated. But rather than the conclusion that deactivation is caused by $\mathrm{As}_n V$ formation via I kick-out, their results really indicate that the $\mathrm{As}_n V$ formation time scales (total number of clusters per time, summed over n) are similar for the I kick-out process and for the process where vacancies are created via the Schottky process. In fact, if applying Eq. (6.4) to the data of Rousseau *et al.* one finds that the interstitial generation per cm^3 from a 2.3×10^{20} cm^{-3} As box at 750 °C is slightly less than the one that we measure from the 1.1×10^{20} cm^{-3} Sb box at 822 °C. So despite a large concentration of deactivated As (1.6×10^{20} cm^{-3} after 16 h at 750 °C) the interstitial generation does not exceed that from the Sb-box where only an insignificant concentration deactivates at 822 °C [124].

Equilibrium distributions between As pairs involving no vacancies, and As complexes involving one or two vacancies have been presented by Berding and Sher [98], based on a statistical mechanical analysis, using *ab initio* total energies and treating simultaneously the chemical and the electronic subsys-

[32] We may note that in highly *As*-doped material, all $\mathrm{As}_n V$ complexes, $n = 2, 3, 4$ have been suggested [98] to remove the same number of electrons, viz. 4, from the conduction band.

tems. In true equilibrium, As_4V is concluded to dominate deactivation, concentrations of DP(2) and of the negative-energy defects As_3V and As_6V_2, being somewhat smaller.

Let us stress that whereas Chadi *et al.* [108] suggested the no-vacancy DP defects to dominate the deactivation in as-grown, 1.5×10^{21} cm^{-3} Sb-doped LT-MBE samples, no investigation was made of annealed samples. Upon annealing the majority of defects may well be Sb_nV; indeed, the formation of DP defects alone would not give cause to a release of point defects.

Let us also mention that short-time (15 min) retardation of Sb marker layer diffusion has been observed in the vicinity of a 3.3×10^{20} cm^{-3} Sn-box [I]. Here the underlying mechanism is Sn–vacancy complex formation. But looking at retardation rather than enhancement, a quantitative comparison with Sb_nV or As_nV complex formation is very difficult.

6.4 Summary

We have demonstrated diffusion enhancement in the temperature range 822-1020 °C of a B marker layer on the deep side of a 1.1×10^{20} cm^{-3} Sb box in a Si MBE structure. The enhancement is not correlated in temperature with Sb precipitate formation. Rather, we suggest that the enhancement is caused by interstitial kick-out from a formation of Sb_nV complexes, mostly with n=2 since the number of injected interstitials, from a simple estimate, is compatible with the statistically expected number of Sb_2V complexes that may be formed by interstitial kickout. However, it is argued for group-V impurities in general, that the majority of impurity–vacancy complexes are not created in kick-out processes, but rather through capture of vacancies generated at the surface.

Acknowledgements

This work was supported by the Danish Natural Science Research Council. Thanks are due to Scott Dunham for valuable comments.

Chapter 7

Comments on Sb-complex formation

A short description is given on the background of the experiments [III] that were presented in Chap. 6, and some of the main conclusions are drawn up.

7.1 Precipitation and complex formation

The significance of the size of group-V atoms in Si is particularly visible in the differences of the solid solubilities of the different atoms. Least soluble among P, As, and Sb are the large-size Sb atoms, and consequently, Sb in Si will constitute a complicated system at high concentrations, since a precipitated phase can occur upon annealing and coexist [115] with Sb atoms in smaller complexes as well as Sb in substitutional form.

In a first set of annealing experiments [II], prior to the experiments presently reported [III], it was seen that during annealing, Si self-interstitials are injected from MBE-grown high-concentration Sb layers. The effect upon the diffusion in a B marker is quite significant; this can be appreciated from Fig. 7.1. TEM inspections were performed on samples with different Sb box concentrations that had undergone annealing under various conditions of time and temperature, and it could be seen [II] that the B diffusion enhancement is correlated with the appearance of Sb precipitates. In Fig. 7.2, examples of TEM images are shown.

A more quantitative analysis of the B diffusion enhancement was conducted in article [III]. In particular, simple statistics was applied to estimate the number N_I^{inj} of injected interstitials from the integration over time of the B diffusion enhancement D/D^* [Eq. (6.4) and Tab. 6.1]. In order to estimate the true number of released interstitials, it was critical that the interstitials had not been trapped in interstitial dislocation loops. Such loops can be seen in Fig. 7.2 (c). Since no loops formed in the samples with $C_{\text{Sb}} \leq 1.1 \times 10^{20}$ cm^{-3}, we could in fact use the 1.1×10^{20}-cm^{-3} Sb box for the statistical study.

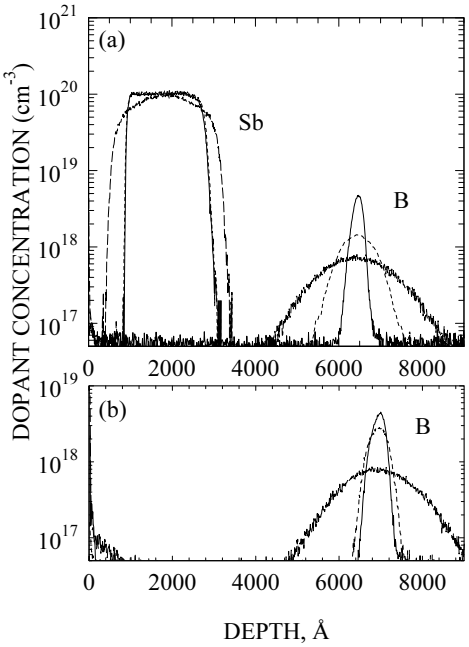

Figure 7.1: SIMS profiles of B-spike MBE structures (a) with and (b) without a 1.6×10^{20} cm^{-3} Sb box. Three different structures have been overlapped: As-grown (solid line), annealed 800 °C/30 min (short-dashed), and annealed 1000 °C/30 min (long-dashed). From [III]

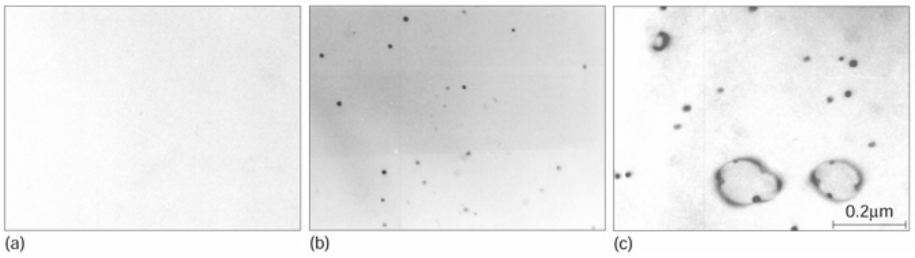

$C_{Sb} = 6 \times 10^{19}$ cm^{-3} 1.1×10^{20} cm^{-3} 1.6×10^{20} cm^{-3}

Figure 7.2: TEM plan-view images, recorded after 900 °C/30 min anneals. The samples contained B spikes and Sb-box profiles with the indicated concentrations. Interstitial dislocation loops are observed only at $C_{Sb} = 1.6 \times 10^{20}$ cm^{-3}, and Sb precipitates are observed only at 1.1×10^{20} cm^{-3} and 1.6×10^{20} cm^{-3}. From [III].

7.2 The kickout reaction

The conclusion was reached [III] that the I release, transient in time, and with only modest temperature dependence (Fig. 6.3) was *not* related to the growth of precipitates. But the measured number of interstitials that are released after long times [$N_I^{\text{inj}} \sim (0.25\text{–}12) \times 10^{18}$ cm^{-3}] corresponds roughly to the statistical number [$N_{\text{Sb}_2} = 1.9 \times 10^{18}$ cm^{-3} (6.2)] of Sb_2 configurations that are likely to participate in the *kickout reaction*

$$\text{Sb}_2\text{Si} \rightarrow \text{Sb}_2V + I. \tag{7.1}$$

The calculation of N_{Sb_2} relies on the assumption that the Sb atoms, according to the maximum-entropy principle, are randomly distributed in substitutional configurations in the as-grown material. One could consider also that a small fraction of Sb atoms were *interstitially* placed in the asgrown sample. That could give cause for I injection via the first-order reaction $\text{Sb}_\text{i} + \text{Si} \rightarrow \text{Sb}_\text{s} + I$. But two observations speak against this picture: (i) From the first-order reaction, one would anticipate a *linear* increase of the I injection with C_{Sb}, but in fact, D/D^* increases much more rapidly [II] with C_{Sb}. (ii) The interstitial configuration Sb_i enforces much local strain on the lattice and appears an improbable configuration.

Much of the relevant literature on complex formation has been reviewed on pp. 51–54. When analysing the evolution of complex distributions, there is one important conclusion [III] that one should be aware of: Whereas large numbers of, e.g., $\text{Sb}_n V$ and $\text{As}_n V$ complexes ($n = 1...4$) may form in thermal equilibrium, only a small fraction of these are formed in *Frenkel*-type kickout processes as discussed there. – The largest fraction of complexes are formed via vacancies that are *Schottky*-generated at the surface and subsequent cause migration of E centers and/or migration of triple complexes.

Chapter 8

Diffusion of P and B in strained and relaxed Si and SiGe

Preliminary results are presented on the diffusion of P delta profiles in MBE-grown SiGe heterostructures. Recent results by Zangenberg and coworkers [V] on B diffusion in similar systems are included in the discussion. In the different heterostructures, the Ge content x and the biaxial strain ϵ in the diffusion layer were varied independently of each other. The strain conditions were compressive, relaxed, and tensile, and the Ge contents ranged from 0 to 40 % for P samples and from 0 to 24 % for B samples. Our results support the proposition [125] of a pairing between B and Ge in SiGe alloys. For each combination (x, ϵ) of Ge content and strain, the prefactors $D_{x\epsilon,0}$ and the enthalpies $H_{x\epsilon}$ in $D_{x\epsilon} = D_{x\epsilon,0} \exp(-H_{x\epsilon}/kT)$ have been obtained. $D_{x\epsilon,0}$ changes by several orders of magnitude with x and ϵ, but the quantity is very closely linked to $H_{x\epsilon}$ through a compensation effect (the Meyer-Neldel rule). This result poses a strong contrast to vacancy-mediated diffusion in strained and relaxed SiGe.

8.1 Introduction

SiGe is rapidly finding its way into microelectronics. For example, in a heterojunction bipolar transistor (HBT), B doped SiGe excels in use as a base layer material in-between a Si emitter and collector. In such a device, rapid electron transfer can be obtained across the base region, enabling very high speed. At the same time, the power consumption is low, thus, high-performance SiGe based devices seriously challenge GaAs in the market of RF circuits used in, e.g., wireless communication. And very crucially: at equivalent performances, SiGe devices can be manufactured at one-fifth the cost of a GaAs [4], and since

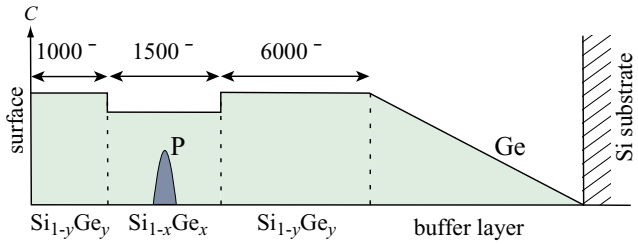

Figure 8.1: Schematic of a strained SiGe heterostructure with a P spike, grown by compositional grading. In this schematic, the $Si_{1-x}Ge_x$ layer contains tensile strain and the $Si_{1-y}Ge_y$ layers are relaxed.

the technology is Si-based, SiGe can be integrated in CMOS[33] circuits that are used for digital logic.

From a physics-point of view, a heterojunction introduces phenomena that are not encountered in a uniform bulk material. A band discontinuity is present and, as a consequence, an electric field is generated in the junction region. Also, biaxial strain is induced when layers of different free lattice parameters are in epitaxial contact. In this work, we address the critical issue of dopant redistribution in $Si_{1-x}Ge_x$ as a function of biaxial strain ϵ and Ge content x. Delta layers with P and B doping, respectively, have been incorporated in thin (approximately 1500 Å) $Si_{1-x}Ge_x$ layers sandwiched in-between $Si_{1-y}Ge_y$ layers, as depicted schematically in Fig. 8.1. If $x \neq y$, the thin $Si_{1-x}Ge_x$ layer will be strained since the in-plane lattice constant is forced to be equal to that of the $Si_{1-y}Ge_y$ substrate layer. Since the delta layers have adequate separation to the junctions, complications of segregation [126, 127] during diffusion do not occur.

We should remark at this point, with regret, that the work presented here is still ongoing and it is not yet in a mature state. The baseline diffusion coefficients that we have obtained for B and P in Si are higher than the literature values, an issue that has caused much concern. Various test experiments now point to unintentional surface oxidation during annealing as the cause of the enhanced diffusivities (details are given below). To eliminate these perturbations, a large part of the diffusion measurements will be repeated in a foreseeable future. We have concluded that the most reliable, inert diffusion can be obtained by depositing on the samples an oxide top layer and capping with a thin nitride.

For the reasons given, the discussion of the data in this chapter will serve to primarily outline some interesting physical phenomena. A full and more detailed treatment will await the production of a refined set of data.

[33] CMOS: Complementary metal oxide semiconductor

8.2 Quantification of strain and compositional effects upon diffusion

Let us first define the *tensile strain* ϵ in the center layer (the 'x' layer) of the heterojunction. It is given by

$$\epsilon = -2\frac{a_x - a_y}{a_x + a_y} \approx -\frac{a_x - a_y}{a_y}. \tag{8.1}$$

This is the elastic strain that arises from the lattice mismatch when the free (relaxed) lattice parameters at the respective compositions are a_x and a_y, respectively. $\epsilon < 0$ corresponds to *compressive* strain ($a_x > a_y$). The additional strain contribution that arises from different thermal expansion coefficients of the x and the y layers can usually be ignored [128]. The interpolation between $a_0 \equiv a_{\mathrm{Si}} = 5.431$ Å and $a_1 \equiv a_{\mathrm{Ge}} = 5.658$ Å is given by [128]

$$a_x = [5.431 + 0.1992x + 0.02733x^2]\text{Å} \tag{8.2}$$

$$\approx [5.431 + 0.227x]\ \text{Å} \tag{8.3}$$

where the linear approximation is known as Vegard's law. Using the approximations in (8.1) and (8.3), the simple formula is obtained:

$$\epsilon \approx -0.0418(x - y). \tag{8.4}$$

Though this formula is commonly used, the precise expression for ϵ was used in the P studies.

Cowern and coworkers [129] observed that Si(Ge) interdiffusion increased exponentially with strain. The exponent varied inversely with temperature, thus, the diffusivity $D_{x\epsilon}$ as a function of strain ϵ and composition x was enhanced relative to the diffusivity D in relaxed Si ($x = 0$, $\epsilon = 0$) as

$$\frac{D_{x\epsilon}}{D} = \exp\left(-\frac{Q'\epsilon}{kT}\right). \tag{8.5}$$

Q' has the dimension of energy per unit strain. In expression (8.5), effects of *both* composition and strain upon the diffusivity have been lumped into the quantity Q', the reason being that Cowern *et al.* did not see evidence of a chemical driving force for Si(Ge) interdiffusion, thus, Q' was believed to largely reflect an effect of strain. Eq. (8.5) implies that the activation energy of diffusion at given strain and composition can be extrapolated from the value Q in relaxed Si as

$$Q_{x\epsilon} = Q + Q'\epsilon, \quad Q' = \frac{dQ}{d\epsilon}. \tag{8.6}$$

However, if chemical and strain effects can be separated, a much more transparent change of the activation energy is provided by using instead of $Q'\epsilon$ the right-hand side of the following equality [130]:

$$Q'\epsilon = Q'_\epsilon \epsilon + Q'_x x. \tag{8.7}$$

In the experiments to be reported below, Arrhenius investigations have been made for each combination $(x, x-y)$. Thus, we obtain the prefactors $D_{x\epsilon,0}$ and diffusion activation enthalpies $H_{x\epsilon}$ in the expression

$$D_{x\epsilon} = D_{x\epsilon,0} \exp\left(-\frac{H_{x\epsilon}}{kT}\right) \equiv D'_{x\epsilon,0} \underbrace{\exp\left(\frac{S_{x\epsilon}}{k}\right) \exp\left(-\frac{H_{x\epsilon}}{kT}\right)}_{\exp\left(-\frac{G_{x\epsilon}}{kT}\right)}. \tag{8.8}$$

Here, we also defined the prefactor $D'_{x\epsilon,0}$ which contains the jump length, the attempt frequency, and a geometric factor, but *no* entropy term. To first order, we will expect that $H_{x\epsilon}$ is linear in both x and ϵ,

$$H_{x\epsilon} = H + \Delta H_{x\epsilon} = H + H'_\epsilon \epsilon + H'_x x, \tag{8.9}$$

and the general expression for the diffusivity $D_{x\epsilon}$ relative to the diffusivity D in relaxed Si, will be

$$\boxed{\frac{D_{x\epsilon}}{D} = \frac{D'_{x\epsilon,0}}{D'_0} \frac{\exp\left(\frac{S_{x\epsilon}}{k}\right)}{\exp\left(\frac{S}{k}\right)} \exp\left(-\frac{H'_\epsilon \epsilon + H'_x x}{kT}\right).} \tag{8.10}$$

In this formula, of course, one can substitute for the value D (which is for Si) a more general value $D_{x'\epsilon'}$ to compare two composition/strain combinations (x, ϵ) and (x', ϵ'). In the following, the term 'activation energy' will be frequently be used instead of 'activation enthalpy'.

8.3 Experimental details

The heterostructures were fabricated with MBE on Si <001> substrates. A schematic of a structure was given in Fig. 8.1, and SIMS profiles of an as-grown and a diffused P spike in strained SiGe are given in Fig. 8.2. To achieve strain-free $Si_{1-y}Ge_y$ layers with a low density of structural defects, the compositional grading technique was used: A graded *buffer layer* is initially grown, in which the Ge content is increased by 10 %/μm. The buffer layer is grown at 750 °C with 4 Å/min. In this layer, strain is relieved due to the generation of a large number of misfit dislocations inside the layer. The top layers, with stepwise uniform doping ($Si_{1-x}Ge_x$, $Si_{1-y}Ge_y$), are grown at 570 °C. The P spike is

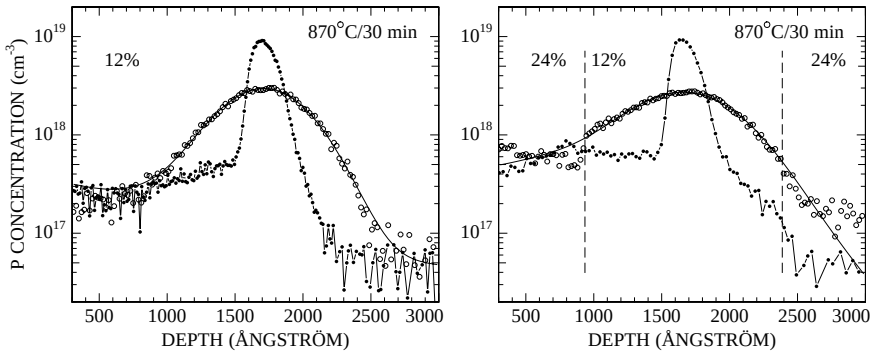

Figure 8.2: SIMS profiles of as-grown and diffused P spikes in $Si_{0.88}Ge_{0.12}$ with no strain (left) and with tensile strain (right). Solid lines are Fick's-law fits. The diffusion was at 870 °C/30 min, oxidizing atmosphere. A constant background-count rate in the SIMS signal was subtracted.

incorporated with 1 keV P^+ in-situ implantation during growth, and B is evaporated from an effusion cell (Chap. 3). In pure Si, lower-energy (500 eV) P^+ implantation has also been tested and no difference is seen on the P diffusion, thus, effects of implantation damage are not severe.[34]

The composition of the SiGe layers was checked with Rutherford-backscattering spectrometry, and the concentration calibration of the P and B ion yields in SIMS (primary beam 3.5 keV O_2^+ at 20° off-normal) was performed by comparison with P and B implants of known doses. For the P delta layers, relatively high peak concentrations $C_P^{peak} = 1.0 \times 10^{19}$ cm^{-3} were necessitated by the high background count rate in SIMS, which is at the level corresponding to almost 1×10^{18} cm^{-3}. This background is due to the $^{30}Si^1H$ mass interference on ^{31}P; a Cs^+ primary beam and/or detection of secondary P molecular species did not provide higher dynamic range.

Furnace annealing was performed in an Argon flow. It was confirmed with TEM that as-grown, strained samples were free of misfit dislocations at the $Si_{1-x}Ge_x/Si_{1-y}Ge_y$ interfaces. Thus, the 'x' layers were pseudomorphic to the 'y' layers and fully strained. The strained P samples were grown with higher misfit $|x - y|$ than the B samples, and to minimize relaxation during annealing, a recipe similar to that by Fitzgerald [131] was employed on the P set: Mesas of dimension 500×500 μm^2 were fabricated by photolithography and chemical etching of the as-grown samples. After annealing, the SIMS profiling was

[34] To check for implantation-induced defects, a 3×10^{16} cm^{-3} uniform As layer was previously MBE-grown with the same technique (1 keV in-situ As^+ implantation). In this layer, the concentration of DLTS-active defects was found to be less than one-thousandth the doping.

performed within one of the mesas. During annealing, strain can partially be relieved through the generation of a square crosshatched network of *misfit dislocations* at the $Si_{1-x}Ge_x/Si_{1-y}Ge_y$ interfaces. With TEM, it can be estimated that the misfit dislocations emanate primarily at the deeper SiGe/Si interface. The average inter-dislocation distance p in compressively strained $Si_{0.88}Ge_{0.12}$ on Si was estimated with the use of planar samples: After 900 °C/30 min, $p \approx$ 14–28 μm. This value of p corresponds to a reduction of strain, $|\Delta\epsilon|$, of only 0.5–1 %; $\Delta\epsilon$ may be calculated [132] since the Burger's vector of a misfit dislocation corresponds to the collapse of one atomic layer. $|\Delta\epsilon|$ was also estimated after 750 °C/4 h, here it was more than an order of magnitude lower. *Threading segments*, extending from either of the interfaces and terminating at the surface, had a density below 10^6 cm^{-2} upon a 900 °C/30 min anneal of $Si_{0.88}Ge_{0.12}$ on Si. From experience [43,85] a low density is also expected in the remainder of the samples. Threading dislocations at a density below 10^7 cm^{-2} are not expected to affect interstitial-type diffusion [133]. In conclusion, these investigations ascertain that the diffusion proceeds in a matrix of high structural quality in a well-determined state of strain and with no influence of dislocations.

It should be mentioned that the measured *temperatures* deviate less than 4 °C from the true temperature, as was checked with the melting point of Ge (tabulated value 937 °C). Temperatures are reproducible within ±1.5 °C.

8.4 Results and discussion

8.4.1 Effect of a surface cap

It is in place to elaborate first on the problem that was mentioned, of the P and B base line diffusivities presently obtained in pure Si. The bulk of the annealings have been performed with no protective capping of the samples but the native oxide. Normal Fick's-law broadening of the profiles is observed and, at 850 °C, bare-surface annealing yields diffusivities D_P and D_B that exceed Fair's values [34] by factors of 11 and 4, respectively. At the same temperature, if the surface has a protective cap of either {1000 Å nitride} or {1000 Å oxide followed by 1000 Å nitride} (with no discernible difference), D_P and D_B are found to be, respectively, 4 and 2.2 times greater than literature values [34]. These results indicate that the flow furnace, albeit using very-high purity gas and being equipped with a carefully sealed chamber with gas in- and outlet through thin ($\sim$ 300 μm diameter) stainless steel tubes, does not provide sufficient purity for inert annealing. With ellipsometry it was seen that a native $\sim$ 25 Å oxide layer grew to $\sim$ 42 and $\sim$ 49 Å after 1 and 4 h at 900 °C, respectively, and whereas the observed diffusivity enhancements seem larger than would have been expected for this modest rate of oxide growth [134], the natural decision

x (%)	Activation energy Q (eV), prefactor D_0 (cm^2/s)			
	$x-y=$ -12 % (tens)	$x-y=$ 0 % (rel)	$x-y=$ 7 % (comp)	$x-y=$ 12 % (compr)
0	3.38 ± 0.14 2.3 ± 3.4	2.65 ± 0.17 $(1.3 \pm 2.3) \times 10^{-3}$		
0		$\left[\begin{array}{c} 2.87 \pm 0.09 \\ (5.1 \pm 5) \times 10^{-3} \end{array}\right]$		
7		3.04 ± 0.13 $(4.8 \pm 6.6) \times 10^{-2}$	3.03 ± 0.06 $(3.4 \pm 2.2) \times 10^{-2}$	
12	3.45 ± 0.10 5.6 ± 5.9	2.96 ± 0.06 $(2.6 \pm 1.7) \times 10^{-2}$		2.96 ± 0.07 $(2.1 \pm 1.5) \times 10^{-2}$
24		3.20 ± 0.12 $(3.5 \pm 4.3) \times 10^{-1}$		3.12 ± 0.20 $(1.2 \pm 2.6) \times 10^{-1}$
40		3.81 ± 0.31 $(3.1 \pm 11) \times 10^{2}$		

Table 8.1: Parameters for P diffusion in strained and relaxed $Si_{1-x}Ge_x$. Samples had no protective cap, except for the the square-bracket entry where samples had been masked with 1000 Å nitride. The errors are statistical uncertainties from the least-squares fitting.

has been made to proceed in the future with a twin-layer oxide/nitride cap.[35] However, in the experiments reported here, most diffusions were performed with no protective capping but the native oxide.

8.4.2 Diffusion coefficients

Phosphorus

Most of the Arrhenius plots obtained for P diffusion (in bare-surface samples) are displayed in Fig. 8.3. The plots cover various conditions of strain and composition, $0 \leq x \leq 0.4$. The extracted activation energies and prefactors are given in Tab. 8.1, and the activation energies have been plotted in Fig. 8.4. In pure Si, the P diffusion coefficients from a nitride-capped sample have also

[35] It has been reported [135] that at elevated temperatures, strain will arise beneath a nitride that is deposited directly on Si. This is due to the different thermal expansion coefficients of the two materials. To circumvent the problem, an oxide should first be deposited before the nitride, to accommodate the strain. However, from a few test measurements, these authors did not detect a difference upon B diffusion, between the use of a nitride and an {oxide+nitride} cap.

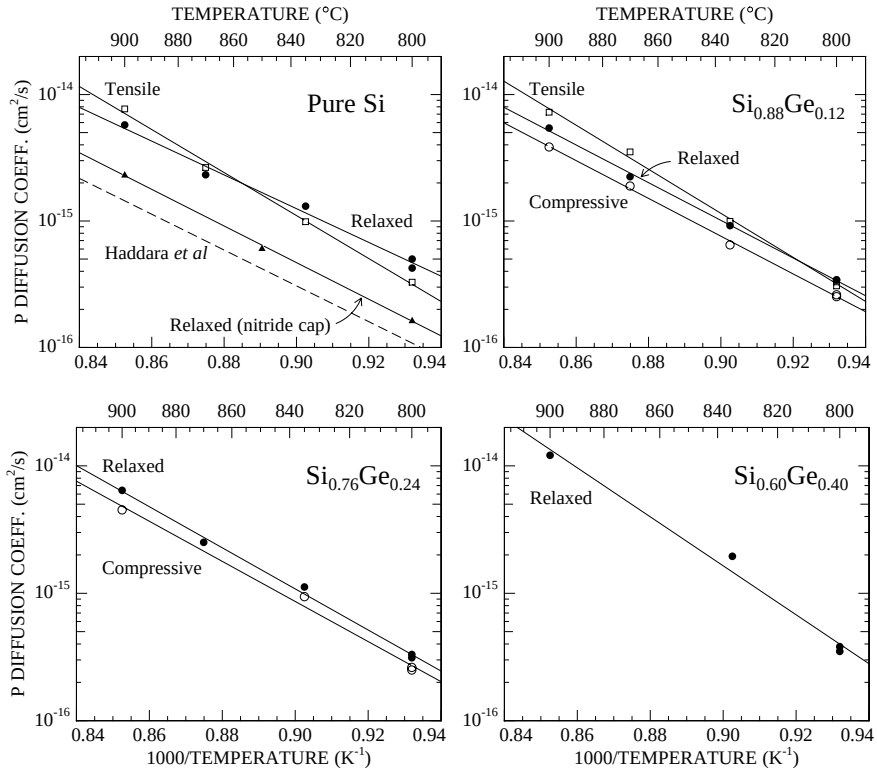

Figure 8.3: P diffusivity in strained and relaxed $Si_{1-x}Ge_x$. All samples were annealed with bare surfaces, except for one pure-Si sample that had been nitride capped prior to annealing. Values from Haddara *et al.* [136] for pure Si have also been inserted.

been plotted in Fig. 8.3, and they are compared with the very recent measurements of Haddara *et al.* [136], performed in a comparable temperature range. The activation energy (2.87 eV) agrees well with that obtained by Haddara, claimed [136] to have been meticulously obtained, but it is lower than the accepted value of 3.66 eV [34]. The reason for the discrepancy is not clear.

The scales in all four plots of Fig. 8.3 are identical; it can be seen that by varying x and ϵ, relatively small perturbations are induced on the diffusion coefficients. Relative to $(x = 0, \epsilon = 0)$, variations of the diffusivity are within a factor of ~ 2 over the investigated temperature range (800–900 °C).

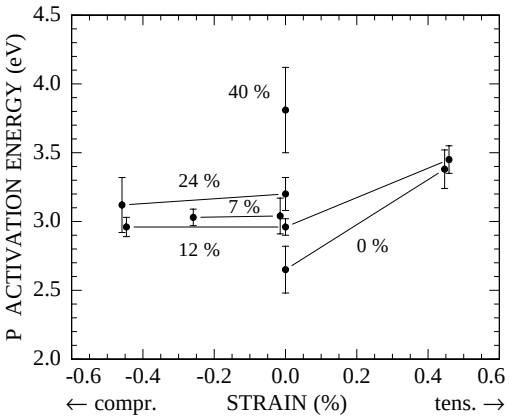

Figure 8.4: Activation enthalpies of P diffusion in strained and relaxed $Si_{1-x}Ge_x$, with x values indicated in the figure. Samples had been annealed with bare surfaces. To avoid overlaps in the figure, the point for relaxed $Si_{0.93}Ge_{0.07}$ has been slightly offset horizontally.

Boron

In contrast, Kuo *et al.* [125] found that the diffusivity of *boron* decreases significantly with x in relaxed $Si_{1-x}Ge_x$. At 800 °C, D_B reaches a minimum value at $x \approx 0.4$ that is one order of magnitude smaller than D_B in pure Si [125]. This was a surprising observation in view of the fact that B diffusion in pure Ge at 800 °C is a couple of orders of magnitude larger than in Si. Kuo *et al.* proposed that mobile B atoms, B_m, perform a pairing interaction with Ge, such that the paired B atoms, B_p, become immobile:

$$B_m + Ge \rightleftarrows B_p \tag{8.11}$$

The proposed interaction (8.11) is easily motivated, since it can be driven by a local strain compensation between B and Ge.

It is natural to compare B diffusion with P diffusion since P also diffuses via an interstitial-related mechanism in Si. It has been shown [137] that this mechanism still dominates for P diffusion in $Si_{0.87}Ge_{0.13}$. From simple strain and size considerations, P and B atoms differ in the respect that it will be less favourable for a P atom to pair with Ge. *Therefore, the observation that D_P does not decrease with Ge content whereas D_B does, is in support of the proposed B–Ge pairing model [125].*

This conclusion finds further corroboration in the results presently obtained [V] on B diffusion in SiGe. B diffusivities in strained and relaxed $Si_{1-x}Ge_x$, $0 \leq x \leq 0.24$, are presented as Arrhenius plots in Fig. 8.5, and the extracted activation energies are displayed in Fig. 8.6. (For a table of the activation energies and prefactors of B diffusion, refer to Ref. [V].) In particular, at the investigated temperatures, D_B is decreased roughly by a factor 2 from Si to $Si_{0.99}Ge_{0.01}$. In view of the small Ge content, this finding is likely to be an indication that B

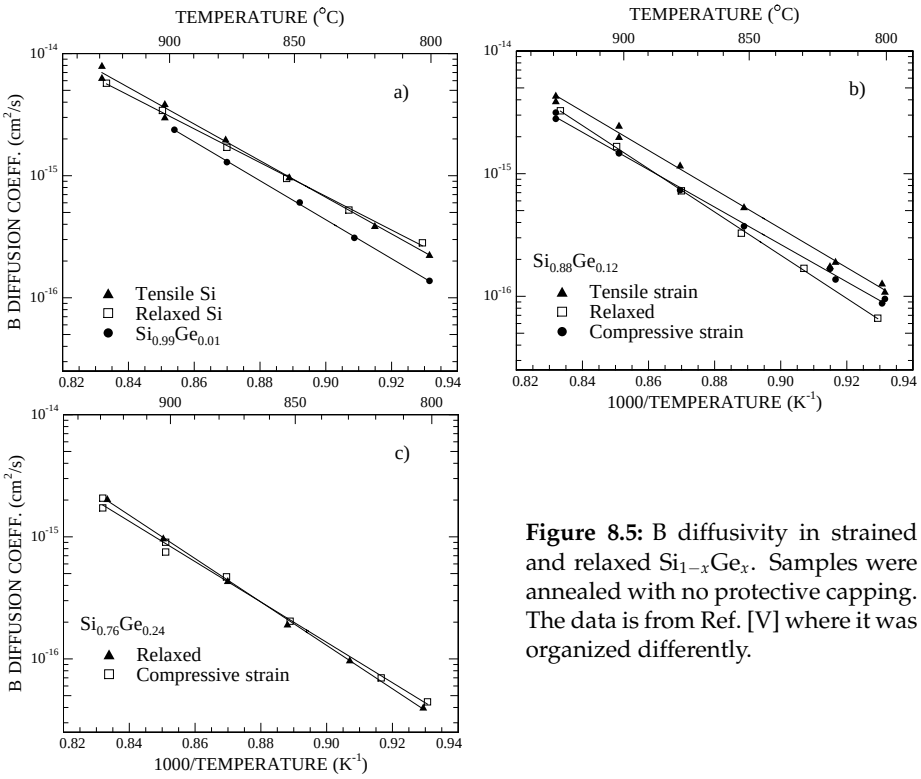

Figure 8.5: B diffusivity in strained and relaxed $Si_{1-x}Ge_x$. Samples were annealed with no protective capping. The data is from Ref. [V] where it was organized differently.

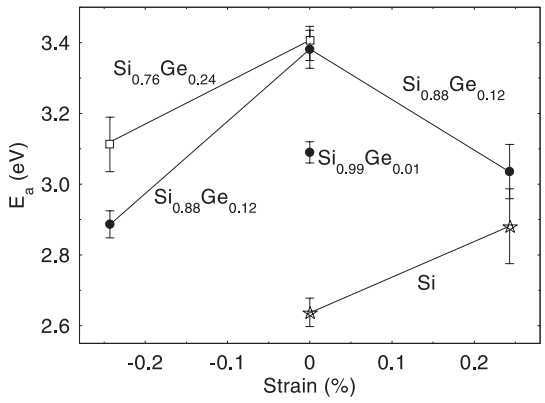

Figure 8.6: Activation enthalpies of B diffusion in strained and relaxed $Si_{1-x}Ge_x$ from bare-surface anneals. From [V].

atoms interact easily with Ge. In terms of the *activation energy*, Q_B, an increase of approximately 0.4 eV is observed from Si to $Si_{0.99}Ge_{0.01}$. In a microscopic picture, a possible interpretation is that the activation energy increase reflects an increase of the barrier for B migration if a B atoms is near a Ge atom. For a test of this interpretation, one should compare with P diffusion in a similar low-Ge content sample ($Si_{0.99}Ge_{0.01}$); unfortunately, such a sample is not available.

8.4.3 The effects of strain and Ge content

In Figs. 8.4 and 8.6, the activation energies for P and B diffusion, respectively, were plotted as a function of biaxial strain and Ge content. Some care must be taken in the interpretation of these results, since the diffusion coefficients are perturbed due to the unintended oxidation (Sec. 8.4.1). Nevertheless, we feel that the following observations are valid irrespective of this perturbation.

With increasing *Ge content*, the activation enthalpies increase for both diffusers. In the case of P in relaxed material, the activation energy Q_P increases from 2.65 eV in Si to 3.8 eV in $Si_{0.4}Ge_{0.6}$. On the Ge side, the activation energy is 2.5 eV [138], thus, Q_P goes through a maximum somewhere in the interval $0.4 \lesssim x < 1$. The same trend appears to hold for B diffusion [V,125].

The effect of *strain* is significant for both B and P diffusion, though no simple trend emerges: For P diffusion in all alloys, compressive strain induces a slight retardation (Fig. 8.3), yet it does not change the activation energy. On the other hand, with tensile strain the activation energy is significantly increased. In pure Si, the increase is quite remarkable: from 2.65 to 3.38 eV. This increase corresponds to a value

$$H'_\epsilon(\text{P in Si,tensile}) = +162 \text{ eV per unit strain} \tag{8.12}$$

as is obtained from Eq. (8.10) with $x = 0$. For B diffusion a more complex picture emerges since the effect of tensile strain upon the activation energy is opposite in Si (increase of Q) to that in $Si_{0.88}Ge_{0.12}$ (decrease of Q). The effect of compressive strain in SiGe is to decrease the activation energy.

For the case of *vacancy*-mediated diffusion in strained material [85,129], the change in activation enthalpy with strain, ΔH_ϵ, is much smaller than what is presently observed for B and P. As a consequence, Arrhenius plots that are obtained under different strain conditions can be fitted with the *same prefactor*, i.e., the assumption is used [85, 129] that the changes in diffusivity are due to (minor) strain-induced changes in the Boltzmann factor [see Eqs. (8.5) and (8.7)]. In this way, Kringhøj and Nylandsted Larsen [85] found for Sb diffusion in strained Si and SiGe,

$$Q'_\epsilon(\text{Sb in Si,tensile}) = +17 \text{ eV per unit strain}, \tag{8.13}$$

$$Q'_\epsilon(\text{Sb in } Si_{0.88}Ge_{0.12}\text{,compr.}) = +13 \text{ eV per unit strain}. \tag{8.14}$$

If the chemical effect is also included, the obtained $Q'_{x,\epsilon}$ [85] is close to that obtained by Cowern *et al.* [129] for Si(Ge) interdiffusion. Whether Q'_ϵ reflects a change, as a function of strain, in the *enthalpy* H_ϵ, or a change in the *free energy* G_ϵ depends on the assumptions made about the prefactor: If the entropy term S_ϵ/k is assumed to be the same for all ϵ values, Q'_ϵ will correspond to an enthalpy change. If S_ϵ/k is assumed to change with ϵ, Q'_ϵ will correspond to a free-energy change. (The same goes for Q'_x and the change with x.)

In any case, we see that the effect of strain upon interstitial-mediated diffusion (P, B) in Si and $Si_{1-x}Ge_x$ is quite different than on vacancy-mediated diffusion (Sb). *For the interstitial-mediated diffusers, large changes occur in* both *the activation enthalpy* $H_{x,\epsilon}$ *and the prefactor* $D'_{x\epsilon,0}\exp(S_{x,\epsilon}/k)$. And in fact, as we have seen above, the large changes in these quantities are induced not only by strain but also by Ge content.

8.4.4 Coupling between the entropy and the enthalpy

It turns out that the microscopic nature of the diffuser (interstitial- or vacancy-type) has a very profound thermodynamic consequence for the coupling between the diffuser and the lattice. In Fig. 8.7, we have plotted the prefactors $D_{x\epsilon,0}$ and the activation enthalpies $H_{x\epsilon}$ for various diffusers in strained and relaxed Si and SiGe. It is striking that *for the interstitial-mediated diffusers (P, B), an intimate coupling (semi-log relation) exist between the prefactor and the activation enthalpy*. For the vacancy-mediated diffusers, either the coupling is far weaker (Sn), or it appears to not exist (Sb).

The coupling is known in the literature as the Meyer-Neldel Compensation Rule [139], and it has been observed in several systems. In the most simple case, the compensation rule will apply if a proportionality exists between the change in the entropy and the change in the activation energy of diffusion:

$$\frac{\Delta S_{x\epsilon}}{k} = \alpha \Delta H_{x\epsilon}, \tag{8.15}$$

where α is a proportionality factor. Under simplifying assumptions, the relation can be deduced in a very simple and elegant manner [140]. The diffusing atom must pick up the energy H from a reservoir of phonons, and the entropy S is given by the number of ways that those phonons that are susceptible to participate in the process, can be assembled. The relationship (8.15) is then easily deduced [140] on the assumption that the (simple) Einstein model can be used to describe the atomic vibrations.

Very interestingly, whether the change in $\Delta H_{x\epsilon}$ for the interstitial-type diffusers is due to strain (ϵ) or due to chemical effects (x), the coupling to the phonons is unaltered. It remains, however, to understand the microscopic explanation as to why the vacancy-type diffusers do not couple strongly to the lattice.

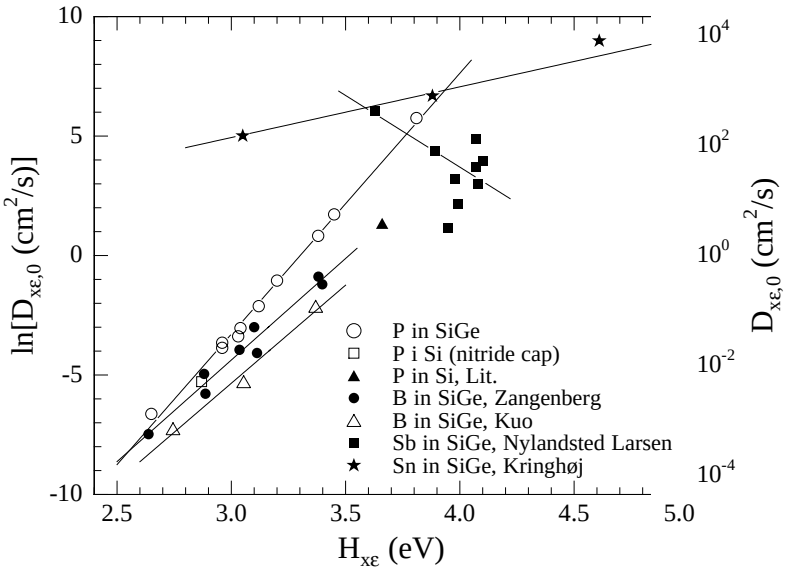

Figure 8.7: Relation between the prefactor and the activation enthalpy of diffusion for various diffusers in strained and relaxed Si and SiGe. The literature value for P diffusion in Si is from Fair [34], and the other data points are from Zangenberg *et al.* [V], Kuo *et al.* [125], Nylandsted Larsen and Kringhøj [43], and Kringhøj and Elliman [42].

Summary

In conclusion, we have studied the diffusion of P and B in Si and $Si_{1-x}Ge_x$ as a function of Ge content and biaxial strain. We observed that the diffusion of B is retarded with increasing x in relaxed $Si_{1-x}Ge_x$, whereas the diffusion of P is not. This can be taken as an indication that B immobilizes due to pairing with Ge atoms. Both for P and B, the strain and the composition are observed to have large effects upon the prefactor $D_{x\epsilon,0}$ and the activation enthalpy $H_{x\epsilon}$ of diffusion. However, in contrast to vacancy-mediated diffusers, $D_{x\epsilon,0}$ and $H_{x\epsilon}$ for P and B are strongly coupled to each other via the Meyer-Neldel Compensation Rule.

Chapter 9

Deep levels in semiconductors: Concepts and experimental issues

An outline is given of the most basic theoretical aspects concerning deep levels, as well as experimental aspects of transient techniques that are used to characterize deep levels. Very good treatments of carrier exchange between deep levels and energy bands are given by Bourgoin and Lannoo [141] and by Blood and Orton [142]. Both sets of authors also provide a discussion on transient methods; in particular, the one by Blood and Orton [142] is very thorough.

9.1 Carrier capture and emission

Impurities, intrinsic defects, and complexes thereof break the periodicity in the lattice and may, as a result, bind electrons or holes in localized, deep levels, or 'centers', within the band gap of the semiconductor. For example, consider single and double acceptor levels of an electron trap X. The energy levels $E_t^{-/=}$ and $E_t^{0/-}$ are defined in terms of the free energies of single and double ionization of the trap, since these are given by

$$\Delta G^{0/-} = E_c - E_t^{0/-} \quad \text{and} \quad \Delta G^{-/=} = E_c - E_t^{-/=}, \tag{9.1}$$

respectively. That is, $E_c - E_t^{0/-}$ and $E_c - E_t^{-/=}$ are the free-energy differences in the reactions

$$X^{=} \xrightarrow[E_c - E_t^{-/=}]{} X^{-} + e^{-} \xrightarrow[E_c - E_t^{0/-}]{} X^{0} + 2e^{-} \tag{9.2}$$

between {the center X^i} and {the center X^{i-1} plus an extra electron in the conduction band}; $i = 1, 2$.

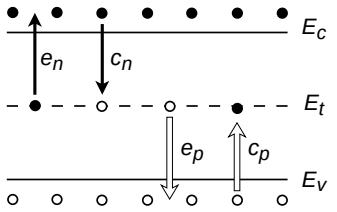

Figure 9.1: Electron and hole exchange processes for a deep center with energy level E_t.

In general, a deep center in the band gap will communicate with either the conduction band or the valence band, or in some cases with both, by exchanging electrons and holes by either of the four processes of Fig. 9.1. In this figure, e_n and e_p are the rates of electron and hole emission (carriers s^{-1} $trap^{-1}$), and c_n and c_p are the rates of electron and hole capture (carriers s^{-1} $trap^{-1}$).

For any transition, the emission and capture rates of each carrier type (electron or hole) are governed by detailed balancing. At the same time, the thermal-equilibrium occupancy of a trap is given by Fermi-Dirac statistics, and as a result, one finds [142] for electron emission (hole emission is similar):

$$e_n = \underset{\uparrow}{c_n} \quad \frac{g_{i-1}}{g_i} \exp\left(\frac{E_t - E_F}{kT}\right) \tag{9.3}$$

$$\sigma_n \langle v_n \rangle_{th} n$$

$$= \sigma_n \gamma_n T^2 \frac{g_{i-1}}{g_i} \exp\left(-\frac{E_c - E_t}{kT}\right), \tag{9.4}$$

where $\gamma_n = 2\sqrt{3}(2\pi)^{3/2} k^2 m_n^* h^{-3}$, m_n^* being the effective electron mass, $\langle v_n \rangle_{th}$ is the mean thermal velocity of the electron, g_{i-1} and g_i are the numbers of different trap configurations when it contains i or $i-1$ electrons, and σ_n is the carrier capture cross section. The latter often has a small temperature dependence [143] that can be put on the form:

$$\sigma_n(T) = \sigma_\infty \exp\left(\frac{E_\sigma}{kT}\right). \tag{9.5}$$

With transient techniques (Sec. 9.2.1), $e_n(T)$ can be measured for a given center. Inserting (9.5) into (9.4) and using $\Delta G = \Delta H - T\Delta S$, it follows that from a plot of $\ln(e_n/T^2)$ vs. $1/T$ (e.g., Fig. 10.5 on p. 108) one can extract these quantities:

$$E_{na} \equiv \Delta H + E_\sigma, \tag{9.6}$$

$$\sigma_{na} \equiv \sigma_\infty \frac{g_{i-1}}{g_i} \exp(\Delta S/k). \tag{9.7}$$

They are the *apparent activation enthalpy* E_{na} and the *apparent cross section* σ_{na} (extrapolated to $T = \infty$). Together they define the *electronic signature* that is associated with a particular transition (i.e., level) in the gap.

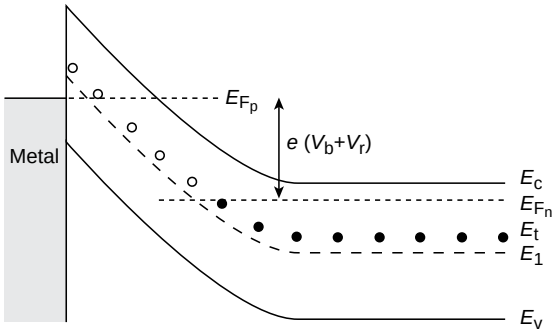

Figure 9.2: A Schottky junction on an n-type semiconductor in thermodynamic equilibrium, containing a trap with $E_t > E_1$. V_b is the built-in voltage and V_r is the applied, reverse voltage. The regions of empty (○) and filled (●) traps are indicated. The quasi Fermi level for holes, pinned to the Fermi level of the metal, has been drawn according to Rhoderick [144].

The particular nature of a deep level is determined by whichever two processes will be the most favourable ones if the defect is to change back and forth between the two charge states that define the level. A level is said to act as either of the four:

Electron trap:	$e_n \gg c_p, c_n \gg e_p$,
Hole trap:	$e_n \ll c_p, c_n \ll e_p$,
Recombination center:	$e_n \ll c_p, c_n \gg e_p$,
Generation center:	$e_n \gg c_p, c_n \ll e_p$.

Whether e_n dominates over c_p and whether c_n dominates over e_p is determined by the trap position relative to the quasi Fermi levels for electrons and holes, E_{F_n} and E_{F_p} (defined in their usual way [141]) and the capture ratio c_n/c_p. The following equivalences namely hold [141]:

$$e_n \gg c_p \Leftrightarrow \frac{E_t + E_{F_p}}{2} > E_1, \tag{9.8}$$

$$c_n \gg e_p \Leftrightarrow \frac{E_t + E_{F_n}}{2} > E_1, \tag{9.9}$$

where

$$E_1 \equiv E_i + \frac{kT}{2} \ln\left(\frac{\sigma_p \langle v_p \rangle_{th}}{\sigma_n \langle v_n \rangle_{th}}\right). \tag{9.10}$$

E_1 will usually be slightly above the middle of the band gap for acceptor levels [e.g., (0/−)] and slightly below for donor levels [e.g., (+/0)]. A Schottky junction on an n-type semiconductor is depicted in Fig. 9.2. In thermodynamic equilibrium, the trap in the figure (assume $E_t > E_1$) will be an electron trap at the crossing point with E_{F_n}, and the trap is filled with electrons only when below E_{F_n}. For the reverse situation, $E_t < E_1$, one would find that the filling is determined by E_{F_p}; if a crossing point exists, the trap will acts as a hole trap

near that point. Refer to Ref. [141] for details on the relative populations as a function of $E_t - E_F$.

9.2 Experimental issues

9.2.1 Transient spectroscopies

Methods such as deep-level transient spectroscopy (DLTS), devised by Lang [145], and minority-carrier transient spectroscopy (MCTS) provide a means to quantify carrier capture and emission rates and the accompanying enthalpy and entropy changes. Ionization free energies can also be found by Hall measurements, but this technique is limited to centers that are present in high enough concentrations to cause and dominate temperature-dependent changes in the carrier concentration. Calculations of defect levels have been demonstrated for Si [146] but have so far not been attempted for Ge – partly on account of the large uncertainty of the calculated levels (about ± 0.15 eV) relative to the band gap.

Microscopic information about the defects is not directly obtained in DLTS and MCTS, thus, defect identification is often performed indirectly, by varying impurity concentrations and studying annealing kinetics, and comparing these observations, if possible, with results from, e.g, electron-paramagnetic resonance (EPR), fourier-transform infrared spectroscopy (FTIR), or Mössbauer spectroscopy. These are techniques that can provide information about the chemical surroundings and the symmetry of a defect. Laplace-transform DLTS has been developed very recently. It offers superior resolution, splitting conventional DLTS lines according to the atomic surroundings of a defect [147], but it is primarily applied to lines that are already well-characterized by conventional DLTS.

In *transient spectroscopies*, defects within some region of the semiconductor are first brought to capture carriers, and subsequently they are brought to emit carriers, during which period a signal is measured. A rectifying junction is usually employed, which is kept on a constant reverse bias V_r during measurement (see Fig. 9.2). In majority- and minority-carrier DLTS, the capture ('filling') is brought about by shortly (typically 10–100 μs) pulsing to a lower reverse bias or a forward bias, respectively. With MCTS, the capture is brought about by photoexcitation of electron–hole pairs with above-band gap light, usually from a diode laser. Under ideal circumstances, only minority carriers enter the active region during the photopulse; in Si this is normally achieved with front-side illumination through a semitransparent barrier: A large number of electron–hole pairs are generated on the deep side of the space-charge region, but due to the electric field, only diffusing minority carriers are allowed to enter this region. For Ge, carrier generation on the deep side of the

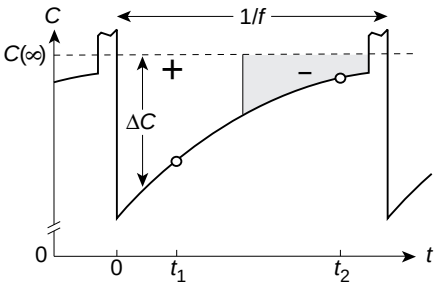

Figure 9.3: Schematic of the construction of a DLTS signal S, illustrated for majority-carrier emission (for minority-carrier emission, the sign of ΔC is changed). With the *lock-in amplifier* method, S is formed by integrating $\Delta C(t)$ weighted with a square-wave signal such that the '–' area is subtracted from the '+' area. With the *double-box car* method, ΔC is sampled at two temporal points t_1 and t_2, and $S \propto \Delta C(t_1) - \Delta C(t_2)$. For simplicity, instrument recovery and gate-off times [142] have been neglected.

space-charge region can not be obtained with front-side illumination since the penetration depth of light at the normal wavelengths employed is small (see Chap. 10 and also pp. 134–136).

When the number of charges bound to defects changes, so does the diode capacitance C. E.g., during thermal emission of electrons, $\Delta C(t) \propto \exp(-e_n/t)$, where $e_n = e_n(T)$ is given by Eq. (9.4). The DLTS signal S, illustrated in Fig. 9.3, is devised from the $\Delta C(t)$ signal in such a way that S peaks at a particular emission rate e_n' that is set by the choice of experimental parameters. The temperature at which one obtains $e_n(T) = e_n'$ is denoted T'; by performing a *temperature scan* of the diode, T' is found as the point where $S(T)$ peaks. For a lock-in amplifier setup,

$$e_n' \equiv e_n(T') = 2.167 f, \tag{9.11}$$

where $1/f$ is (approximately) the interval over which $\Delta C(t)$ is integrated. And for a double-box car system,

$$e_n' \equiv e_n(T') = \frac{\ln(t_1/t_2)}{t_1 - t_2}, \tag{9.12}$$

where t_1, t_2 are the two temporal points where $\Delta C(t)$ is sampled. e_n' is called the *rate window*.

Different (e_n',T') pairs (see Fig. 10.5 on p. 108) can be found by performing temperature scans with different rate windows, typically in the interval $e_n = 1$–$1000\ \mathrm{s}^{-1}$. The trap concentration relative to the doping level, $N_t/|N_D - N_A|$, can be calculated from the apparatus sensitivity and the peak height of the signal, $S(T')$. The detection limit is usually at $N_t/|N_D - N_A| \sim 10^{-4}$–$10^{-3}$.

Alternative modes of operation include *frequency scan*: f is varied at fixed $T = T'$; and *depth profiling*: The reverse bias is maintained at V_r and the difference is recorded between two DLTS signals that were obtained after pulsing

to two different, reverse biases V_1 and V_2. The signal is recorded as these biases are slowly varied between 0 and V_r with fixed resolution $\Delta V = V_1 - V_2$; ideally $\Delta V \ll V_r$.

As is easily understood, a lock-in amplifier setup has the advantage of a greater signal-to noise ratio, the double-box car technique allows for simultaneous monitoring of more than one rate windows during each temperature scan. The relative width of the lineshape $S(T)$ is slightly smaller for a double-box car system.

9.2.2 Instrumentation

Most DLTS measurements were carried out at the University of Aarhus. Either of two commercial setups were used: a DLS-82E or a DLS-83D, both manufactured by Semilab, Budapest. Fully identical spectra were obtained from the two systems. Each setup contains a pulse generator and an automatic frequency sweeper, a reverse-bias power supply, a capacitance and conductance meter, an automated capacitance compensator, a temperature controller and a cryostat, a lock-in amplification system, as well as output signal monitors (oscilloscope, counter, multimeter) and computerized data acquisition through an IEEE card. The cryostats employed in the present experiments have a built-in resistive heater (max. temperature 175 °C) and they are cooled by immersion into a liquid-N_2 bath.

The DLS-83D excels in ease of operation since all of the above components (except oscilloscope and, of course, cryostat) are built into a single, compact desktop unit with fully PC-integrated readout and control of all settings. On the DLS-82E, a few of the components are built together.

For MCTS (and supplementary DLTS) measurements, a commercial Polaron setup from Biorad was used at the PHASE[36] laboratory of CNRS,[37] Strasbourg. The setup is somewhat similar to the DLS-83D, except that it utilizes the double-box car method with simultaneous recording of two rate windows. The cryostat here uses circulation of liquid-N_2, and it is evacuated with a roughing pump. The GaAs diode laser is affixed directly onto the cryostat.

[36] PHysique et Applications des SEmi-conducteurs
[37] Centre National de la Recherche Scientifique

Chapter 10

Article: Irradiation-induced defects in Ge studied by transient methods.

J. Fage-Pedersen, A. Mesli, and A. Nylandsted Larsen, Phys. Rev. B **62**, *10116 (2000).* [IV]

Abstract

Irradiation-induced impurity-point defect complexes have been investigated in *n*-type germanium crystals that were doped with either antimony or oxygen. Several majority and one minority carrier traps are characterized by means of Deep Level Transient Spectroscopy (DLTS) and Minority Carrier Transient Spectroscopy (MCTS). The antimony-vacancy complex (*E* center) $E_{0.37}$ is found to anneal in a way that is fundamentally different from that in silicon, since it is retarded under reverse bias. Temperature-dependent carrier capture cross sections of the *E* center are an order of magnitude lower than those of the oxygen–vacancy complex (*A* center) $E_{0.27}$ ($\sigma_n \sim 1.5 \times 10^{-18}$ cm^2 and 2×10^{-17} cm^2, respectively). A trap $E_{0.23}$ which is antimony-related grows in at room temperature, seemingly by interstitial capture. A trap $E_{0.29}$ is assigned to the divacancy since it is observed after proton irradiation but not after electron irradiation. A minority carrier trap $H_{0.30}$, displaying strong Poole-Frenkel effect, is Sb-related and possibly related to the *E* center. In view of the experiments, we comment on a range of diverging results in the literature.

10.1 Introduction

For the last couple of decades the dedication to understand point defect- and impurity-point defect interactions in Ge has been at a large deficit relative to that in Si. This unfortunate circumstance is naturally related to the overwhelming success of Si in applied fields; Ge has not been used extensively in devices

but primarily in high-purity form as detector material. A recent trend, however, is that of venturing from Si into $Si_{1-x}Ge_x$ [148]. This trend originates in improved epitaxial growth techniques and the promise of very fast devices [4]. Needless to say, a satisfactory description of carrier, defect, and band gap issues calls for good understanding in the full composition range $0 \leq x \leq 1$. At the same time it is a misfortune that Ge, so similar to Si, has not been used to its full potential as a test ground for a range of fundamental defect properties.

Investigations of irradiated *n*-type Ge have employed electronic techniques such as Hall measurements [149] or deep-level transient spectroscopy (DLTS) [150, 151, 152, 153, 154]. Electron paramagnetic resonance unfortunately has only limited applicability in Ge, but infrared (IR) absorption spectroscopy has been applied to O-doped Ge [155, 156]. From DLTS investigations in the literature one sees, however, that considerable scatter exists in reported energy levels, defect annealing behaviour and microscopic interpretation of those defects that dominate after sample irradiation.

In this article we show that the reverse-bias annealing of the Sb *E* center in Ge is fundamentally different from that in Si. Different annealing mechanisms are considered, as is the likelihood of a double-negative *E* center charge state. It turns out that several defects evolve strongly at room temperature. By comparing electron with proton irradiation, we are able to manifest the level of the divacancy. And we make an attempt of clarifying and unifying, where possible, experimental results from the literature.

10.2 Experimental Details

Three types of material were employed, they will be denoted *Sb1*, *Sb2*, and *Ox*. Czochralski-Ge *Sb1* and *Sb2* from Union Miniere, Belgium, contain respectively 3.5×10^{14} cm^{-3} Sb and 1.4×10^{15} cm^{-3} Sb, and *Ox* contains, from growth, a concentration of interstitial O of 7×10^{16} cm^{-3} (measured with infrared absorption). O-doped Ge is known to acquire its *n*-type nature from thermal, oxygen-related donors [157]; for *Ox* we measured carrier concentrations between 4 and 8×10^{14} cm^{-3}, depending on the sample.

Schottky barriers were fabricated by electron-gun evaporation of either Au, Pd, or Pt, or by thermal evaporation of Au. Immediately before diode evaporation, crystals were dipped in HF. Some *Ox* samples had been etched with CP4 with no apparent effect on the spectra. At room temperature (RT) typical leakage currents at -10 V were ~ 4 mA/cm^2 on *Sb2* material and a bit less on *Sb1*. C-V characteristics were ideal. On *Ox* Ge the diode quality was less reproducible, with RT leakage currents often a factor of 2-3 higher. A few of these diodes required slight cooling ($\sim$ 30-50 K) below RT to display ideal C-V characteristics.

Defects were introduced by irradiating the diodes at RT with either 2 MeV

electrons or 2 MeV protons. Beam intensities were typically $\sim$ 100 nA cm^{-2} for electrons and $\sim$ 0.5 nA cm^{-2} for protons, and it was ascertained that the beam induced no sample heating.

Electron traps were characterized with DLTS in a lock-in amplifier setup. Hole traps were studied in a double-box car system with either injection-pulse (i.e. forward bias pulse) DLTS or with minority carrier transient spectroscopy (MCTS). MCTS enables one to probe minority carrier traps by excitation of electron-hole pairs with the use of above-band gap light. For this purpose a GaAs diode laser was applied to the front of semitransparent Schottky barriers (typical metal thickness $\sim$ 100 Å). In Ge the penetration depth ($1/e$) at the appropriate wavelength of 870 nm is approximately 0.5 μm, which is considerably less than in Si, e.g. Therefore one must be aware that MCTS probes a region that is very close to the interface.

Temperature scans with DLTS and injection-pulse DLTS showed that all unirradiated materials were defect free when prepared with thermally evaporated diodes. When prepared with electron-gun diodes, a hole trap ($H_{0.30}$) was detected in unirradiated *Sb1* and *Sb2*.

10.3 Experimental Results: Overview

The individual electron trap is defined by its electronic signature, i.e. $\log\left[e_n(T)/T^2\right]$ vs. $1/T$, where $e_n(T)$ is the electron emission rate per trap. With the usual symbol meanings [158] the signature of an electron trap is determined by the apparent capture cross section at $T = \infty$,

$$\sigma_{\mathrm{na}} = \sigma_\infty \frac{g_0}{g_1} e^{\Delta S/k} \tag{10.1}$$

and the apparent enthalpy (according to which trap labels are chosen in this paper)

$$E_{\mathrm{na}} = \Delta H + E_\sigma. \tag{10.2}$$

Here we assumed a thermally activated cross section for carrier capture,

$$\sigma_n(T) = \sigma_\infty e^{-E_\sigma/kT}, \tag{10.3}$$

and the trap energy level E_t is defined by

$$E_c - E_t = \Delta G = \Delta H - T\Delta S. \tag{10.4}$$

Similar expressions apply for hole traps.

Before discussing the individual traps, an overview is presented of the occurrences of traps and their annealing behavior. Of main concern will be the

Table 10.1: Properties of all electron and hole traps presently observed.

Label	E_{na} (eV)	σ_{na} (cm^2)	Annealing (°C) [a]	Identification	Occurrence	
$H_{0.30}$	0.30 [b]	1.6×10^{-13} [b]	↑ 150	Sb-related	*Sb1*, *Sb2*	H, e
$E_{0.37}$	0.37	1.1×10^{-14}	↓ 150	*E* center	*Sb1*, *Sb2*	H, e
$E_{0.23}$	0.23	2.0×10^{-15}	↑ RT, ↓ 110	Sb- and *I*-related	*Sb1*, *Sb2*	H, e
$E_{0.19}$	0.19	1.5×10^{-14}	↑ RT, ↓ RT	Sb- and *I*-related	*Sb1*, *Sb2*	H, e
$E_{0.13}$	0.13	3.2×10^{-15}	↑ RT, ↓ RT	Sb- and *I*-related	*Sb1*, *Sb2*	H, e
$E_{0.21}$	0.21	7.1×10^{-14}	↑ 90, ↓ 180	Sb-related?	*Sb1*, *Sb2*	H, e
$E_{0.29}$	0.29	2.1×10^{-15}	↓ 180	Divacancy	*Sb1*, *Sb2* (, *Ox*?)	H
$E_{0.30}$	0.30	2.9×10^{-14}	↑ RT, ↓ 110	*I*- and impurity-related?	*Sb2*	H, e
$E_{0.28}$	0.28	6.2×10^{-15}	↑ 190, ↓ 270	O-impurity complex?	*Sb1*	H, e
$E_{0.27}$	0.27	2.6×10^{-15}	↓ 150	*A* center	*Sb1*, *Ox*	H, e
$E'_{0.19}$	0.19	2.2×10^{-15}	↑ 130, ↓ 190	O-related	*Ox*	H, e
$E_{0.14}$	0.14	1.3×10^{-16}	↑ 130, ↓ 190	O-related	*Ox*	H, e

[a] After 2 MeV proton irradiation
[b] E_{pa} and σ_{pa} at -1 V bias

E center $E_{0.37}$, the *A* center $E_{0.27}$, as well as the level $E_{0.29}$ that we propose to be related to the divacancy, and $H_{0.30}$ and $E_{0.23}$ that we propose to both be Sb-related, the latter in connection with an interstitial Ge atom *I*. Properties of the observed traps are summarised in Tab. 10.1.

Fig. 10.1 shows DLTS temperature scans from materials *Sb1* and *Sb2*, recorded three days after 2 MeV electron irradiations. The following traps were present in both materials: $E_{0.37}$, $E_{0.23}$, $E_{0.19}$, $E_{0.13}$, and, after a $\sim$ 100 °C anneal, $E_{0.21}$. $E_{0.27}$ occurred only in *Sb1*, as did also a trap $E_{0.28}$ which grew up after a 190 °C anneal. A trap $E_{0.30}$ occurred only in *Sb2*. Irradiating *Sb1* and *Sb2* materials with 2 MeV protons resulted in almost identical spectra, except for the pronounced occurrence of $E_{0.29}$ of which merely a hint was seen upon electron irradiation. This trap, partly hidden beneath others, becomes particularly visible upon annealing, as is seen in Fig. 10.2 where spectra are shown of 110 °C-annealed *Sb2* samples that had been either electron- or proton-irradiated.

When applying MCTS or injection-pulse DLTS to *Sb1* or *Sb2*, the hole trap $H_{0.30}$ is predominant after both electron and proton irradiation. This is shown in Fig 10.3 for *Sb2* material.

A DLTS scan from a proton-irradiated *Ox* sample is presented in Fig. 10.4. $E_{0.27}$ strongly dominates the spectrum, and two new traps, $E_{0.14}$ and $E'_{0.19}$, are found.

The inset of Fig. 10.4 shows a DLTS scan from the *Ox* material recorded with injection pulse. Three hole traps are present, and none of them is $H_{0.30}$. Presumably, reports of the *Ox* hole traps have not been made in the literature, but in this study focus will be solely on $H_{0.30}$.

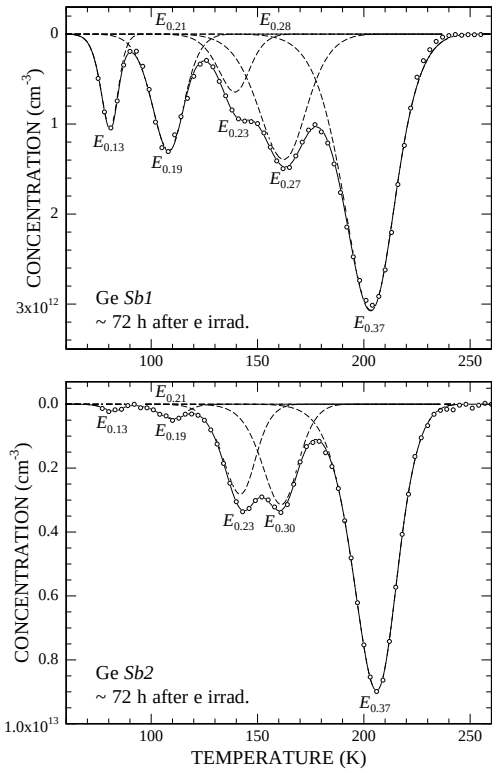

Figure 10.1: DLTS spectra from *Sb1* and *Sb2*, recorded 3 days after 4×10^{13} cm^{-2} electron irradiations (we have also indicated where $E_{0.21}$ and $E_{0.28}$ grow in *after* annealing). For clarity only every 3rd data point has been drawn here and in all other plots. The solid-curve fit is a sum of the dashed curves. Settings were $e_n = 542$ s^{-1}, bias $-10 \rightarrow -5$ V, pulse duration 100 μs.

Electronic signatures of electron traps are displayed in Fig. 10.5. Electric--field (Poole-Frenkel) effects were not exhibited by any of the electron traps that occurred at room temperature in Sb-doped Ge, and we infer that the electron traps probably have acceptor character.

The hole trap $H_{0.30}$, on the other hand, exhibits clear Poole-Frenkel effect: The $H_{0.30}$ signatures in Fig. 10.6 were obtained under reverse biases of 1 V, 8 V, and 20 V respectively, and they demonstrate that for $H_{0.30}$ hole emission is strongly enhanced with increased electric field. Thus, $H_{0.30}$ is believed to create an acceptor level.

We find that dramatic evolution of defect concentrations takes place already at RT in Sb-doped Ge. As a consequence, details of the defect dynamics that would normally be lost if proceeding upon irradiation with a standard annealing series, may be revealed by monitoring defect concentrations first as a function of storage time at RT, and subsequently as a function of annealing temperature. Results of such a study, on proton-irradiated *Sb1* and *Sb2*, are plotted

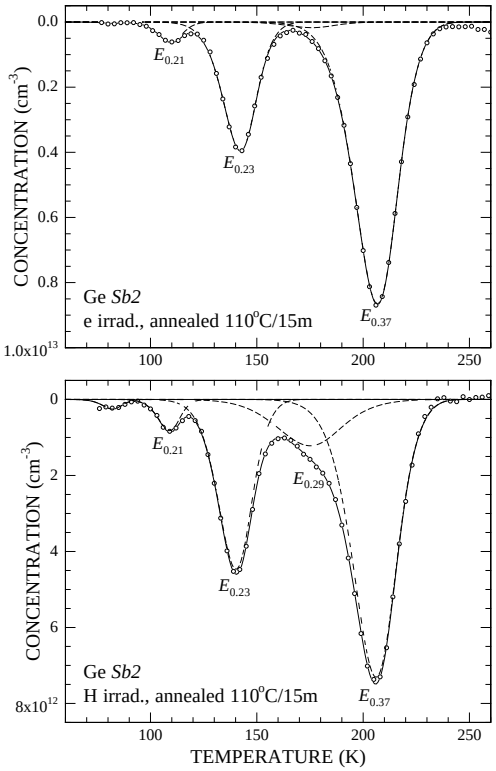

Figure 10.2: DLTS spectra from *Sb2,* irradiated with 2×10^{13} cm^{-2} electrons (upper panel) or 1.7×10^{11} cm^{-2} protons (lower panel) and annealed at 110 °C for 15 min. The $E_{0.29}$ defect is seen clearly only after proton irradiation. Settings as in Fig. 10.1.

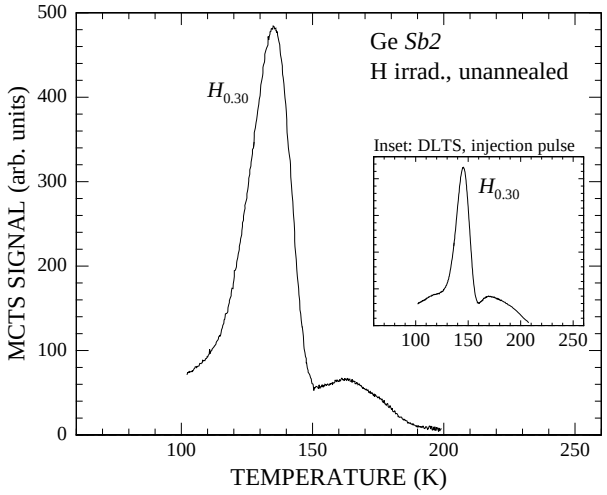

Figure 10.3: Double-box car MCTS spectrum from a thermal Au diode on *Sb2* material, irradiated with 5×10^{11} cm^{-2} protons. Settings were $e_n = 50$ s^{-1}, bias -2 V. Inset: Double-box car DLTS spectrum with the use of an injection pulse. Settings were $e_n = 80$ s^{-1}, bias $-2 \rightarrow +2$ V.

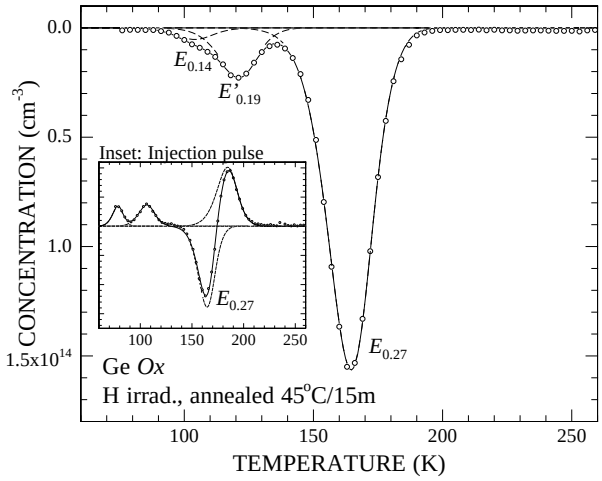

Figure 10.4: DLTS spectrum from an *Ox* sample, irradiated with 6×10^{10} cm^{-2} protons and annealed at 45 °C for 15 min. Settings as in Fig. 10.1. Inset: DLTS spectrum from an *Ox* sample under injection pulse. $H_{0.30}$ is not present in the O-doped material.

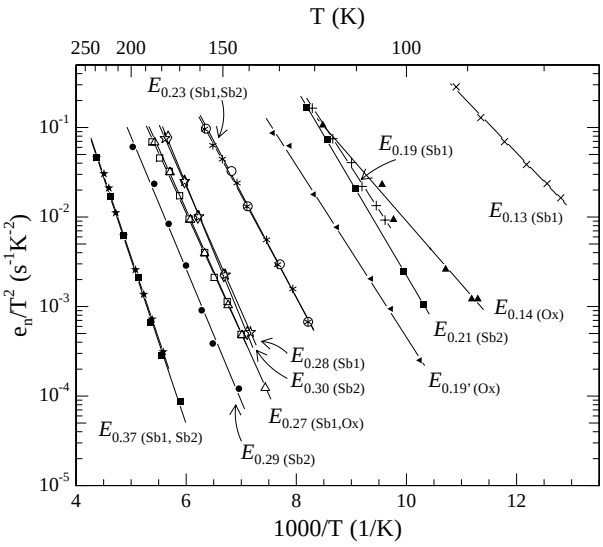

Figure 10.5: Electronic signatures of all observed electron traps. For some of those traps that are present in more than one material the signatures from both materials are presented; this is indicated in parentheses.

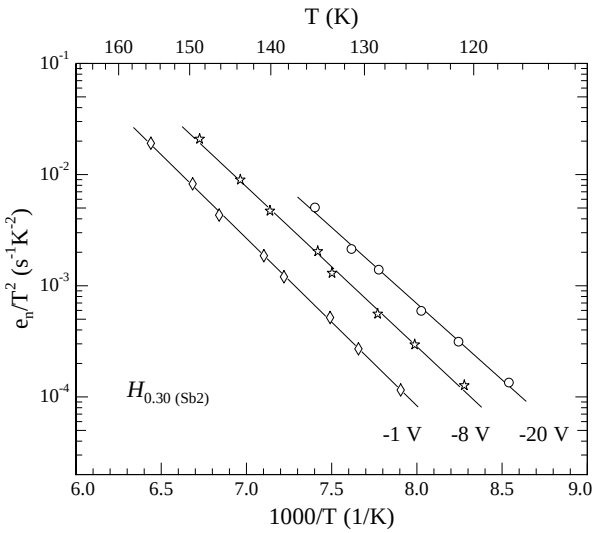

Figure 10.6: Electronic signature of the $H_{0.30}$ hole trap in Sb2 material, extracted from MCTS spectra at reverse biases of 1, 8, and 20 V, respectively.

in Fig. 10.7. Apart from slight quantitative differences, the defects that occur in both materials, viz. $E_{0.37}$, $E_{0.29}$, $E_{0.23}$, $E_{0.21}$ $E_{0.19}$, and $E_{0.13}$, indeed have the same annealing behaviour in both materials.

The annealing series for proton-irradiated, O-doped Ge is plotted in Fig. 10.8, and the observed annealing behaviour of $H_{0.30}$ in *Sb2* is reported in Fig. 10.9. It turns out that this is not independent of the method of observation (injection-pulse DLTS or MCTS).

The annealing behaviour of the individual defects shall be discussed in Sec. 10.4 below.

10.4 Experimental Results: Analysis and Discussion

In the following, for the sake of clarity, designated names of defects that are reported in the literature will be additionally indexed with author name. In accordance with the discussion below, an overview is given in Tab. 10.2 of some of these defects. Unless otherwise stated, defect energy levels are referred to in terms of the apparent ionisation enthalpies (Eq. 10.2).

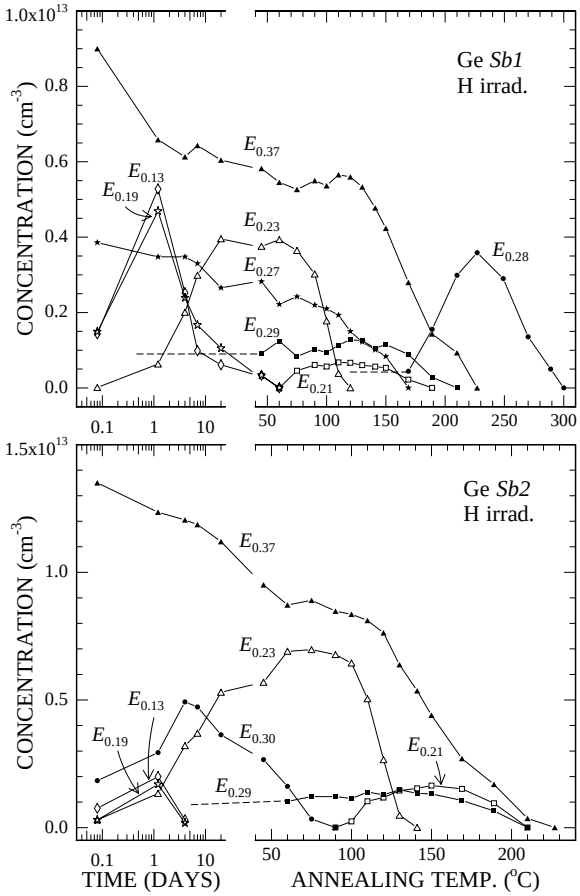

Figure 10.7: Annealing series of proton-irradiated materials *Sb1* and *Sb2*. After irradiation the defect concentrations were followed first as a function of time at RT, and subsequently as a function of 15 min isochronal anneals. The initial concentrations of $E_{0.29}$ and $E_{0.28}$ are somewhat uncertain, since the peaks are overlapped with those of $E_{0.30}$ or $E_{0.27}$.

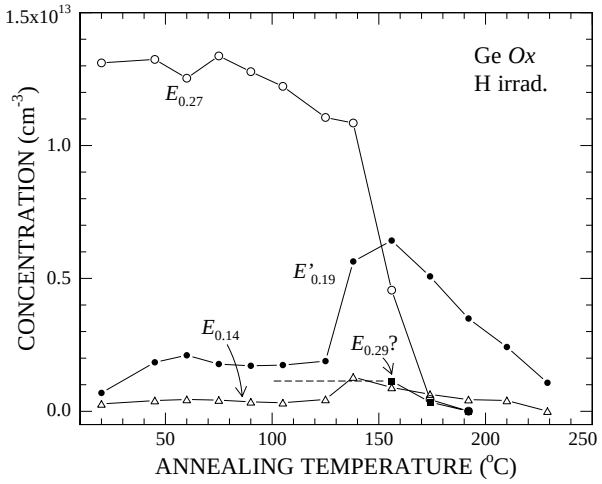

Figure 10.8: 15 min isochronal annealing series of proton-irradiated material *Ox*. Due to overlap with $E_{0.27}$ it cannot be decided after anneals below 156 °C whether $E_{0.29}$ exists.

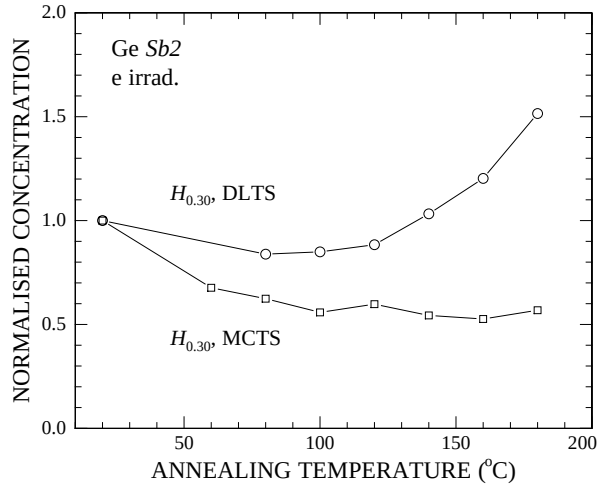

Figure 10.9: 10 min isochronal annealing series of $H_{0.30}$ in material *Sb2*. The DLTS measurements were performed with an injection bias (-4 V→+2 V), and the MCTS measurements were performed at a reverse bias of 2 V. It was ascertained in all MCTS measurements that the same photo current was generated in the diode.

Table 10.2: Connection between selected deep traps from the literature. The Ge was doped with either of the indicated elements and irradiated with either of the indicated species. Each entry contains designated name, apparent enthalpy (eV), apparent cross section (cm^2) at $T = \infty$, and annealing behaviour (°C).

	This study Sb, O H, e	Bourgoin *et al.* [150,159,160] Sb, 'group V' e	Fukuoka *et al.* [161,151,152] Sb, O e	Marie *et al.* [154] Sb Pb, Ne	Nagesh *et al.* [153] Sb, O, P n, γ	Zistl [162] Sb e
Sb-related	$H_{0.30}$ 0.30 1.6×10^{-13} $\uparrow$ 150	H_2 0.30 - $\uparrow$ 150, $\downarrow$ 250	$H(0.24)$ 0.24 - $\uparrow$ 110 (hours)			
E center	$E_{0.37}$ 0.37 1.1×10^{-14} $\downarrow$ 150	E_2 0.53 4×10^{-11} $\downarrow$ 150	$E(0.40)$ 0.40 - $\downarrow$ 97 (hours)	$ET5$ 0.46-0.47 0.4-1.1$\times 10^{-12}$ $\downarrow$ 150	E_4 0.35 - $\downarrow$ 125	$ET5$ 0.34-0.39 - $\downarrow$ 150
Divacancy	$E_{0.29}$ 0.29 2.1×10^{-15} $\downarrow$ 180	E_4, E_5 0.46, 0.42 3×10^{-12}, 2×10^{-12} $\uparrow$ 90[a], $\downarrow$ 150		$ET4$ 0.32 1.3×10^{-14} $\downarrow$ 140		
A center	$E_{0.27}$ 0.27 2.6×10^{-15} $\downarrow$ 150		$E(0.25)$ 0.25 - $\downarrow$ 140		E_3 0.27 - $\downarrow$ 90	
Sb- and I-related	$E_{0.23}$ 0.23 2.0×10^{-15} $\uparrow$ RT, $\downarrow$ 110	E_1 0.32 1×10^{-13} $\downarrow$ 110	$E(0.23)$ 0.23 - $\uparrow$ 70 $\downarrow$ 110	$ET3$ 0.29 2.2×10^{-14} $\downarrow$ 90	E_2[b] (?) 0.17 - $\uparrow$ RT, $\downarrow$ 100	ET3 0.22-0.23 - $\uparrow$ RT, $\downarrow$ 110
Sb-related?	$E_{0.21}$ 0.21 7.1×10^{-14} $\uparrow$ 90, $\downarrow$ 180			$ET2$ 0.27-0.28 2.0-8.2$\times 10^{-12}$ $\uparrow$ 80, $\downarrow$ 160	E_6 (?) 0.15 - $\uparrow$ 80, $\downarrow$ 170	
O-related	$E'_{0.19}$ 0.19 2.2×10^{-15} $\uparrow$ 130, $\downarrow$ 190		$E(0.13)$ 0.13 - $\uparrow$ 120, $\downarrow$ 200		E_5 0.17 - $\downarrow$ 225	

[a] Increased by 70 % after 2 MeV e irrad., not after 1 MeV e irrad.

[b] Observed after n irrad., not after γ irrad.

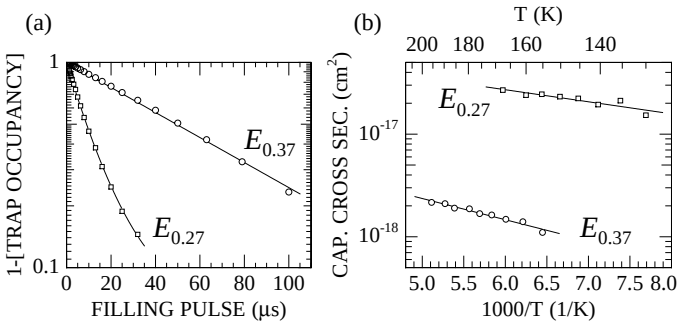

Figure 10.10: (a) Fraction of empty trap vs. filling time for the A center $E_{0.27}$ at $T =$ 141 K, e_n=10 s^{-1} and the E center $E_{0.37}$ at $T =$ 186 K, e_n=50 s^{-1}. For the A center the filling has a slight Debye free carrier incursion effect, and the fit has been done with the Simplex method using the complete DLTS signal: formula (8) in Ref. [7]. (b) The thermal activation of the extracted electron capture cross sections.

10.4.1 Level $E_{0.27}$

$E_{0.27}$ strongly dominates after irradiation of O-doped Ge (*Ox*) and it is present also in *Sb1*. $E_{0.27}$ anneals abruptly at 150 °C in the *Ox* material, but the annealing starts at a lower temperature in *Sb1*. $E_{0.27}$ is identical to $E(0.25)_{\mathrm{Fuk}}$ (at $E_c - 0.25$ eV, anneals at $T_{\mathrm{ann}} \sim 150$ °C) reported by Fukuoka and Saito [152] and to $E_{3,\mathrm{Nag}}$ (0.27 eV, $T_{\mathrm{ann}} \sim 90$ °C) reported by Nagesh and Farmer [153]. These levels were found to dominate in irradiated O-doped Ge and they were indeed assigned to the *A center*.

The electron capture cross section was measured by varying the filling pulse duration at different, fixed temperatures. This is demonstrated in Fig. 10.10. We obtain

$$\begin{aligned} \sigma_n^{E_{0.27}}(T) &= 1.37 \times 10^{-16} \exp\left(-\frac{0.023\ \mathrm{eV}}{kT}\right)\ \mathrm{cm}^2 \\ &\approx (1.8 - 2.9) \times 10^{-17}\ \mathrm{cm}^2 \end{aligned} \tag{10.5}$$

in the 130–170 K range. The value of the capture cross section is discussed below in connection with that of $E_{0.37}$.

10.4.2 Level $E_{0.37}$

$E_{0.37}$ is present in both kinds of Sb-doped Ge. The introduction rate increases with Sb concentration, but the level is absent in oxygen-doped Ge. In highly

Sb-doped Ge (*Sb2*) $E_{0.37}$ is in fact the sole observed defect very shortly after electron irradiation; all other defects in *Sb2* are secondary defects that grow in with time.

Sb is expected to bind vacancies in Ge, and our data confirm the conclusion by Nagesh and Farmer [153] that the corresponding level $E_{4,\mathrm{Nag}}$ (at $E_c - 0.35$ eV, seen in both P and Sb-doped Ge after neutron and after γ irradiation, $T_{\mathrm{ann}} \sim 125$ °C) is the *E center*. Moreover, $E_{0.37}$ is identical to the level $E(0.40)_{\mathrm{Fuk}}$ observed by Fukuoka and Saito [161,151]. Fukuoka and Saito did not conclude that $E(0.40)_{\mathrm{Fuk}}$ was the E center, but $E(0.40)_{\mathrm{Fuk}}$ dominated the spectra in two kinds of 1.5 MeV e-irradiated, Sb-doped Ge, and it annealed over several hours at 97 °C.

Let us briefly point out that in two kinds of *As*-doped material the level $E(0.40)_{\mathrm{Fuk}}$ was replaced by $E(0.27)_{\mathrm{Fuk}}$ [151]. Thus, it is evident that $E(0.27)_{\mathrm{Fuk}}$ is the As E center, but it is interesting that the enthalpy differs markedly from those of the Sb and P E centers.

A fraction of $E_{0.37}$ disappears already at RT, but the major fraction anneals at $\sim$ 150 °C. Thermally activated dissociation or diffusion would not proceed over such a wide temperature span. Hence, if we trust that the $E_{0.37}$ peak did not contain a very large contribution from other defects, some mobile species that consumes E centers must be released at RT from an unstable source that was created during irradiation. Judging from the annealing curves, this source simultaneously causes the growth of new defects. Notice that the Ge self-interstitial itself has become mobile at a much lower temperature, probably around 200 K [163]. In *Si* a common contamination species, carbon, can indeed open up a manifold of electrically active defects [31] when interstitial carbon C_i becomes mobile at $\sim$ 50 °C (C_i is formed when irradiation-induced self-interstitials kick out substitutional C_s). It would not be unreasonable that C could pair with E centers. However, the picture is not transferable to Ge in which the C_s solubility is merely $10^8 - 10^{10}$ cm^{-3} [164]. Most likely, interstitial agglomerates have been created during irradiation, and a transient release of Ge self-interstitials I takes place at RT.

The levels of the A center and the E center seem to roughly resemble those in Si. But in recent DLTS experiments [165] on 2 MeV α-irradiated n-type $Si_{1-x}Ge_x$, the E center stands out clearly for x = 0, 0.05, and 0.15, but it has a very small amplitude for $x = 0.25$ and it is not detected for $x = 0.35$ or $x = 0.50$.[38] Tentatively, it is deduced that the E center level moves down in the band gap with x so that for $x \gtrsim 0.25$, communication with the valence band takes over [165]. In this light it is somewhat surprising to rediscover the E center level in Ge in the upper half of the band gap. (Going from $x = 0$ to

[38] The fact that Goubet and Stievenard [166] and Kringhøj and Larsen [167] did observe the E-centre in $Si_{70}Ge_{30}$ and $Si_{75}Ge_{25}$, respectively, is most likely related to slight uncertainties in the true composition x.

$x = 1$, the conduction band minimum is essentially fixed and identical to the Si X minimum until $x \approx 0.85$. Above this composition, the Ge L conduction band minimum moves down below X [168]. The valence band maximum steadily rises with x, and the band gap decreases from $E_g^{\mathrm{Si}} = 1.12$ eV to $E_g^{\mathrm{Ge}} = 0.66$ eV at RT.)

Emphasizing the difference from the Si case, the E center capture cross section turns out to be lower than that of the A center by more than an order of magnitude. The relevant measurements are reported in Fig. 10.10; the result is

$$\sigma_n^{E_{0.37}}(T) = 2.55 \times 10^{-17} \exp\left(-\frac{0.041\ \mathrm{eV}}{kT}\right)\ \mathrm{cm}^2 \tag{10.6}$$

$$\approx (1.1 - 2.4) \times 10^{-18}\ \mathrm{cm}^2 \tag{10.7}$$

at 150–200 K. The very small cross section of $E_{0.37}$ hints that $E_{0.37}$ is in fact a repulsive centre. I.e. $E_{0.37}$ could be the double acceptor level $(-/=)$ of the Sb E center that has moved down from the conduction band in Si, into the gap in Ge. Indeed, that would be consistent with the above-mentioned lowering of the 'silicon' $(0/-)$ level for $x \gtrsim 0.25$.

Possible corroboration of this idea is found in annealing experiments: We demonstrate from the E center profiles in Fig. 10.11 that the application of a reverse bias (4 V) will *impede* annealing of the E center in Ge. This contrasts the bias-enhancement of E center annealing in Si [169].

The slope of the as-irradiated (+ 15 days) profile in Fig. 10.11 shows that a number of vacancies from the irradiation-generated Frenkel pairs had diffused to the surface before they could be trapped by Sb-atoms. Comparing upper and lower panels of Fig. 10.11, we see that the application of a -4 V bias greatly reduces the role of the surface as a sink for E center annealing. At an annealing temperature of 120 °C the Fermi level [121] is approximately 0.08 eV below $E_{0.37}$ (since $\Delta G(E_{0.37}) = 0.23$ eV if we assume $g_0/g_1 = 1$). For the sake of discussion, let us assume that $E_{0.37}$ is a double acceptor $(-/=)$. In the bulk, due to the width of the Fermi level, each trap then has approximately a 9 % chance of being $(=)$, but in the depleted region a trap will always be $(-)$. The following scenarios are then compatible with the observed depth profiles:

(i) Suppose that the E center anneals by *diffusion*. When migrating E centers approach the surface, they will be driven back at some point where the electric field is strong enough. The field acts as a barrier for outdiffusion and as a driving force toward the bulk, and only very close to the surface (in the region not probed) is the E center concentration expected to decrease. Note that this scenario is compatible with $(-/=)$ charge states, but not with $(0/-)$. Alternatively, migration may simply be much smaller for the E centers within the depletion layer (e.g. Sb$V^{=}$) than for those E centers in the bulk that are in a different charge state (e.g. SbV^{-}).

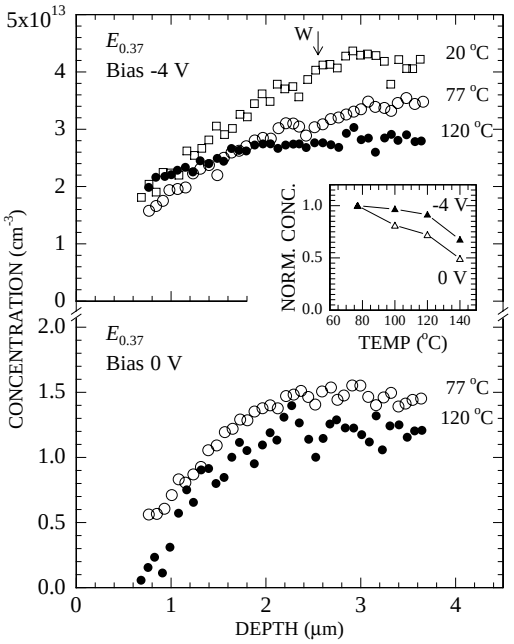

Figure 10.11: *E* center depth profiles in two diodes on the same *Sb2* sample, that were annealed either with a 4 V reverse bias or with no bias. The depletion layer width W at 4 V is indicated. Diodes had been electron-irradiated with somewhat different doses. Profiles were measured 15 days after irradiation (□), 3 months later after a 77 °C/5 min anneal (○), and after a 120 °C/10 min anneal (●). They were obtained at 205 K with DLTS double-pulse technique with a constant reverse bias of 20 V and a pulse difference $\Delta V = 1.00\ V$. Inserted are annealing curves with (▲) and without (△) bias, as observed by DLTS using -4 V → 0 V.

(ii) Suppose that the *E* center anneals by *dissociation* and vacancy loss to the surface. Dissociation should then be suppressed under reverse bias, meaning, e.g., that the $(-)$ charge state should be more stable than (=). This stabilization should be stronger than the opposite tendency that the electric field will have to separate the positive Sb^+ from the negative vacancy. Or, alternatively, the mobility of the vacancy could be reduced in the depletion region (although this opposes the Si situation where, e.g., V^- is more mobile than $V^=$) [5].

In the 'silicon picture' [169] the annealing without bias should have been slower due to the energy cost (0.23 eV) of first converting Sb$V^=$ into the less stable SbV^-. From the above discussion it is clear that this picture does not hold for SbV annealing in Ge – except possibly in the diffusion scenario: Even if SbV^- *were* more mobile than Sb$V^=$, the electric field could in fact retard the annealing by restraining SbV^- from outdiffusion .

10.4.3 Level $H_{0.30}$

This hole trap strongly dominates the minority spectra in both of the Sb-doped samples (Fig. 10.3), but neither before nor after anneal does it appear in the

oxygen-doped Ge (Fig. 10.4).[39] When detected with injection-pulse DLTS the $H_{0.30}$ amplitude increases steadily for anneals above $\sim$ 120 °C, but when applying MCTS with front-side illumination a moderate decrease is observed, see Fig. 10.9. To our knowledge, all studies of minority traps in irradiated Ge have hitherto been performed with injection-pulse DLTS.

$H_{0.30}$ resembles $H(0.24)_{\mathrm{Fuk}}$ (E_v+0.24 eV). This level, present as the only minority trap after 1.5 MeV electron irradiation of 1.5×10^{14} and 2.5×10^{15} cm^{-3} Sb-doped Ge [151], had a small decrease upon 70 °C annealing but increased in amplitude during several hours at 107 °C. $H(0.24)_{\mathrm{Fuk}}$ was found in neither of two As-doped samples, but prominent was instead $H(0.29)_{\mathrm{Fuk}}$ which we propose to be the As analog. Annealing behaviour of $H(0.29)_{\mathrm{Fuk}}$ was not reported. Also similar, the level $H_{2,\mathrm{Bou}}$ at E_v+0.30 eV in 2 MeV e-irradiated, 10^{13} cm^{-3} n-type Ge increased above $\sim$ 120 °C and finally annealed at $\sim$ 250 °C [160]. From irradiation-energy threshold experiments it was excluded that $H_{2,\mathrm{Bou}}$ originated from two-atom displacements [170].

Hence, by combining our observations with those from the literature, strong indications arise that $H_{0.30}$ is formed when one or more simple defects, i.e. vacancies or interstitials, meets with an Sb atom.

We demonstrated with Fig. 10.6 that $H_{0.30}$ is strongly attractive to holes, i.e. it is an acceptor level. Bearing in mind the analysis of Sec. 10.4.2 it is tempting to propose that $H_{0.30}$ is the $(0/-)$ transition of the E center: If the E center level $E_{0.37}$ were indeed $(-/=)$, of which we pointed out indications, then $(0/-)$, with a stronger Coulomb binding of the electron, is expected to be present below $E_{0.37}$, very likely within the band gap.

Against this picture apparently speaks the different annealing behaviours of $E_{0.37}$ and $H_{0.30}$ (Figs. 10.7 and 10.9). But one must be cautious here, since $H_{0.30}$, probed with a hole concentration that decays exponentially from the interface, is detected with particularly high sensitivity very near the interface (see footnote 39). When observed with injection-pulse DLTS, the $H_{0.30}$ amplitude increases above $\sim$ 120 °C which is the temperature at which $E_{0.37}$ starts to anneal. The possibility must therefore be considered that $H_{0.30}$ and $E_{0.37}$ are related and that the $H_{0.30}$ increase is a consequence of the abnormal E center redistribution, combined with a different annealing characteristics of the particular E center charge state that prevails very near the interface. – Certainly, different annealing behaviours are exposed with MCTS and with injection-DLTS.

If not a coincidence that $H_{0.30}$ increases when $E_{0.37}$ starts to anneal, other candidates for $H_{0.30}$ are defects that are formed from SbV migration. An example could be Sb_2V which would have a relatively low abundance directly after irradiation. As detailed earlier, an interstitial flux seemed to appear at

[39] In fact, in *Sb*1 and *Sb*2, but not in *Ox*, a strong $H(0.30)$ signal is induced even by the near-surface damage that is created by electron gun diode evaporation of Au, Pt or Pd. Since no electron traps are seen, the damage is closer to the surface than the depletion layer width W_0. Thermal Au evaporation induces no defects in any material.

low temperature, and that did not cause a $H_{0.30}$ increase.

10.4.4 Level $E_{0.29}$

In *Sb2* Ge, $E_{0.29}$ cannot be positively detected at any time after electron irradiation. But following proton irradiation, $E_{0.29}$ stands out after a 110 °C anneal when $E_{0.30}$ has disappeared. This was demonstrated in Fig. 10.2. The line width is $\sim$ 65 % larger than expected for a 0.29 eV line, so $E_{0.29}$ is in fact a sum of two close-lying levels.

The concentration of $E_{0.29}$ prior to heating of the sample is somewhat uncertain; we can only estimate that the amplitude must have been $\lesssim$ 75 % of the amplitude after 110 °C.

In *Sb1* Ge, $E_{0.29}$ is almost hidden under the *A* center $E_{0.27}$ or under $E_{0.28}$. Upon proton irradiation and a 110 °C anneal (giving a slight *A* center decrease), the existence of $E_{0.27}$ is clear, but before sample heating we can only say that the amplitude must have been $\lesssim$ 120 % of the amplitude after 110 °C. On electron-irradiated *Sb1* a systematic annealing series was not performed.

In proton-irradiated, O-doped Ge a small shoulder to the *A* center can be seen when the *A* center has strongly decreased after 156 °C anneal. The shoulder is possibly, though not certainly, $E_{0.29}$.

Thus, the introduction rate of $E_{0.29}$ relative to other defects in *Sb2* Ge is multiply enhanced with proton relative to electron irradiation. $E_{0.29}$ is most likely present immediately after proton irradiation (but hidden beneath other peaks). It is introduced also in *Sb1*, and possibly in *Ox*. Hence, $E_{0.29}$ meets the requirements, as the only level, of one that is related to a displacement of more than one host atom and probably does not involve a dopant atom. We propose that $E_{0.29}$ belongs to a divacancy or a diinterstitial.

10.4.5 Levels $E_{0.13}$, $E_{0.19}$, and $E_{0.23}$

These defects appear in *Sb1* and *Sb2* after both electron and proton irradiation, but not in *Ox*. At RT $E_{0.13}$ and $E_{0.19}$ transiently grow in with almost identical concentrations and anneal again over a few days. Most likely, $E_{0.13}$ and $E_{0.19}$ are therefore different (close-lying) charge states of the same defect. $E_{0.23}$ grows in after longer time at RT and anneals at $\sim$ 110 °C.

$E_{0.13}$ and $E_{0.19}$ were observed also by Zistl [162] in 1.2 MeV e-irradiated, 2×10^{15} cm^{-3} Sb-doped Ge: The levels $ET1_{\text{Zis}}$ and $ET2_{\text{Zis}}$ are at 0.14 eV and 0.19 eV, and both anneal at RT. Moreover, in a temperature scan down to 100 °C a defect $E_{3,\text{Bou}}$ [171] that was unstable at RT appeared close to the position of $E_{0.19}$.

$E_{0.23}$ matches $E(0.23)_{\text{Fuk}}$ [151] which grows in during a couple of hours at $\sim$ 70 °C and anneals at $\sim$ 110 °C. This level was seen in 1.5×10^{14} and $2.5 \times$

10^{15} cm^{-3} Sb-doped Ge after 1.5 MeV electron irradiations. It also matches $ET3_{\mathrm{Zis}}$ at 0.22-0.23 eV [162]. $ET3_{\mathrm{Zis}}$ grows in at RT, anneals at $\sim$ 110 °C and is seen in 2×10^{15} and 1×10^{16} cm^{-3} Sb-doped material.

These observations very strongly suggest that $E_{0.23}$ is Sb-related. In As-doped Ge, Fukuoka and Saito [151] did not detect a level that resembled $E(0.23)_{\mathrm{Fuk}}$, but annealing experiments were not reported.

Since $E_{0.13}$, $E_{0.19}$, and $E_{0.23}$ are not produced in the collision cascade, they must be formed from thermal transformation of one defect species and/or from capture of defects that are released from another. From the time and temperature evolutions in both *Sb1* and *Sb2* it appears that the same defect source (presumably interstitials) as that which reduces $E_{0.37}$ at RT is responsible for the growth of $E_{0.13}$, $E_{0.19}$, and $E_{0.23}$. Hence, we arrive at the conclusion that $E_{0.23}$ contains an Sb atom, very likely in relation with an interstitial-related defect.

Formation of $E_{0.13}$ and $E_{0.19}$ *precedes* formation of $E_{0.23}$. It is possible that a small energy barrier exists to the formation of $E_{0.23}$, and $E_{0.13}$ and $E_{0.19}$ may even be two levels of a metastable 'precursor' configuration to the former.

$E(0.23)_{\mathrm{Fuk}}$ was speculated to be created from a vacancy flux at $\sim$ 70 °C and to be $\mathrm{Sb}_i V$ [151]. However, that does not fit with the foregoing discussion. In particular, it can be seen that a vacancy-injection which would have increased the E center concentration is not supported by our annealing curves (Fig. 10.7).

10.4.6 Levels $E'_{0.19}$ and $E_{0.14}$

These levels are detected only in the *Ox* material. $E'_{0.19}$ increases after an 138 °C anneal, shortly before the A center anneals. $E_{0.14}$, as a small shoulder, follows closely the growth and decrease of $E'_{0.19}$. The annealing characteristics of $E'_{0.19}$ is very close to those of $E(0.13)_{\mathrm{Fuk}}$ [152] (created after 120 °C anneal, slow disappearance between 160 and 300 °C) and $E_{5,\mathrm{Nag}}$ [153] ($E_c - 0.17$ eV, $T_{\mathrm{ann}} \sim$ 225 °C) that both occurred next to the A center in heavily O-doped Ge. It is unclear why there is an energy discrepancy with $E(0.13)_{\mathrm{Fuk}}$.

10.4.7 Levels $E_{0.30}$, $E_{0.28}$, and $E_{0.21}$

$E_{0.21}$ is observed in *Sb2* and, with smaller amplitude, also in *Sb1*. It grows in above $\sim$ 90 °C and anneals at $\sim$ 180 °C. The maximum amplitude (relative to the E center) is enhanced only slightly by proton vs. electron irradiation. The level may be Sb-related, but other than $ET2_{\mathrm{Mar}}$ [154] and $E_{1,\mathrm{Nag}}$ [153] literature reports of this defect are elusive (see Tab. 10.2 and Sec. 10.4.8 below).

$E_{0.30}$ is observed only in *Sb2*; it is found after both electron and proton irradiation. $E_{0.30}$ grows in and anneals again during several days at RT. Referring to Sec. 10.4.5, this behaviour may be indicative of an interstitial-related defect.

$E_{0.28}$, seen after irradiation of *Sb1* Ge only, grows in above 170 °C and anneals at $\sim$ 270 °C. Prior to annealing, if present, $E_{0.28}$ is hidden directly below the A center $E_{0.27}$. The growth, annealing, and energy level of $E_{0.28}$ resembles that of $E(0.29)_{\mathrm{Fuk}}$ from heavily O-doped Ge [152] (which did peak, however, in the DLTS spectrum at a higher temperature than the A center). $E(0.29)_{\mathrm{Fuk}}$ was associated with an 819 cm^{-1} infrared absorption band [155] that resembled a defect-di-oxygen complex or a complex containing oxygen and a different impurity atom [155]. Acknowledging that *Sb1* contains oxygen, this description, though speculative, is not untenable for $E_{0.28}$ also.

In any case, it is plausible that $E_{0.30}$ and $E_{0.28}$ are related to residual impurities in Ge.

10.4.8 Variations In the Literature

It has now been established that several electronic levels exist in n-type Ge, for which agreement can indeed be found on energy level and annealing behaviour [151, 152, 153, 162].

However, extensive DLTS investigations of (0.5–3 MeV electron-) irradiated n-type Ge were performed first by the Bourgoin group [150, 160, 171, 172, 159], but the remarkably large values of the enthalpies [159] render impossible a direct comparison with the enthalpies of this study. On grounds of the annealing behaviour the levels $E_{2,\mathrm{Bou}}$ (0.53 eV; $T_{\mathrm{ann}} \sim 150$ °C) and $E_{1,\mathrm{Bou}}$ (0.32 eV; $T_{\mathrm{ann}} \sim 110$ °C) were identified, respectively, with the A center and the E center [160], but we now see that most likely $E_{2,\mathrm{Bou}} = E_{0.37}$ (E center) and $E_{1,\mathrm{Bou}} = E_{0.23}$ (Sb-related). This is inferred from the annealing temperatures and from the defect ordering in the spectra. Comparing still with $E_{0.37}$, it is worth mentioning that out of four defects, $E_{2,\mathrm{Bou}}$ was found to have by far the smallest capture cross section [159]. (However, our measurement on $E_{0.37}$ now reduces the absolute value by a factor of $\sim$ 25).

Further, studies of the energy threshold of defect introduction [172] lead to the conclusion that the close-lying levels $E_{4,\mathrm{Bou}}$ (0.46 eV, $T_{\mathrm{ann}} \sim 150$ °C) and $E_{5,\mathrm{Bou}}$ (0.42 eV, $T_{\mathrm{ann}} \sim 150$ °C) were divacancy-related. Like $E_{0.29}$, the levels $E_{4,\mathrm{Bou}}$ and $E_{5,\mathrm{Bou}}$ appeared in the spectra at a slightly lower temperature than the E center (i.e. $E_{2,\mathrm{Bou}}$). It seems reasonable that $E_{4,\mathrm{Bou}}$ and/or $E_{5,\mathrm{Bou}}$ are the same as $E_{0.29}$ that contains two close-lying levels and which we indeed attribute to the divacancy.[40]

A word is appropriate also on the studies by Marie *et al.* [154, 173]. They irradiated 2.4×10^{14} cm^{-3} Sb-doped Cz-Ge with high-energy ($\sim 0.3 - 6$ GeV) heavy ions, but for a reason yet to be understood the apparent enthalpies [154]

[40] After 2 MeV electron irradiation the divacancy levels $E_{4,\mathrm{Bou}}$ and $E_{5,\mathrm{Bou}}$ appeared with relatively large amplitudes in the spectra of Ref. [160]. This simply reflects that vacancy trapping at impurities was modest; the donor atom concentration itself was merely 10^{13} cm^{-3}.

of the defects so obtained differ markedly from the enthalpies obtained with electron and proton irradiation. If we reinterpret their assignments, with an eye on the defect ordering and annealing temperatures, it now seems clear that $ET5_{\mathrm{Mar}}$ (0.47 eV, $T_{\mathrm{ann}} \sim 150$ °C) is the same as $E_{0.37}$ (E center) and highly probable that $ET3_{\mathrm{Mar}}$ (0.29 eV, $T_{\mathrm{ann}} \sim 90$ °C) is the same as $E_{0.23}$ (Sb-related). Here we rely on the value of 150 °C, rather than 90 °C [151], of the A center annealing temperature - which makes it unlikely that $ET3_{\mathrm{Mar}}$, and also $E_{1,\mathrm{Bou}}$, should be identified with the A center $E_{0.27}$.

A divacancy level is anticipated from the heavy-ion irradiations, and a highly plausible candidate is $ET4_{\mathrm{Mar}}$ (0.32 eV, $T_{\mathrm{ann}} \sim 140$ °C) [154] which has the proper position in the spectra. But from arguments based solely on the annealing behaviour it is hard to see that $ET2_{\mathrm{Mar}}$ (0.28 eV, amplitude doubles at ~ 90 °C, $T_{\mathrm{ann}} \sim 150$ °C) should in fact be related to the divacancy levels $E_{4,\mathrm{Bou}}$ and $E_{5,\mathrm{Bou}}$. The suggestion [173] that $ET2_{\mathrm{Mar}}$ and $ET4_{\mathrm{Mar}}$ are merely single and double acceptor states of the same defect is not easily justified, owing to the fact that $ET2_{\mathrm{Mar}}$ strongly increased with a 90 °C anneal, whereas $ET4_{\mathrm{Mar}}$ did not [154]. $ET2_{\mathrm{Mar}}$ is positioned in the spectra at a relatively low temperature, close to $E_{0.21}$, and indeed they have a similar annealing behaviour.

10.5 Summary

Ge with three types of doping was investigated. Crystals contained respectively 2.5×10^{14} cm^{-3} Sb, 1.2×10^{15} cm^{-3} Sb, and 7×10^{16} cm^{-3} O. Strong defect evolution at RT was observed in both Sb-doped materials after 2 MeV proton or electron irradiation, and the dynamics is compatible with the existence of a source of interstitials. Contrary to the Si case, annealing of the Sb E center, $E_{0.37}$, is retarded under reverse bias. Temperature-dependent electron capture cross sections were measured for the E center and for the A center, $E_{0.27}$; they are near 1.5×10^{-18} cm^2 and 2×10^{-17} cm^2, respectively. It was speculated that $E_{0.37}$ is the double acceptor level of the E center. A trap, $E_{0.23}$, is related to Sb and seemingly grows up by interstitial capture, possibly hindered by a small barrier. The amplitude of a trap $E_{0.29}$ is strongly enhanced by proton relative to electron irradiation, and $E_{0.29}$ is suggested to be divacancy-related. One significant hole trap, $H_{0.30}$, was present in Sb-doped but not in O-doped material. The apparent annealing behaviour of $H_{0.30}$ depends on the mode of detection (MCTS or injection-pulse DLTS). $H_{0.30}$ is strongly attractive to holes, and whereas firm identification cannot be made, we cautiously presented the idea that it be the single acceptor level of the E center. Correspondence was pointed out between seemingly varying literature results.

Acknowledgements

We thank Prof. Paul Clauws for providing us with the oxygen-doped Ge samples. Our work was supported by the Danish Natural Science Research Council.

Chapter 11

Comments on deep levels in *n*-type Ge

Brief comments are attached to the article [IV] that was presented in Chap. 10, and to recent reports in the literature. A discussion is provided on the change of the E center level as the band gap shrinks with the Ge content in $Si_{1-x}Ge_x$, going from Si to Ge. (The reader is also referred to appendix A where a discussion is presented on the hole filling of the $H_{0.30}$ acceptor level as a function of optical filling pulse duration.)

11.1 On the defect levels in Ge

We demonstrated [IV] in the previous chapter that no clear-cut picture exists in *n*-type[41] Ge in terms of identifying the particular lattice defects that are associated with even the most common, irradiation-induced deep levels. In combination with the experiments that were presently conducted [IV], an important issue was to objectively collect and analyse much of the existing knowledge, thus advancing a small step towards an improved description of defects in Ge. It was attempted to give an overview of independent experimental findings in Tab. 10.2, but it is clear that many answers still need to be found, and new questions need to be asked.

Among the primary results was the firm establishment of $E_{0.37}$ as an acceptor level (possibly double acceptor level) of the *E center*. Almost concurrently with the publication of article [IV], a DLTS study was published by Colder, Levalois, and Marie [174]. In this study, it was now acknowledged that $ET5_{\mathrm{Mar}}$ must indeed be the Sb *E* center. Interestingly, Colder *et al.* had irradiated both As and Sb doped Ge with 328 MeV Ne ions, and they came to the conclusion that the As *E* center level is more shallow than the Sb *E* center level. This point was also made in article [IV] from inspection of the spectra of Fukuoka and Saito [151, 152]. Upon irradiation with 328 MeV Ne ions, Colder, Levalois,

[41] A quick survey of the literature will reveal that the amount of knowledge of defects in *p*-type Ge, much akin to that in *n*-type, is rather modest.

and Marie find that $E_c - E_t \approx 0.46$ eV for $ET5_{Mar}$ in Sb-doped Ge but that $E_c - E_t \approx 0.31$ eV for $ET5_{Mar}$ in As-doped Ge. This observation is most surprising, since in Si, the E center levels originating from P, As, and Sb lie very close, approximately between $E_c - 0.43$ and $E_c - 0.47$ eV [175, 176, 177]. Similar spectra seem to be obtained from high-energy heavy-ion irradiations and 12 MeV proton irradiations [174].

It was demonstrated in the same article [174] that with the application of a more gentle-type irradiation, namely 2 MeV electrons, the E center peak is shifted approximately 20 °C toward lower temperature (from approximately 210 to 190 K). This is in agreement with the fact that relatively *deep* level locations have been reported by Marie *et al.* [154] after heavy-ion irradiations. It is also true that heavy-ion irradiation can produce large defects, for example multivacancy clusters. Colder *et al.* suggest that the movement [174] of the E center peak position toward a higher temperature when *heavy-ion* irradiation is applied, is only an apparent movement, and that, in reality, an additional peak (from a multivacancy-cluster) has been introduced at the highest temperature in the spectrum. This proposition is not unreasonable, but if the 210-K peak (Fig. 3 in Ref. [174]) is in fact a sum of a 190-K peak (the E center) and a higher-temperature peak (multivacancy cluster), then the E center introduction rate from heavy-ion irradiations has to be surprisingly low compared with the other defects. I.e., the formation of E centers should be strongly suppressed when the multivacancy defect forms. However, the proposed level of the multivacancy defect, $\sim E_c - 0.55$ eV, is extremely low in the band gap of Ge ($E_g = 0.66$ eV at RT), and such a defect would be expected to act as a hole trap and not show up in a majority carrier spectrum.

So it does not yet seem fully justified that the apparent shift of the E center (with higher mass and energy of the bombarding species) should signal the introduction of a *new* defect. Instead, it is possible that one needs to find a physical explanation for a *distortion* of the level position. In favour of this interpretation speaks the observation that not only the (presumed) E center $ET5_{Mar}$, but also the other defects $ET2_{Mar}$, $ET3_{Mar}$, and $ET4_{Mar}$ are deeper than those observed after 2 MeV electron or proton irradiation by these authors [IV] and by Fukuoka and Saito (Tab. 10.2). As a (rather loose) speculation, one way to explain distortion of levels would be to invoke band-gap alteration due to the lattice strain that can be induced when extended defects are introduced in the Ge lattice [178].

It is shown [174] that $ET3_{Mar}$ grows in during long-term room temperature annealing. This corroborates our proposition that $ET3_{Mar}$ is the same as $E_{0.23}$ (Sb and I related), and it shows that $ET3_{Mar}$ can not be the A center [174] since the A center is induced directly during irradiation.

11.2 On the E center in $Si_{1-x}Ge_x$, $0 \leq x \leq 1$

A number of hints were found [IV] that $E_{0.37}$ could possibly be the doubly charged acceptor state of the Sb E center in Ge. Accordingly, $H_{0.30}$ would be a plausible candidate for the singly charged acceptor level. We can summarize the most relevant clues:

- The cross section for electron capture at $E_{0.37}$ is very small, $\sigma_n \sim 1.5 \times 10^{-18}$ cm^2, compared with $\sim 2 \times 10^{-17}$ cm^2 for the A center (Fig. 10.10).
- Annealing of $E_{0.37}$ is oppressed by application of a reverse bias (Fig. 10.11). This observation can possibly be explained if the E center anneals primarily by diffusion[42] and if one makes the assumption that outdiffusion of E centers is hindered by the electric field. This field supplies a driving force toward the bulk, but the probed region is not drained of E centers since the E center concentration initially has a slight gradient toward the surface. The electric-field assumption necessitates that E centers be negative (–) near the interface; this will be valid for a (–/=) E center level but not for a Si-like (0/–) level (see discussion on p. 115).
- $H_{0.30}$ was detected by several authors in n-type Ge (Sec. 10.4.3) and we infer that it can be related to the donor atom. Conversely, we did not see indication of $H_{0.30}$ in oxygen-doped Ge.
- The barrier for hole emission from $H_{0.30}$ is radically decreased with increasing electric field (Fig. 10.6). This is an example of the Poole-Frenkel effect, indicating that $H_{0.30}$ (when empty of holes) has a long range (i.e., Coulombic) attraction to holes. Therefore, $H_{0.30}$ is certainly a donor level.
- Finally, we insinuated that the (0/–) level of the E center in Si moves toward the lower half of the band gap when an increasing fraction of Ge is added to the material. Thus, in Ge-rich SiGe, one is not *a priory* guaranteed to rediscover the (0/–) level in the upper half of the gap.

Let us be more specific regarding the final point above; the shift of the E center single acceptor level with Ge composition in SiGe alloys. Relevant data on this matter was recently produced by Skarði [179], and a thorough reinvestigation of the E center in this system is currently ongoing [165]. In Fig. 11.1, we show DLTS spectra that were obtained in n-type, MBE-grown $Si_{1-x}Ge_x$ alloys, $0 \leq x \leq 0.5$. The alloys had been irradiated at room temperature with 2 MeV α particles. The identification of the individual levels is shown in the figure. It is remarkable that the E center can be followed up to $x = 0.15$ % but in

[42] For example, in Si it does appear that the E center anneals primarily by diffusion (see [6] and refs. therein). However, a small fraction of E centers do dissolve; this is signalled by a modest increase of the divacancy level.

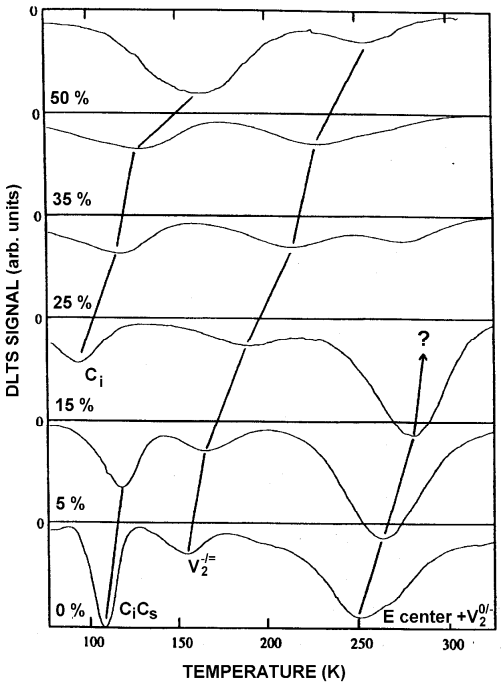

Figure 11.1: DLTS spectra from n-type Si and $Si_{1-x}Ge_x$ up to $x = 50$ %, measured after 2 MeV α-particle irradiation. The E center peak is overlapped with a smaller peak from the single acceptor level of the divacancy, $V_2^{0/-}$; this level has the same amplitude as $V_2^{-/=}$, the double acceptor level of the divacancy. C_i is interstitial carbon, and C_iC_s is interstitial carbon next to substitutional carbon. After Skarði [179].

$Si_{0.75}Ge_{0.25}$, the level is not easily discernible, and at higher Ge concentrations, the level does not appear in the spectra. With increasing Ge content, the peak is shifted toward higher temperatures as was also observed by Kringhøj and Nylandsted Larsen [167] (see also footnote 38 on p. 114).

There is little reason to believe that E centers should *not* be produced by irradiation in compounds that have a Ge content higher than ~ 0.25. A different guess, as to why the E center disappears from the spectra, would be that the E center starts to communicate with the valence band rather than the conduction band at a Ge fraction $x \approx 0.25$. Since the band gap shrinks when x is increased, such a guess seems well qualified.

The changeover can be evaluated from simple considerations [179]. When carriers are exchanged with both bands, the fraction of traps that give a majority-carrier signal is

$$\Delta n_t = \frac{e_n}{e_p + e_n}. \tag{11.1}$$

The electron emission rate was given in Eq. (9.4). From this equation, $e_n \propto \exp[-(E_c - E_t)/kT]$, and similarly, $e_p \propto \exp[-(E_t - E_v)/kT]$. For the purpose of calculation, assume that the fraction of detected traps at two different

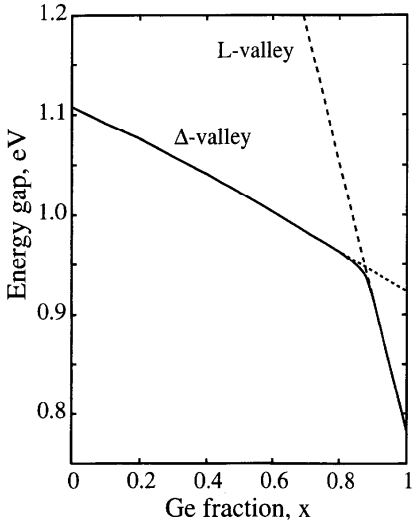

Figure 11.2: The variation of the indirect band gap with Ge content x in $Si_{1-x}Ge_x$, calculated with pseudopotentials with a virtual crystal approximation [180]. From Shaw and Jaros [180]

Ge concentrations are $\Delta n(x = 0.20) = 0.95$ and $\Delta n(x = 0.30) = 0.05$. For simplicity, we will neglect possible composition-dependent changes of the prefactors of e_n and e_p. If we take into account that the band gap, $E_g = E_t - E_c$, is reduced by approximately 0.03 eV from $Si_{0.8}Ge_{0.2}$ to $Si_{0.7}Ge_{0.3}$, we can use the above relations to estimate that the E center has moved down in the band gap by approximately 0.06 eV. *That is, a reduction of the normalized E center peak amplitude from 0.95 in $Si_{0.8}Ge_{0.2}$ to 0.05 in $Si_{0.7}Ge_{0.2}$ can be explained if $E_t - E_c$ has increased by approximately 0.06 eV in that composition range*. Thus, these results strongly indicate the the (0/−) level moves *downward*, i.e., further away from the conduction band, with increasing Ge content.

The change of the band gap from Si to Ge, calculated by Shaw and Jaros, can be seen in Fig. 11.2. For a measurement of the band-gap energy, see Weber and Alonso [168]. The valence band maximum is at the Γ point of the Brillouin zone throughout the whole composition range, but the conduction band minimum changes: The Si-like Δ valley (which is in the X direction of the Brillouin zone) dominates up to $x \approx 0.85$, and at higher values of x, the Ge-like valley at the L point moves down below the Δ valley.

The DLTS results show that the E center (0/−) level has moved down in the lower half of the band gap, such that at $x = 0.5$ the level is not seen with majority-carrier DLTS. So the question is: how does the E center level scale in the composition range $0.5 < x \leq 1$, and what happens when the Ge-like L valley moves down? If the E center (0/−) level does *not* follow the movement of the the L valley, the possibility exists that the valley comes down in such a way that it closes again the distance from the conduction band minimum to the

(0/–) level. Yet, there were several indications [IV] that the Ge-side E center level $E_{0.37}$ is a *double* acceptor, (–/=). If we lean on this interpretation, we can conclude that the (–/=) level must move down into the gap at some $x > 0.5$. Therefore, to some extent $E_{0.37}$ follows the movement of the L valley.

It is clear that to solve these issues, the best and most critical test would be to perform DLTS investigations in Ge rich SiGe alloys. However, such alloys, if grown from the Ge side, contain high defect concentrations, and only recently has successful attempts [181] been made at growing Ge rich SiGe from the Si side. An alternative, possible means of revealing if $E_{0.37}$ and $H_{0.30}$ are coupled levels, is described in Appendix A.

11.3 A digression: Arsenic diffusion in Ge

Finally, a very special interest is found in a recent observation by Vainonen-Ahlgren and coworkers [40]: They found that As diffusion in Ge with As maximum concentrations of a few times 10^{19} cm^{-3} had the following donor dependence (in a straight-forward notation):

$$D_{\mathrm{As}}^{\mathrm{eff}} = D_{\mathrm{As}}^{0} + D_{\mathrm{As}}^{=} \left(\frac{n}{n_{\mathrm{i}}} \right)^{2}. \tag{11.2}$$

From this result, they inferred, according to the standard diffusion model [Eq. (2.37)] that the vacancy in Ge exists in the neutral (0) and the double-negative (=) charge state. Since no (–) term was found, the vacancy was suggested [40] to be a negative-U system. The latter conclusion, however, is in disagreement with theory [182]. It is appealing to suggest, alternatively, that the $(n/n_{\mathrm{i}})^{m}$ ($m = 0, 1, 2$) dependence in Eq. (11.2) [and in the standard model, Eq. (2.37)] does not reflect the distribution of *vacancy* charge states but rather the distribution of E *center* charge states. This suggestion can immediately explain why donor diffusion in Si [with a (0/–) E center level] increases as n/n_{i}, whereas donor diffusion in Ge [with a (–/=) E center level] increases as $(n/n_{\mathrm{i}})^{2}$.

In fact, it is not hard to motivate the above suggestion, since the standard model [Eq. (2.37)] neglects that the E centers possess energy levels in the band gap. One can argue that the E centers will automatically adjust to the most desirable charge states, which is independent of the initial charge state of the vacancy with which they interacted. For diffusion issues, Eq. (2.37) is of course the same, practical tool in any case.

Chapter 12

Summary and Conclusions

The road to wisdom? - Well, it's plain
and simple to express:
Err
and err
and err again
but less
and less
and less.

PIET HEIN

The author presents an experimental study of the interactions among impurity atoms and between native point defects and impurity atoms in crystalline Si, SiGe, and Ge. Native *point defects* are the lattice vacancies and the self-interstitial atoms. The *impurity atoms*, in relation to the present studies, are dopant atoms that have been deliberately introduced during growth of the material. The thesis can roughly be divided into two parts:

In one part, the *redistribution* of dopants in Si and $Si_{1-x}Ge_x$ alloys ($0 \leq x \leq 0.4$) at elevated temperatures has been studied by measuring the chemical depth profiles. For these studies, samples have been grown with dopant profiles that have been especially designed for the particular purposes. The depth profiling technique is secondary ion mass spectrometry (SIMS), and the growth technique is molecular-beam epitaxy (MBE). Due to the pushing demands of miniaturization, precise knowledge and control of the redistribution (diffusion) of dopant atoms has pivotal importance in microelectronic device fabrication.

In a second part, *electrical measurements* have been employed on bulk Ge in which point defects have been deliberately produced by electron or proton irradiation of the material. Point defects and impurity–point defect complexes may introduce deep levels in the forbidden band gap of the semiconductor, such that electrons and holes are exchanged between the defect and the electron and valence band, respectively. The employed techniques, which are sensitive to carrier capture and emission processes, are deep-level transient spectroscopy (DLTS) and minority-carrier transient spectroscopy (MCTS). Deep-level studies provide fundamental information on the kind of defects that may form and how defects interact with one-another. Deep levels, even if present in

very small concentrations, can sometimes influence minority carrier properties in a way that can be critical for some devices. Doped Ge is studied mainly for fundamental reasons, and because it resembles Si and, thus, constitutes a test bed for defect knowledge in Si.

Specifically, the following topics have been studied:

Vacancy-mediated diffusion in Si at high dopant concentrations: The case of Sb diffusion in a high Sn-background concentration in Si.

The diffusion of certain impurity atoms in Si is dependent on the interaction between the impurity atoms and the lattice vacancies. By far the largest amount of data on vacancy-mediated diffusion comes from group-V elements at high concentrations in Si. However, much controversy exists on the diffusion mechanisms at very high dopant concentrations, and one complicating factor is that the Fermi level rises with dopant concentration, thereby increasing the concentrations of negatively charged defects. To test existing theories on high-concentration diffusion, Sb diffusion was examined as a function of Sn-background concentration. This particular system is ideal for a simplified diffusion study for the reasons (i) that Sb diffuses purely by a vacancy-mediated mechanism, and (ii) that Sn, being isovalent with Si, does not change the Fermi level, yet, Sn is known to be attractive to vacancies.

At 995 °C, we found that Sb diffusion is enhanced when the Sn-background concentrations exceeds $\sim 5 \times 10^{19}$ cm^{-3}. Small amounts of Sn went into precipitates, but we estimated that the effect upon the Sb diffusion at diffusion times of $\sim$ 2–3 hours was very small, though possibly retarding. We argued from the diffusion data that *a collective phenomenon ('vacancy percolation') can not be applied to explain the diffusivity enhancement in the system*. Instead, it was made likely that *the diffusion may be mediated by Sb-Sn-V triple complexes*. Solid evidence of diffusion via such complexes has not been seen before. Nevertheless, an analysis of experimental data in the literature corroborates that triple complexes are likely to participate in the high-concentration diffusion of large-size dopant atoms in Si.

Impurity vacancy complex formation in Si: Si self-interstitial injection from Sb complex formation

The issue of complex formation and the metastability of highly doped layers in Si can be critical for device production. We demonstrated that diffusion is enhanced in a B marker layer if the layer is situated next to a high-concentration (1.1×10^{20} cm^{-3}) Sb box profile in Si. Since B diffuses via Si self-interstitial atoms, I, this shows that *self-interstitials are released from the Sb layer during annealing*. A large fraction of Sb goes into precipitates, but the diffusion

enhancement of B is not correlated in temperature with Sb precipitate formation. Instead, we suggest that *the interstitials are produced in a kickout reaction*, $Sb_nSi \rightarrow Sb_nV + I$, primarily with n=2 since the number of injected interstitials, from a simple estimate, is compatible with the statistically expected number of Sb_2 configurations in Si. In the literature, I injection has been observed also for As layers in Si. However, it is argued for group-V impurities in general, that the majority of the impurity–vacancy complexes that are generated at high temperature are *not* created in kick-out processes, but rather through capture of vacancies generated at the surface.

Interstitial-mediated diffusion in Si and SiGe: The influence of composition and biaxial strain upon P and B diffusion

Ge is fully miscible with Si, thus, any $Si_{1-x}Ge_x$ compound, $0 \leq x \leq 1$, can be fabricated and it will be thermodynamically stable. Since the lattice constant varies with x, a thin $Si_{1-x}Ge_x$ layer that is grown on Si, will contain biaxial strain. In modern Si/SiGe heterostructures, one must understand how dopant diffusion is affected both when the Ge content x, and when the amount of biaxial strain is varied. In the present investigation, P and B diffusion have been studied in such structures that were either relaxed or had compressive or tensile strain. Ge contents up to $x = 0.4$ were investigated. P and B both have an interstitial-related mechanism, and it is demonstrated that *the thermodynamics of P and B diffusion in relaxed and strained SiGe is fundamentally different from that of vacancy-mediated diffusers*. In particular, B diffusion is retarded at even very little Ge content, thus, B apparently pairs easily with Ge atoms into a configuration with low mobility. Under influence of biaxial strain, the activation enthalpies of P and B diffusion are significantly changed; these changes are correlated with changes in the entropy of diffusion.

Irradiation-induced defects in Ge studied by transient methods.

Very little is yet known about defects in Ge, and much uncertainty prevails even on the most common, irradiation-induced defects. Presently, we investigated Ge crystals that were doped either with O or with Sb, the latter with two different concentrations. On account of the spectra from these samples and annealing experiments, we attempt to clarify the proper assignment of defects with the peaks in the DLTS spectra. The results is displayed in Tab. 10.2 on p. 112.

We observed that strong evolution of defects took place at room temperature in the two Sb-doped materials after 2 MeV proton or electron irradiation, and the dynamics between the defects is compatible with the existence of a source of interstitials. In annealing experiments, we find that, *contrary to the Si case, annealing of the E center (the Sb–vacancy pair), $E_{0.37}$, is retarded under reverse*

bias. Temperature-dependent electron capture cross sections were measured for the E center and for the A center (oxygen–self-interstitial pair), $E_{0.27}$; the cross sections are near 1.5×10^{-18} cm^2 and 2×10^{-17} cm^2, respectively. Due to the low capture cross section and the annealing behaviour under bias, *it was speculated that $E_{0.37}$ is the double acceptor level of the E center*. A trap, $E_{0.23}$, is related to Sb and seemingly grows up by interstitial capture, possibly hindered by a small barrier. The amplitude of a trap $E_{0.29}$ is strongly enhanced by proton relative to electron irradiation, and $E_{0.29}$ is suggested to be divacancy-related. One significant hole trap, $H_{0.30}$, was present in Sb-doped but not in O-doped material. The apparent annealing behaviour of $H_{0.30}$ depends on the mode of detection (MCTS or injection-pulse DLTS). $H_{0.30}$ is strongly attractive to holes, and whereas firm identification cannot be made, we cautiously presented the idea that it be the single acceptor level of the E center. Correspondence was pointed out between seemingly varying results in the literature.

Appendix A

Further experiments with MCTS in *n*-type Ge

The hole filling of the trap $H_{0.30}$ in Ge is studied as a function of optical--filling pulse duration. It is shown that this kind of experiment can possibly be used to reveal if $H_{0.30}$ and $E_{0.37}$ are different charge states of the same defect (viz., the E center).

A.1 On the possible coupling between $E_{0.37}$ and $H_{0.30}$

In Chap. 10, it was speculated that the $H_{0.30}$ level in the lower half of the band gap might be a charge transition of the E center, which was otherwise shown to posses the level $E_{0.37}$ in the upper half of the band gap. We argued that it could be misleading to test this proposal simply by comparing the annealing behaviours of $H_{0.30}$ and $E_{0.37}$. In the following, we will propose an alternative experiment that may be suitable to reveal if $E_{0.37}$ and $H_{0.30}$ are indeed coupled (i.e., different levels belonging to the same defect).

The experiment rests on the fact that $H_{0.30}$ acts as a hole trap and on the assumption that $E_{0.37}$ acts as a recombination center. This assumption is justified under illumination conditions (where $E_{\mathrm{F_p}}$ is pulled downward in the band gap [183]); we have namely observed that the DLTS amplitude of $E_{0.37}$ is somewhat reduced if an optical (*clearing*) pulse is applied in the short time interval that lies immediately after the voltage pulse that fills the center with electrons but before the period of time in which the capacitance transient is probed. Thus, $E_{0.37}$ had captured holes during the clearing pulse and the level has the recombination property. Consequently, filling of $E_{0.37}$ with holes will compete with filling of $H_{0.30}$ with holes if the two are coupled – and if they are not coupled, the hole filling of one of the levels will not influence the hole filling of the other level.

The relevant emission and capture processes during illumination are depicted in Fig. A.1. e_{p0} is the rate of hole emission in the (0/–) transition, and the capture rates of holes at (0/–) and (–/=), and the capture rate of electrons

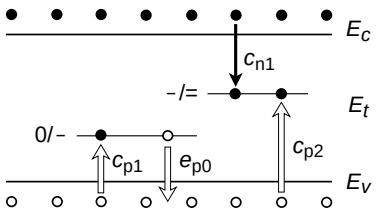

Figure A.1: Dominant emission and capture rates for a hole trap [(0/–) in this figure] and a recombination center [(–/=) in this figure].

at (–/=) are given by

$$c_{p1} = \sigma_{p1}\langle v_p\rangle_{th}\Delta p \tag{A.1}$$
$$c_{p2} = \sigma_{p2}\langle v_p\rangle_{th}\Delta p \tag{A.2}$$
$$c_{n1} = \sigma_{n1}\langle v_n\rangle_{th}\Delta n. \tag{A.3}$$

where Δn and Δp are the concentrations of available electrons and holes, respectively. Notice that $\sigma_{n1} \equiv \sigma_n^{E_{0.37}}$ is known [Eq. (10.6)], and so is $e_{p0} \equiv e_p^{H_{0.30}}$ (Fig. 10.6). For $\langle v_p\rangle_{th}$, we will use 10^7 cm/s.

Assume now that the levels are indeed coupled. By n_0, n_1, and n_2 we will denote the occupancies of the (0), (–), and (=) charge states. They must fulfill the boundary condition

$$n_0 + n_1 + n_2 = 1, \tag{A.4}$$

and the following system of rate equations must be obeyed:

$$\frac{dn_0}{dt} = -e_{p0}n_0 + c_{p1}n_1 \tag{A.5}$$
$$\frac{dn_1}{dt} = e_{p0}n_0 - c_{p1}n_1 - c_{n1}n_1 + c_{p2}n_2 \tag{A.6}$$
$$\frac{dn_2}{dt} = + c_{n1}n_1 - c_{p2}n_2, \tag{A.7}$$

Due to the small penetration depth of light in Ge ($1/e$ penetration depth $\sim$ 0.5 μm at the wavelength employed), we can consider two different experimental situations:

(i) *Front-side illumination.* – Under this condition, the optical filling pulse was varied and the filling of $H_{0.30}$ with holes was monitored at $T = 140$ K; see Fig. A.2. Optical excitation occurs in the depletion region very close to the interface and, for this reason, holes will primarily be captured into the (–) state rather than (=). Therefore, we have the initial conditions $n_0 = 0$, $n_1 = 1$, and $n_2 = 0$ in the probed region. To a crude approximation [183], Δp can be related to the photocurrent density J_{ph} (i.e., the current flow that is generated in the

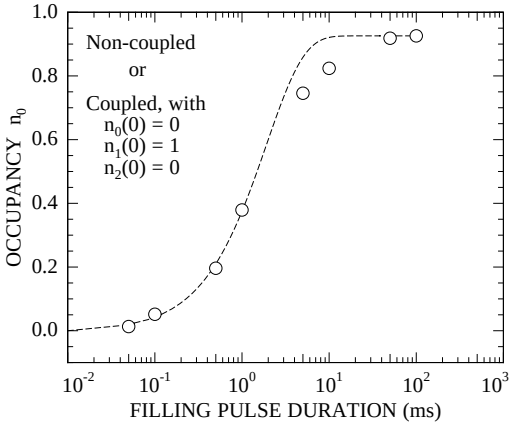

Figure A.2: Relative population n_0 of the (0) charge state of $H_{0.30}$, as a function of optical filling pulse, applied through a semitransparent Schottky barrier at 140 K. Symbols (○) are measured values, the solid curve is Eq. (A.10). A reverse bias of 2 V was used; the photocurrent was $J_{\rm ph} = 2.25 \times 10^{-3}$ A/cm^2.

diode due to optical excitation of electron–hole pairs) by

$$\Delta p = \frac{J_{\rm ph}}{e\mu_{\rm p}\mathcal{E}_{\rm max}}. \tag{A.8}$$

$$= 2.6 \times 10^8 \text{ cm}^{-3} \tag{A.9}$$

Here, we used the experimental parameters of $J_{\rm ph} = 2.25 \times 10^{-3}$ A/cm^2 and reverse bias 2 V, the latter from which the electric field value $\mathcal{E}_{\rm max}$ was calculated. We will roughly have $\Delta n = \Delta p$ from the photo generation, but in fact, since $\sigma_{\rm n1}$ is very small [Eq. (10.6)], the $c_{\rm n1}n_1$ terms can safely be neglected in the rate equations, and n_2 will remain equal to zero. Therefore, the system has a simple solution $n_0^{\rm nc}$ which is identical to that obtained if the levels were *not* coupled [since hole filling into (=) is never of importance and n_2 remains equal to zero],

$$n_0^{\rm nc}(t) = \frac{c_{\rm p1}}{e_{\rm p0} + c_{\rm p1}} \left[1 - \exp(-c_{\rm p1}t)\right]. \tag{A.10}$$

By fitting to the short-time data points, we obtain at $T = 140$ K

$$\sigma_{\rm p1} \equiv \sigma_{\rm p}^{H_{0.30}} = 1.8 \times 10^{-13} \text{ cm}^2. \tag{A.11}$$

This is a very large cross section, as is indeed expected for an attractive center (0/–). We remind the reader, however, that Δp was derived very simplistically, and we did not take into account the proper depth distribution $\Delta p(x)$. At longer filling times ($\gtrsim$ 5 ms), the deviation of the data points from exponential behaviour (Fig. A.2) is probably caused by slower hole capture towards the deep end of the optical penetration depth [184].

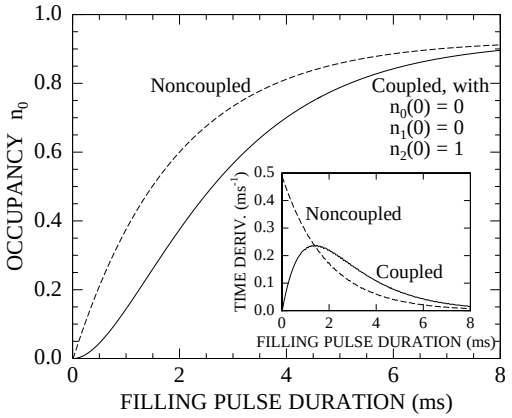

Figure A.3: Relative population n_0 of the (0) charge state of $H_{0.30}$, as a function of optical filling pulse. The solid curve is a numerical calculation if the (0/–) and (−/=) levels are coupled [it is identical to Eq. (A.12) at small filling levels]; the dashed line is the solution if the levels are not coupled [Eq. (A.10)]. The inset shows the time derivatives of n_0 in the two different scenarios.

(ii) *Electrical majority-filling pulse and back-side illumination.* – This case is of particular interest. Due to practical circumstances, we have not yet employed this method, but back-side illumination has been applied previously to Ge [8]. In n-type material, holes that are optically generated (at the backside of the sample) within a few diffusion lengths[43] of the space-charge region, will potentially reach the region and be swept through it. But electrons are effectively repelled by the electric field, that is, $\Delta n = 0$. Since the flux of holes is from the *bulk* side, holes will now be able to interact with the recombination center $E_{0.37}$ since, at the deep end of the depletion layer, $E_{0.37}$ will be in the (=) charge state. In order to ensure a maximum (close to 1) population of the (=) state in a larger region (viz., most of the depletion region), an *electric filling pulse*, as in normal DLTS, may be applied immediately prior to the optical hole generation. In addition to interaction with the (=) state, holes may also be trapped at $H_{0.30}$ in the (–) state, if populated, and these processes will compete if the levels are coupled. So if we do assume that the levels are coupled and that initial conditions in the probed region are $n_0 = 0$, $n_1 = 0$, $n_2 = 1$, we find numerically a solution $n_0^{\mathrm{cpl}}(t)$ that is shown in Fig. A.3 as a solid line. For the calculation, we used $\Delta p = 2.6 \times 10^8$ cm^{-3} as before and $\sigma_{\mathrm{p2}} = 2\sigma_{\mathrm{p1}}$, corresponding to the double charge. At short times, a simple analytical solution can be obtained: We have already argued that $\Delta n = 0$, and at low occupancies of the (0) state, it will be fair to neglect the $e_{\mathrm{p0}} n_0$ term. The system can be transformed to a linear,

[43] If necessary, the sample should be mechanically thinned to ensure that the back-side hole generation will take place within a few diffusion lengths of the space-charge region.

nonhomogeneous second order equation, and we find

$$n_0^{\mathrm{cpl}}(t) \approx 1 - \frac{c_{\mathrm{p2}}}{c_{\mathrm{p2}} - c_{\mathrm{p1}}} \exp(-c_{\mathrm{p1}} t) + \frac{c_{\mathrm{p1}}}{c_{\mathrm{p2}} - c_{\mathrm{p1}}} \exp(-c_{\mathrm{p2}} t). \tag{A.12}$$

The hole filling of $H_{0.30}$, if non-coupled levels are assumed, is still given by n_0^{nc} [Eq. (A.10)]. A striking difference between the two situations appears when taking the time derivatives in the limit $t \to 0$:

$$\frac{\mathrm{d}n_0^{\mathrm{nc}}}{\mathrm{d}t} \xrightarrow[t\to 0]{} c_{\mathrm{p1}} \tag{A.13}$$

$$\frac{\mathrm{d}n_0^{\mathrm{cpl}}}{\mathrm{d}t} \xrightarrow[t\to 0]{} 0 \tag{A.14}$$

The derivatives have been plotted as a function of time in the inset of Fig. A.3. From these plots it is apparent that *the time derivative of $n_0(t)$ at small times can provide easy distinction between the coupled and the non-coupled case*.

Different initial conditions than that assumed above ($n_0 = 0$, $n_1 = 0$, $n_2 = 1$) should also be considered;[44] one could anticipate situations such as, e.g., $n_0 = 0$, $n_1 = 0.6$, and $n_2 = 0.4$ in the probed region at time zero. This will represent an intermediate case where $\mathrm{d}n_0^{\mathrm{cpl}}/\mathrm{d}t$ approaches a finite value, rather than zero. However, as $t \to 0$, $\mathrm{d}n_0^{\mathrm{cpl}}/\mathrm{d}t$ will still reach a maximum and then decrease. So also in this case may the coupled and non-coupled cases be distinguished by the curvature of the filling curve: As long as n_2 has a non-zero initial population in the probed region, the occupancy $n_0(t)$ will have a *positive* curvature at short times if the levels are coupled, but it will have a *negative* curvature at short times if the levels are not coupled.

[44] The steady-state trap occupancies are actually a function of depth and depend on $n(x)$ and $p(x)$ which determine the positions of the quasi Fermi levels, $E_{\mathrm{F_{n(x)}}}$ and $E_{\mathrm{F_p}}(x)$. For a calculation of these properties in the dark and under illumination, see, e.g., Ref. [183].

References

The number(s) after each entry refer to the page(s) where citation was made.

[1] P. A. Packan, MRS Bulletin **25**, 18 (2000): *Scaling Transistors into the Deep-Submicron Regime*. 2

[2] Semiconductor Industry Association: http://www.semichips.org. 2, 31

[3] *The International Technology Roadmap for Semiconductors*, SIA (Semiconductor Industry Association:), 1999. 2, 31

[4] W. C. Holton, Solid State Techn. **40**, 119 (1997): *Silicon germanium: Finally for real*. 2, 81, 102

[5] G. D. Watkins: *The Lattice Vacancy in Silicon*, in *Deep Centers in Semiconductors*, edited by S. T. Pantelides, chap. 3, pp. 147–183, Gordon and Breach Science Publishers, New York, 1986. 3, 13, 14, 116

[6] A. Nylandsted Larsen, C. Christensen, and J. Wulff Petersen, J. Appl. Phys. **86**, 4861 (1999): *Room-temperature vacancy migration in crystalline Si from an ion-implanted surface layer*. 3, 125

[7] A. Mesli, E. Courcelle, T. Zundel, and P. Siffert, Phys. Rev. B **35**, 8049 (1987): *Process-induced and gold acceptor defects in silicon*. 3, 113

[8] A. Blondeel, P. Clauws, and C. Vyncke, J. Appl. Phys. **81**, 6767 (1997): *Optical deep level transient spectroscopy of minority traps in n-type high-purity germanium*. 3, 136

[9] P. M. Fahey, P. B. Griffin, and J. D. Plummer, Rev. Mod. Phys. **61**, 289 (1989): *Point defects and dopant diffusion in silicon*. 5, 9, 11, 13, 17, 47

[10] S. M. Hu, Mat. Sci. and Engineering **R13**, 105 (1994): *Nonequilibrium point defects and diffusion in silicon*. 5, 9, 10, 13, 17, 73

[11] R. J. Borg and G. J. Dienes: *An Introduction to Solid State Diffusion*, Academic Press, Inc., San Diego, 1988. 5, 11, 145

[12] P. Haahr Christensen: IRENE (*I*on-*re*distribution *n*umerical *e*mulator), PC programme, 1995. 6

[13] A. Ural, P. B. Griffin, and J. D. Plummer, J. Appl. Phys. **85**, 6440 (1999): *Fractional contributions of microscopic diffusion mechanisms for common dopants and self-diffusion in silicon*. 8, 9

[14] J. Philibert: *Atom movements, Diffusion and mass transport in solids*, Les Éditions de Physique, Les Ulis, France, 1991. 8, 145

[15] H.-J. Gossmann, T. E. Haynes, P. A. Stolk, D. C. Jacobson, G. H. Gilmer, J. M. Poate, H. S. Luftman, T. K. Mogi, and M. O. Thompson, Appl. Phys. Lett. **71**, 3862 (1997): *The interstitial fraction of diffusivity of common dopants in Si*. 9, 10

[16] N. E. B. Cowern, K. T. F. Janssen, G. F. A. van de Walle, and D. J. Gravesteijn, Phys. Rev. Lett. **65**, 2434 (1990): *Impurity Diffusion via an Intermediate Species: the B–Si system*. 9

[17] N. E. B. Cowern, G. F. A. van de Walle, D. J. Gravesteijn, and C. J. Vriezema, Phys. Rev. Lett. **67**, 212 (1991): *Experiments on Atomic-Scale Mechanisms of Diffusion*. 9

[18] A. Ural, P. B. Griffin, and J. D. Plummer, Phys. Rev. Lett. **83**, 3454 (1999): *Self-Diffusion in Silicon: Similarity between the Properties of Native Point Defects*. 10, 17, 21, 61

[19] H. Bracht, N. A. Stolwijk, and H. Mehrer, Phys. Rev. B **52**, 16542 (1995): *Properties of intrinsic point defects in silicon determined by zinc diffusion experiments under nonequilibrium conditions*. 10, 11, 17

[20] P. M. Fahey, S. S. Iyer, and G. J. Scilla, Appl. Phys. Lett. **54**, 843 (1989): *Experimental evidence of both interstitial- and vacancy-assisted diffusion of Ge in Si*. 10, 18

[21] P. Kringhøj and A. Nylandsted Larsen, Phys. Rev. B **56**, 6396 (1997): *Anomalous diffusion of tin in silicon*. 10, 17, 21, 61

[22] J. W. Mayer and S. S. Lau: *Electronic Materials Science: For integrated Circuits in Si and GaAs*, Macmillan Publishing Company, New York, 1990. 10, 14

[23] A. Giese, N. A. Stolwijk, and H. Bracht, Appl. Phys. Lett. **77**, 642 (2000): *Double-hump diffusion profiles of copper and nickel in germanium wafers yielding vacancy-related information*. 10

[24] W. T. C. Fang, T. T. Fang, P. B. Griffin, and J. D. Plummer, Appl. Phys. Lett. **68**, 2085 (1996): *Surface and bulk point defect generation in Czochralski and float zone type silicon wafers*. 10

[25] M. Lannoo and J. Bourgoin: *Point Defects in Semiconductors I, Theoretical Aspects*, vol. 22 of *Springer Series in Solid-State Sciences*, Springer Verlag, Berlin, 1981. 11

[26] J. S. Nelson, P. A. Schultz, and A. F. Wright, Appl. Phys. Lett. **73**, 247 (1998): *Valence and atomic size dependent exchange barriers in vacancy-mediated dopant diffusion*. 11, 19, 71

[27] O. Pankratov, H. Huang, T. D. de la Rubia, and C. Mailhiot, Phys. Rev. B **56**, 13172 (1997): *As–vacancy interaction and ring mechanism of diffusion in Si*. 11, 19, 20, 41

[28] J. Xie and S. P. Chen, Phys. Rev. Lett. **83**, 1795 (1999): *Diffusion and Clustering in Heavily Arsenic-Doped Silicon: Discrepancies and Explanation*. 11, 20, 51, 53, 55, 57

[29] B. Sadigh, T. J. Lenosky, S. K. Theiss, M.-J. Caturla, T. D. de la Rubia, and M. A. Foad, Phys. Rev. Lett. **83**, 4341 (1999): *Mechanism of Boron Diffusion in Silicon: An Ab Initio and Kinetic Monte Carlo Study*. 11, 23

[30] J. L. Newton, A. P. Chatterjee, R. D. Harris, and G. D. Watkins: (1983), proceedings of International Conference on Defects in Semiconductors, Amsterdam 1982. Physica B **14** 3551 (1976). 13

[31] G. D. Watkins: *Native defects and their interactions with impurities in silicon*, in *Defects and Diffusion in Silicon Processing*, edited by T. D. de la Rubia, S. Coffa, P. A. Stolk, and C. S. Rafferty, vol. 469 of *MRS Symposia Proceedings*, p. 139, Materials Research Society, Pittsburgh, 1997. 13, 114

[32] J. A. Van Vechten: *A Simple Man's View of the Thermochemistry of Semiconductors*, in *Handbook on Semiconductors*, edited by T. S. Moss, vol. 3: *Materials, Properties and Preparation*, ed. S. P. Keller, p. 1, North-Holland, New York, 1980. 13, 14

[33] C. V. Budtz-Jørgensen, P. Kringhøj, A. Nylandsted Larsen, and N. V. Abrosimov, Phys. Rev. B **58**, 1110 (1998): *Deep-level transient spectroscopy of the Ge–vacancy pair in Ge-doped n-type silicon*. 14

[34] R. B. Fair: *Concentration Profiles of Diffused Dopants in Silicon*, in *Impurity Doping Processes in Silicon*, edited by F. F. Y. Wang, chap. 7, pp. 315–442, North-Holland, Amsterdam, 1981. 15, 16, 86, 88, 93

[35] R. B. Fair and G. R. Weber, J. Appl. Phys. **44**, 273 (1793): *Effect of complex formation on diffusion of arsenic in silicon*. 16, 51, 52, 53, 55, 57

[36] F. Wittel and S. Dunham, Appl. Phys. Lett. **66**, 1415 (1995): *Diffusion of phosphorus in arsenic and boron doped silicon*. 16, 50, 55, 59

[37] A. Nylandsted Larsen, K. K. Larsen, P. E. Andersen, and B. G. Svensson, J. Appl. Phys. **73**, 691 (1993): *Heavy doping effects in the diffusion of group IV and V impurities in silicon*. 16, 35, 41, 42, 46, 50, 54, 55, 57, 58, 60

[38] R. B. Fair, M. L. Manda, and J. J. Wortman, J. Mater. Res. **1**, 705 (1986): *The diffusion of antimony in heavily doped and n- and p-type silicon*. 16, 35, 54, 55

[39] J. L. Hoyt and J. F. Gibbons: *Rapid thermal annealing of As in Si*, in *Rapid Thermal Processing*, edited by T. O. Sedgwick, T. E. Seidel, and B.-Y. Tsaur, vol. 52 of *MRS Symposia Proceedings*, pp. 15–22, Materials Research Society, Pittsburgh, 1986. 16

[40] E. Vainonen-Ahlgren, T. Ahlgren, J. Likonen, S. Lehto, and J. Keinonen, Appl. Phys. Lett. **77**, 690 (2000): *Identification of vacancy charge states in diffusion of arsenic in germanium*. 16, 128

[41] H. Bracht, E. E. Haller, and R. Clark-Phelps, Phys. Rev. Lett. **81**, 393 (1998): *Silicon Self-Diffusion in Isotope Heterostructures*. 17

[42] P. Kringhøj and R. G. Elliman, Appl. Phys. Lett. **65**, 324 (1994): *Diffusion of ion-implanted Sn in Si, $Si_{1-x}Ge_x$, and Ge*. 17, 21, 61, 93

[43] A. Nylandsted Larsen and P. Kringhøj, Appl. Phys. Lett. **68**, 2684 (1996): *Diffusion of Sb in relaxed $Si_{1-x}Ge_x$*. 17, 37, 40, 68, 86, 93

[44] P. Dorner, W. Gust, B. Predel, U. Roll, A. Lodding, and H. Odelius, Philos. Mag. A **49**, 557 (1984): *Investigations by SIMS of the bulk impurity diffusion of Ge in Si*. 17, 18

[45] G. Hettich, H. Mehrer, and K. Maier: *Tracer diffusion of ^{71}Ge and ^{31}Si in intrinsic and doped silicon*, in *Defects and Radiation Effects in Semiconductors*, edited by J. H. Albany, vol. 46, pp. 500–7, Inst. Phys., London, 1979. 17, 18

[46] S. T. Pantelides: *Atomic diffusion processes in silicon*, in *Impurities, Defects and Diffusion in Semiconductors: Bulk and Layered Structures*, edited by D. J. Wolford, J. Bernholc, and E. E. Haller, vol. 163 of *MRS Symposia Proceedings*, pp. 511–521, Materials Research Society, Pittsburgh, 1990. 17

[47] O. Sugino and A. Oshiyama, Phys. Rev. B **46**, 12335 (1992): *Microscopic mechanism of atomic diffusion in Si under pressure*. 17

[48] S. M. Hu, Phys. Stat. Sol. (b) **60**, 595 (1973): *On Interaction Potential, Correlation Factor, Vacancy Mobility, and Activation Energy of Impurity Diffusion in Diamond Lattice*. 18, 19

[49] S. M. Hu: *Diffusion in silicon and germanium*, in *Atomic Diffusion in Semiconductors*, edited by D. Shaw, pp. 205–233, Plenum Press, London, 1973. 18

[50] S. T. Dunham and C. D. Wu, J. Appl. Phys. **78**, 2362 (1995): *Atomistic models of vacancy-mediated diffusion in silicon*. 18, 19, 35, 42, 51

[51] G. D. Watkins, Phys. Rev. B **12**, 4383 (1975): *Defects in irradiated silicon: EPR of the tin–vacancy pair*. 21

[52] G. D. Watkins, Solid State Commun. **17**, 1205 (1975): *Isotope effects in the EPR spectrum of a tin–vacancy pair in silicon*. 21

[53] G. Kresse and J. Furthmüller, Phys. Rev. B **54**, 11169 (1996): *Efficient iterative schemes for* ab initio *total-energy calculations using a plane-wave basis set*. 21

[54] M. Kaukonen and R. Jones and S. Öberg, to be submitted to Phys. Rev. B. 21, 61

[55] E. Kasper and J. C. Bean (editors): *Silicon-molecular beam epitaxy*, CRC Press, Inc., Boca Raton, Florida, 1988. 25, 27, 28

[56] S. M. Sze: *Semiconductor Devices, Physics and Technology*, Bell Telephone Laboratories, Inc., John Wiley & Sons, 1985. 26

[57] J. Fage-Pedersen and J. Lundsgaard Hansen (1999) (unpublished) . 27

[58] P. M. Rousseau, P. B. Griffin, W. T. Fang, and J. D. Plummer, J. Appl. Phys. **84**, 3593 (1998): *Arsenic-deactivation enhanced diffusion: A time, temperature and concentration study*. 28, 54, 65, 66, 70, 71, 75

[59] A. Agarwal, T. E. Haynes, D. J. Eaglesham, H.-J. Gossmann, D. C. Jacobson, and J. M. Poate, Appl. Phys. Lett. **70**, 3332 (1997): *Interstitial defects in silicon from 1–5 keV Si^+ ion implantation*. 28

[60] P. A. Stolk, H.-J. Gossmann, D. J. Eaglesham, D. C. Jacobson, C. S. Rafferty, G. H. Gilmer, M. Jaraíz, J. M. Poate, H. S. Luftman, and T. E. Haynes, J. Appl. Phys. **81**, 6031 (1997): *Physical mechanisms of transient enhanced dopant diffusion in ion-implanted silicon*. 28

[61] R. G. Wilson, F. A. Stevie, and C. W. Magee: *Secondary Ion Mass Spectrometry, a Practical Handbook For Depth Profiling and Bulk Impurity Analysis*, John Wiley & Sons, Inc., New York, 1989. 28, 29

[62] D. P. Woodruff and T. A. Delchar: *Modern Techniques of Surface Science*, Second Edition, Cambridge Solid State Science Series, Cambridge University Press, Cambridge, 1994. 28, 30

[63] L. C. Feldman and J. W. Mayer: *Fundamentals of Surface And Thin Film Analysis*, Elsevier Science Publishing Co., Inc., New York, 1986. 28, 34

[64] http://www.simsworkshop.org. 28

[65] P. Sigmund: *Sputtering by Ion Bombardment; Theoretical Concepts*, in *Sputtering by Particle Bombardment*, edited by R. Berisch, vol. I, chap. 2, Springer-Verlag, New York, 1981. 28

[66] D. Krüger, P. Gaworzewski, R. Hurps, and H. P. Zeindl, J. Vac. Sci. Technol B **14**, 341 (1996): *Characterization of B and Sb delta-doping profiles in Si and $Si_{1-x}Ge_x$ alloys grown by molecular-beam epitaxy*. 30, 31

[67] K. Wittmaack, J. Vac. Sci. Technol B **16**, 2776 (1998): *Artifacts in low-energy depth profiling using oxygen primary ion beams: Dependence on impact angle and oxygen flooding conditions*. 30, 31

[68] V. K. F. Chia, G. R. Mount, M. J. Edgell, and C. W. Magee, J. Vac. Sci. Technol B **17**, 2345 (1999): *Recent advances in secondary ion mass spectrometry to characterize ultralow energy ion implants*. 30, 31

[69] R. Loesing, G. M. Guryanov, J. L. Hunter, and D. P. Griffis, J. Vac. Sci. Technol B **18**, 509 (2000): *Secondary ion mass spectrometry depth profiling of ultrashallow phosphorous in silicon*. 30

[70] P. C. Zalm and C. J. Vriezema, Nucl. Inst. and Meth. B **67**, 495 (1992): *On some factors limiting depth resolution during SIMS profiling*. 31

[71] H. H. Andersen, Appl. Phys. **18**, 131 (1979): *The Depth Resolution of Sputter Profiling*. 31

[72] M. Petravić, B. G. Svensson, and J. S. Williams, Appl. Phys. Lett. **62**, 278 (1993): *On the estimation of depth resolution during sputter profiling*. 31

[73] J. Kocanda, V. Fesič, M. Veselý, J. Breza, and M. Kadlečíková, Appl. Phys. Lett. **57**, 1206 (1995): *Estimation of the depth resolution of secondary ion mass spectrometry at the interface SiO_2/Si*. 31

[74] K. Wittmaack, J. Vac. Sci. Technol B **12**, 258 (1994): *Secondary ion mass spectrometry depth profiling of boron and antimony deltas in silicon: Comparison of the resolution functions using oxygen bombardment at different energies and impact angles*. 31

[75] M. G. Dowsett, R. D. Barlow, H. S. Fox, and R. Kubiak, J. Vac. Sci. Technol B **10**, 336 (1992): *Secondary ion mass spectrometry depth profiling of boron, antimony, and germanium deltas in silicon and implications for profile deconvolution*. 31

[76] M. G. Dowsett and D. P. Chu, J. Vac. Sci. Technol B **16**, 377 (1998): *Quantification of secondary-ion-mass spectroscopy depth profiles using maximum entropy deconvolution with a sample independent response function*. 31

[77] D. B. Williams and C. B. Carter: *Transmission electron microscopy: a textbook for materials science*, Plenum Press, New York, 1996. 33

[78] D. Mathiot and J. C. Pfister, J. Appl. Phys. **66**, 970 (1989): *Dopant redistribution in heavily doped silicon: Confirmation of the validity of the vacancy-percolation model*. 35, 40, 41, 46, 49, 50

[79] E. Antoncik, J. Electrochem. Soc. **141**, 3593 (1994): *Enhanced Diffusion of Dopants at Concentrations near the Solubility Limit*. 35, 42, 46

[80] M. Ramamoorthy and S. T. Pantelides, Phys. Rev. Lett. **76**, 4753 (1996): *Complex Dynamical Phenomena in Heavily Arsenic Doped Silicon*. 35, 41, 51, 52, 53, 55, 57, 66, 71

[81] S. List and H. Ryssel, J. Appl. Phys. **83**, 7595 (1998): *Atomistic modeling of high--concentration effects of impurity diffusion in silicon*. 35, 42, 51

[82] A. Nylandsted Larsen, P. Kringhøj, J. Lundsgaard Hansen, and S. Yu. Shiryaev, J. Appl. Phys. **81**, 2173 (1997): *Isoconcentration studies of antimony diffusion in silicon*. 35, 41, 54, 58, 59

[83] A. Nylandsted Larsen, S. Yu. Shiryaev, E. S. Sørensen, and P. Tidemand-Petersson, Appl. Phys. Lett. **48**, 1805 (1986): *Rapid thermal annealing of high concentration, arsenic implanted silicon single crystals*. 35, 41, 46, 50, 55, 59

[84] F. A. Trumbore: *Solid solubilities of impurities in Ge and Si*, in *The Bell System Technical Journal*, vol. 39, pp. 205–233, Jan. 1960. 37

[85] P. Kringhøj, A. Nylandsted Larsen, and S. Yu. Shiryaev, Phys. Rev. Lett. **76**, 3372 (1996): *Diffusion of Sb in Strained and Relaxed Si and SiGe*. 37, 40, 86, 91, 92

[86] S. Yu. Shiryaev, J. Lundsgaard Hansen, P. Kringhøj, and A. Nylandsted Larsen, Appl. Phys. Lett. **67**, 2287 (1995): *Pseudomorhic $Si_{1-x}Sn_x$ alloy films grown by molecular beam epitaxy on Si*. 39

[87] H. Rücker, B. Heinemann, W. Röpke, R. Kurps, G. Lippert, and H. J. Osten, Appl. Phys. Lett. **73**, 1682 (1998): *Suppressed diffusion of boron and carbon in carbon-rich silicon*. 40, 68

[88] D. Mathiot and J. C. Pfister, J. Phys. (France) Lett. **43**, L453 (1982): *High Concentration diffusion of P in Si: a percolation problem?* 40, 41, 46, 47, 48, 49, 50, 55

[89] D. Mathiot and J. C. Pfister, J. Appl. Phys. **55**, 3518 (1984): *Dopant diffusion in silicon: A consistent view involving nonequilibrium defects*. 40, 41, 46, 47, 48, 50, 55, 59

[90] P. Haahr Christensen: Private communication. 41

[91] C. van Opdorp, L. J. van IJzendoorn, C. W. Fredriksz, and D. J. Gravesteijn, J. Appl. Phys. **72**, 4047 (1992): *A model for the diffusion and precipitation of antimony in highly doped δ layers in silicon*. 41, 51

[92] S. A. Fedotov, Phys. Stat. Sol. (b) **186**, 375 (1994): *Diffusion of Electrically Active Sb Atoms in Heavily Doped Silicon*. 42

[93] E. Antoncik, J. Electrochem. Soc. **142**, 3170 (1995): *Theory of Isoconcentration Diffusion in semiconductors*. 46

[94] W. Walukiewicz, Phys. Rev. B **50**, 5221 (1994): *Defect formation and diffusion in heavily doped semiconductors*. 46

[95] D. Mathiot and J. C. Pfister, J. Appl. Phys. **66**, 970 (1989): *Diffusion of arsenic in silicon: Validity of the vacancy-percolation model*. 46, 55

[96] D. Stauffer: *Introduction to Percolation Theory*, Taylor & Francis Ltd, London, 1985. 48, 49, 50

[97] P. Haahr Christensen: *An Experimental Study of the Diffusion and Deactivation of Ion Implanted As in Si during RTA*, Master's thesis, Inst. of Physics and Astronomy, Univ. of Aarhus (1995). 48

[98] M. A. Berding and A. Sher, Phys. Rev. B **58**, 3853 (1998): *Electronic quasi-chemical formalism: Application to arsenic deactivation in silicon*. 51, 56, 66, 75

[99] S. Solmi and D. Nobili, J. Appl. Phys. **83**, 2484 (1998): *High concentration diffusivity and clustering of arsenic and phosphorus in silicon*. 51, 52, 53, 54, 55, 57

[100] See, e.g., Borg and Dienes [11] or Philibert [14]. 52, 55

[101] D. W. Lawther, U. Myler, and P. J. Simpson, Appl. Phys. Lett. **67**, 3575 (1995): *Vacancy generation resulting from electrical deactivation of arsenic*. 54, 58, 59, 66

[102] A. Armigliato, F. Romanato, A. Drigo, A. Carnera, C. Brizard, J. R. Regnard, and J. L. Allain, Phys. Rev. B **52**, 1859 (1995): *Anomalous low-temperature dopant diffusivity and defect structure in Sb- and Sb/B-implanted annealed silicon samples*. 54, 66

[103] P. E. Andersen, A. Nylandsted Larsen, P. Tidemand-Petersson, and G. Weyer, Appl. Phys. Lett. **53**, 755 (1988): *Diffusion of ion-implanted Sn and Sb in heavily doped n-type silicon*. 54, 57

[104] E. Müller, A. Nylandsted Larsen, and G. Weyer, Hyp. Int. **93**, 1395 (1994): *Evidence for vacancy percolation in highly-doped silicon*. 54, 57, 66

[105] TSUPREM-4, *User's manual*, Technology Modelling Associates, Palo Alto, CA 1995. 54

[106] A. Nylandsted Larsen (unpublished) . 54, 55, 58

[107] J. Heller: *Catch-22*, Simon and Schuster, New York, 1961. 55

[108] D. J. Chadi, C. H. Park, D. L. Adler, M. A. Marcus, and H.-J. Gossmann, Phys. Rev. Lett. **79**, 4834 (1997): *Fermi-Level-Pinning in Highly* n*-Doped Silicon*. 58, 67, 76

[109] D. Nobili: *Solubility of Sb in Si*, in *Properties of Silicon* [190], pp. 401–3. 58, 66

[110] D. Nobili, S. Solmi, A. Parisini, M. Derdour, A. Armigliato, and L. Moro, Phys. Rev. B **49**, 2477 (1994): *Precipitation, aggregation, and diffusion in heavily arsenic--doped silicon*. 59, 66

[111] A. Nylandsted Larsen, J. J. Goubet, P. Mejlholm, J. Sherman Christensen, M. Fanciulli, H. P. Gunnlaugsson, G. Weyer, J. Wulff Petersen, A. Resende, M. Kaukonen, R. Jones, S. Oberg, P. R. Briddon, B. G. Svensson, J. L. Lindstrom, and S. Dannefaer, Phys. Rev. B **62**, 4535 (2000): *Tin–vacancy acceptor levels in electron-irradiated n-type silicon*. 60

[112] M. M. Bunea and S. T. Dunham, Phys. Rev. B **61**, R2397 (2000): *Monte Carlo study of vacancy-mediated impurity diffusion in silicon*. 60

[113] E. V. Thomsen, O. Hansen, K. Harrekilde-Petersen, J. Lundsgaard Hansen, S. Yu. Shiryaev, and A. Nylandsted Larsen, J. Vac. Sci. Technol B **12**, 3016 (1994): *Thermal stability of highly Sb-doped molecular beam epitaxy silicon grown at low temperatures: Structural and electrical characterization*. 65, 71

[114] P. D. Agnello, T. O. Sedgwick, and J. Cotte, J. Electrochem. Soc. **140**, 2703 (1993): *Growth rate enhancement of heavy n- and p-type doped silicon deposited by atmospheric-pressure chemical vapor deposition at low temperatures*. 65

[115] A. Nylandsted Larsen, F. T. Pedersen, G. Weyer, R. Galloni, R. Rizzoli, and A. Armigliato, J. Appl. Phys. **59**, 1908 (1986): *The nature of electrically inactive antimony in silicon*. 66, 75, 77

[116] K. C. Pandey, A. Erbil, G. S. Cargill, and R. F. Boehme, Phys. Rev. Lett. **61**, 1282 (1988): *Annealing of Heavily Arsenic-Doped Silicon: Electrical Deactivation and a New Defect Complex*. 66

[117] J. L. Allain, J. R. Regnard, A. Bourret, A. Parisini, A. Armigliato, G. Tourillon, and S. Pizzini, Phys. Rev. B **46**, 9434 (1992): *Extended x-ray absorption fine-structure study of the local atomic structure in As^+ heavily implanted silicon*. 66

[118] K. Saarinen, J. Nissilä, H. Kauppinen, M. Hakala, M. J. Pusaka, P. Hautojärvi, and C. Corbel, Phys. Rev. Lett. **82**, 1883 (1999): *Identification of Vacancy-Impurity Complexes in Highly n-type Si*. 66

[119] D. Nobili: *Solubility of As in Si*, in *Properties of Silicon* [190], pp. 398–400. 66

[120] J. L. Benton, S. Libertino, P. Kringhøj, D. J. Eaglesham, J. M. Poate, and S. Coffa, J. Appl. Phys. **82**, 120 (1997): *Evolution from point to extended defects in ion implanted silicon*. 67

[121] W. E. Beadle, J. C. C. Tsai, and R. D. Plummer (editors): *Quick Reference Manual for Silicon Integrated Circuit Technology*, Wiley, New York, 1985. 68, 115

[122] H.-J. Gossmann, C. S. Rafferty, A. M. Vredenberg, H. S. Luftman, F. C. Unterwald, D. J. Eaglesham, D. C. Jacobson, T. Boone, and J. M. Poate, Appl. Phys. Lett. **64**, 312 (1994): *Time dependence of dopant diffusion in δ-doped Si films and properties of Si point defects*. 68

[123] T. Y. Tan and U. Gösele, Appl. Phys. A **37**, 1 (1985): *Point Defects, Diffusion Processes, and Swirl Defect Formation in Silicon*. 75

[124] Hall measurements on Sb layers in MBE-Si; unpublished. 75

[125] P. Kuo, J. L. Hoyt, J. F. Gibbons, J. E. Turner, and D. Lefforge: *Boron diffusion in Si and $Si_{1-x}Ge_x$*, in *Strained Layer Epitaxy - Materials, Processing, and Device Applications*, edited by E. Fitzgerald, J. Hoyt, K.-Y. Cheng, and J. Bean, vol. 379 of *MRS Symposia Proceedings*, pp. 373–8, Materials Research Society, Pittsburgh, 1995. 81, 89, 93

[126] S. M. Hu, Phys. Rev. B **45**, 4498 (1992): *Diffusion and segregation in heterostructures: Theory, two limiting cases, and internal strain*. 82

[127] H.-H. Chen, U. M. Gösele, and T. Y. Tan, Appl. Phys. A **68**, 19 (1999): *Dopant diffusion and segregation in semiconductor heterostructures: Part 2. B in Ge_xSi_{1-x}/Si structures*. 82

[128] R. Hull: *Misfit Strain and Accommodation in SiGe Heterostructures*, in Hull and Bean [191], chap. 3. 83

[129] N. E. B. Cowern, P. C. Zalm, P. van der Sluis, D. J. Gravesteijn, and W. B. de Boer, Phys. Rev. Lett. **72**, 2585 (1994): *Diffusion in Strained Si(Ge)*. 83, 91, 92

[130] N. E. B. Cowern, W. J. Kersten, R. C. M. De Kruif, J. G. M. Van Berkum, W. B. de Boer, D. J. Gravesteijn, and C. Bulle-Liewma: *Interdiffusion mechanisms in coherently strained SiGe multilayers*, in *Proceedings of the Fourth International Symposium on Process Physics and Modeling in Semiconductor Technology*, edited by G. R. Srinivasan, C. S. Murthy, and S. T. Dunham, pp. 195–209, Electrochem. Soc, 1996. 84

[131] E. A. Fitzgerald, Y.-H. Xie, D. Brasen, M. L. Green, J. Michel, P. E. Freeland, and B. E. Weir, J. Electronic Mater. **19**, 949 (1990): *Elimination of dislocations in heteroepitaxial MBE and RTCVD Ge_xSi_{1-x} grown on patterned Si substrates*. 85

[132] E. Kasper and H.-J. Herzog, Thin Solid Films **44**, 357 (1977): *Elastic strain and misfit dislocation density in $Si_{0.92}Ge_{0.08}$ films on silicon substrates*. 86

[133] P. Kuo, J. L. Hoyt, J. F. Gibbons, J. E. Turner, and D. Lefforge, Appl. Phys. Lett. **66**, 580 (1995): *Effects of strain on boron diffusion in Si and $Si_{1-x}Ge_x$*. 86

[134] N. Jeng and S. T. Dunham, J. Appl. Phys. **72**, 2049 (1992): *Interstitial supersaturation during oxidation of silicon in steam ambients*. 86

[135] K. Osada, Y. Zaitsu, S. Matsumoto, M. Yoshida, E. Arai, and T. Abe, J. Electrochem. Soc. **142**, 202 (1995): *Effect of Stress in the Deposited Silicon Nitride Films on Boron Diffusion of Silicon*. 87

[136] Y. M. Haddara, B. T. Folmer, M. E. Law, and T. Buyuklimnali, Appl. Phys. Lett. **77**, 1976 (2000): *Accurate measurements of the intrinsic diffusivities of boron and phosphorus in silicon*. 88

[137] A. Yu. Kuznetsov, J. S. Christensen, M. K. Linnarsson, B. G. Svensson, H. H. Radamson, J. Grahn, and G. Landgren, MRS Symposia Proceedings **568**, 271 (1999): *Diffusion of phosphorus in strained Si/SiGe/Si heterostructures*. 89

[138] W. C. Dunlap, Jr., Phys. Rev. **94**, 1954 (1531): *Diffusion of Impurities in Germanium*. 91

[139] W. Meyer and H. Neldel, Zeitschr. f. Techn. Physik **18**, 588 (1937): *Über die Beziehungen zwischen der Energiekonstanten ε und der Mengenkonstanten a in der Leitwerts-Temperaturformel bei oxydischen Halbleitern*. 92

[140] A. Yelon, B. Movaghar, and H. Branz, Phys. Rev. B **46**, 12244 (1992): *Origin and consequences of the compensation (Meyer-Neldel) law*. 92

[141] J. Bourgoin and M. Lannoo: *Point Defects in Semiconductors II, Experimental Aspects*, vol. 22 of *Springer Series in Solid-State Sciences*, Springer Verlag, Berlin, 1981. 95, 97, 98

[142] P. Blood and J. W. Orton: *The Electrical Characterization of Semiconductors: Majority Carriers and Electron States*, vol. 14 of *Techniques of Physics*, Academic Press, London, 1992. 95, 96, 99, 148

[143] V. N. Abakumov, V. I. Perel, and I. N. Yassievich: *Nonradiative recombination in semiconductors*, vol. 33 of *Modern Problems in Condensed Matter Sciences*, North--Holland, Amsterdam, 1991. 96

[144] E. H. Rhoderick: *Metal–semiconductor contacts*, Monographs in Electrical and Electronic Engineering, Clarendon Press, Oxford, 1978. 97

[145] D. V. Lang, J. Appl. Phys. **45**, 3014 (1974): *Fast capacitance transient apparatus: application to ZnO and O centers in GaP p-n junctions*. 98

[146] A. Resende, R. Jones, S. Öberg, and P. R. Briddon, Phys. Rev. Lett. **82**, 2111 (1999): *Calculations of Electrical Levels of Deep Centers: Application to Au–H and Ag–H Defects in Silicon*. 98

[147] L. Dobaczewski, K. Gościński, K. Bonde Nielsen, A. Nylandsted Larsen, J. Lundsgaard Hansen, and A. R. Peaker, Phys. Rev. Lett. **83**, 4582 (1999): *Alloy splitting of gold and platinum acceptor levels in SiGe*. 98

[148] See, e.g., *Germanium Silicon: Physics and Materials*, Vol. 56 of *Semiconductors and semimetals*, edited by R. Hull and J. C. Bean (Academic Press, San Diego, 1999). 102

[149] J. C. Pigg and J. H. Crawford, Jr., Phys. Rev. **135**, A1141 (1964): *Radiation Effects and Their Annealing in Co^{60}-Gamma-Irradiated Sb-Doped Germanium*. 102

[150] J. C. Bourgoin, P. M. Mooney, and F. Poulin: *Irradiation-induced defects in germanium*, in *Defects and Radiation Effects in Semiconductors*, edited by R. R. Hasiguti, pp. 33–43, The Inst. of Physics, London, 1980. 102, 112, 120

[151] N. Fukuoka and H. Saito, Jpn. J. Appl. Phys. **21**, 930 (1982): *Defect States in n-Type Germanium Irradiated with 1.5 MeV Electrons*. 102, 112, 114, 117, 118, 119, 120, 121, 123

[152] N. Fukuoka, H. Saito, and Y. Kambe, Jpn. J. Appl. Phys. **22**, L353 (1983): *Oxygen--Related Defects in Irradiated Germanium*. 102, 112, 113, 119, 120, 123

[153] V. Nagesh and J. W. Farmer, J. Appl. Phys. **63**, 1549 (1988): *Study of irradiation-induced defects in germanium*. 102, 112, 113, 114, 119, 120

[154] P. Marie, M. Levalois, and P. Bogdanski, J. Appl. Phys. **74**, 868 (1993): *Deep level transient spectroscopy of high-energy heavy ion irradiation-induced defects in n-type germanium*. 102, 112, 119, 120, 121, 124

[155] R. E. Whan, Phys. Rev. **140**, A 690 (1965): *Investigations of Oxygen-Defect Interactions between 25 and 700°K in Irradiated Germanium*. 102, 120

[156] R. E. Whan, J. Appl. Phys. **37**, 2435 (1966): *Oxygen-Defect Complexes in Neutron-Irradiated Germanium*. 102

[157] P. Clauws, Mat. Sci. and Engineering B **36**, 213 (1996): *Oxygen related defects in germanium*. 102

[158] P. Blood and J. W. Orton: *The Electrical Characterization of Semiconductors: Majority Carriers and Electron States*, vol. 14 of *Techniques of Physics* [142] (1992). 103

[159] F. Poulin and J. C. Bourgoin, Phys. Rev. B **26**, 6788 (1982): *Characteristics of the electron traps produced by electron irradiation in n-type germanium*. 112, 120

[160] P. M. Mooney, F. Poulin, and J. C. Bourgoin, Phys. Rev. B **28**, 3372 (1983): *Annealing of electron-induced defects in n-type germanium*. 112, 117, 120

[161] N. Fukuoka and H. Saito, Jpn. J. Appl. Phys. **20**, L519 (1981): *Radiation Defects in n-Type Germanium Studied by Deep Level Transient Spectroscopy*. 112, 114

[162] C. Zistl: Ph.D. thesis, Hahn Meitner Institut, Berlin (1997). 112, 118, 119, 120

[163] H. Haesslein, R. Sielemann, and C. Zistl, Phys. Rev. Lett. **80**, 2626 (1998): *Vacancies and Self-Interstitials in Germanium Observed by Perturbed Angular Correlation Spectroscopy*. 114

[164] R. I. Scace and G. A. Slack, J. Chem. Phys. **30**, 1551 (1959): *Solubility of carbon in silicon and germanium*. 114

[165] A. Mesli, H. av Skarði, and A. Nylandsted Larsen: To be published. 114, 125

[166] J. J. Goubet and D. Stievenard, Appl. Phys. Lett. **66**, 1409 (1995): *Annealing Study of electron irradiation-induced defects in SiGe alloys*. 114

[167] P. Kringhøj and A. Nylandsted Larsen, Phys. Rev. B **52**, 16333 (1995): *Irradiation-induced defect states in epitaxial n-type $Si_{1-x}Ge_x$ alloy layers*. 114, 126

[168] J. Weber and M. I. Alonso, J. Appl. Phys. **1**, 1 (1998): *Near-band-gap photoluminescence of Si-Ge alloys*. 115, 127

[169] L. Kimerling, H. M. DeAngelis, and J. W. Diebold, Solid State Commun. **16**, 171 (1975): *On the role of defect charge state in the stability of point defects in silicon*. 115, 116

[170] F. Poulin and J. C. Bourgoin: *Minority carrier traps in electron irradiated n-type germanium*, in *Recent Developments in Condensed Matter Physics*, edited by J. T. Devreese, L. F. Lemmens, V. E. van Doren, and J. van Royen, pp. 83–88, Plenum Press, New York, 1981. 117

[171] F. Poulin and J. C. Bourgoin, Revue Phys. Appl. **15**, 15 (1980): *Threshold energy for atomic displacement in electron irradiated germanium*. 118, 120

[172] P. M. Mooney, M. Cherki, and J. C. Bourgoin, J. Phys. (France) Lett. **40**, L (1979): *Energy levels in electron irradiated n-type germanium*. 120

[173] P. Marie, M. Levalois, and E. Paumier, J. Appl. Phys. **79**, 7555 (1996): *Swift-heavy-ion induced damage in germanium: An evaluation of defect introduction rates*. 120, 121

[174] A. Colder, M. Levalois, and P. Marie, J. Appl. Phys. **88**, 3082 (2000): *Study of electron, proton, and swift heavy ion irradiation of n-type germanium using deep level transient spectroscopy*. 123, 124

[175] A. O. Evwaraye, J. Appl. Phys. **48**, 734 (1977): *Electron-irradiation induced damage in antimony-doped silicon*. 124

[176] A. O. Evwaraye, J. Appl. Phys. **48**, 1840 (1977): *Annealing of irradiation-induced defects in arsenic-doped silicon*. 124

[177] S. D. Brotherton and P. Bradley, J. Appl. Phys. **53**, 5720 (1982): *Defect production and lifetime control in electron and γ-irradiated silicon*. 124

[178] H. Huber, W. Assmann, H. D. Mieskes, S. A. Karamian, A. Mucklich, R. Grotzschel, W. Prusseit, E. Gazis, R. Vlastou, M. Kokkoris, and E. Kossionidis, Nucl. Inst. and Meth. B **122**, 542 (1997): *Void formation in Ge induced by high energy heavy ion irradiation*. 124

[179] H. av Skarði: *DLTS-undersøgelse af divakancen i n-type $Si_{1-x}Ge_x$* (DLTS investigation of the divacancy in *n*-type $Si_{1-x}Ge_x$), Master's thesis, Inst. of Phys. and Astronomy, University of Aarhus (1998). 125, 126

[180] M. J. Shaw and M. Jaros: *Fundamental Physics of Strained Layer GeSi: Quo Vadis?*, in Hull and Bean [191], chap. 4, pp. 169–223. 127

[181] C. S. Peng, Z. Y. Zhao, H. Chen, J. H. Li, Y. K. Li, L. W. Guo, D. Y. Dai, Q. Huang, J. M. Zhou, Y. H. Zhang, T. T. Sheng, and C. H. Tung, Appl. Phys. Lett. **72**, 3160 (1998): *Relaxed $Ge_{0.9}Si_{0.1}$ alloy layers with low threading dislocation densities grown on low-temperature Si buffers*. 128

[182] A. Fazzio, A. Janotti, A. J. R. da Silva, and R. Mota, Phys. Rev. B **61**, R2401 (2000): *Microscopic picture of the single vacancy in germanium*. 128

[183] J. A. Davidson and J. H. Evans, J. Appl. Phys. **81**, 251 (1997): *Detection statistics of deep levels in minority carrier transient spectroscopy*. 133, 134, 137

[184] E. Meijer, H. G. Grimmeiss, and L.-A. Ledebo, J. Appl. Phys. **55**, 4266 (1984): *Dynamics of capture from free-carrier tails in depletion regions and its consequences in junction experiments*. 135

[185] J. Fage-Pedersen, A. Nylandsted Larsen, P. Gaiduk, J. Lundsgaard Hansen, and M. Linnarsson, Phys. Rev. Lett. **81**, 5856 (1998): *Sn-background induced diffusion enhancement of Sb in Si.* Same as [I] (see preface).

[186] P. Gaiduk, J. Fage-Pedersen, J. Lundsgaard Hansen, and A. Nylandsted Larsen, Phys. Rev. B **59**, 7278 (1999): *Sb-precipitation-induced injection of Si self-interstitials in Si.* Same as [II] (see preface).

[187] J. Fage-Pedersen, P. Gaiduk, and A. Nylandsted Larsen, J. Appl. Phys. **88**, 3254 (2000): *Si self-interstitial injection from Sb complex formation in Si.* Same as [III] (see preface).

[188] J. Fage-Pedersen, A. Mesli, and A. Nylandsted Larsen, Phys. Rev. B **62**, 10116 (2000): *Irradiation-induced defects in Ge studied by transient spectroscopies.* Same as [IV] (see preface).

[189] N. Zangenberg, J. Fage-Pedersen, J. Lundsgaard Hansen, and A. Nylandsted Larsen: *Boron diffusion in strained and relaxed $Si_{1-x}Ge_x$*. Same as [IV] (see preface).

[190] *Properties of Silicon*, EMIS Data Reviews Series No. 4, INSPEC, The Institute of Electrical Engineers, London, 1988. 145, 146

[191] R. Hull and J. C. Bean (editors): *Germanium Silicon: Physics and Materials*, vol. 56 of *Semiconductors and semimetals*, ed. by R. K. Willardson and Eicke R. Weber, Academic Press, San Diego, 1999. 147, 150

Comprehensive author index

The numbers refer to the entry in the list of references.

Abakumov, V. N. 143
Abe, T. 135
Abrosimov, N. V. 33
Adler, D. L. 108
Agarwal, A. 59
Agnello, P. D. 114
Ahlgren, T. 40
Albany, J. H. 45
Allain, J. L. 102, 117
Alonso, M. I. 168
Andersen, H. H. 71
Andersen, P. E. 37, 103
Antoncik, E. 79, 93
Arai, E. 135
Armigliato, A. 102, 110, 115, 117
Assmann, W. 178
av Skarði, H. 165, 179

Barlow, R. D. 75
Beadle, W. E. 121
Bean, J. 125
Bean, J. C. 55, 128, 180, 191
Benton, J. L. 120
Berding, M. A. 98
Berisch, R. 65
Bernholc, J. 46
Blondeel, A. 8
Blood, P. 142, 158
Boehme, R. F. 116
Bogdanski, P. 154
Bonde Nielsen, K. 147
Boone, T. 122
Borg, R. J. 11
Bourgoin, J. 25, 141
Bourgoin, J. C. 150, 159, 160, 170, 171, 172
Bourret, A. 117
Bracht, H. 19, 23, 41
Bradley, P. 177
Branz, H. 140
Brasen, D. 131
Breza, J. 73
Briddon, P. R. 111, 146
Brizard, C. 102
Brotherton, S. D. 177
Budtz-Jørgensen, C. V. 33
Bulle-Liewma, C. 130
Bunea, M. M. 112
Buyuklimnali, T. 136

Cargill, G. S. 116
Carnera, A. 102
Carter, C. B. 77
Caturla, M.-J. 29
Chadi, D. J. 108
Chatterjee, A. P. 30
Chen, H. 181
Chen, H.-H. 127
Chen, S. P. 28
Cheng, K.-Y. 125
Cherki, M. 172
Chia, V. K. F. 68
Christensen, C. 6
Christensen, J. S. 137
Chu, D. P. 76
Clark-Phelps, R. 41
Clauws, P. 8, 157
Coffa, S. 31, 120
Colder, A. 174
Corbel, C. 118
Cotte, J. 114
Courcelle, E. 7
Cowern, N. E. B. 16, 17, 129, 130
Crawford, Jr., J. H. 149

da Silva, A. J. R. 182
Dai, D. Y. 181
Dannefaer, S. 111
Davidson, J. A. 183
de Boer, W. B. 129, 130
De Kruif, R. C. M. 130
de la Rubia, T. D. 27, 29, 31
DeAngelis, H. M. 169
Delchar, T. A. 62
Derdour, M. 110
Devreese, J. T. 170
Diebold, J. W. 169
Dienes, G. J. 11
Dobaczewski, L. 147
Dorner, P. 44
Dowsett, M. G. 75, 76

Drigo, A. 102
Dunham, S. 36
Dunham, S. T. 50, 112, 130, 134
Dunlap, Jr., W. C. 138

Eaglesham, D. J. 59, 60, 120, 122
Edgell, M. J. 68
Elliman, R. G. 42
Erbil, A. 116
Evans, J. H. 183
Evwaraye, A. O. 175, 176

Fage-Pedersen, J. 57, 185, 186, 187, 188, 189
Fahey, P. M. 9, 20
Fair, R. B. 34, 35, 38
Fanciulli, M. 111
Fang, T. T. 24
Fang, W. T. 58
Fang, W. T. C. 24
Farmer, J. W. 153
Fazzio, A. 182
Fedotov, S. A. 92
Feldman, L. C. 63
Fesič, V. 73
Fitzgerald, E. 125
Fitzgerald, E. A. 131
Foad, M. A. 29
Folmer, B. T. 136
Fox, H. S. 75
Fredriksz, C. W. 91
Freeland, P. E. 131
Fukuoka, N. 151, 152, 161
Furthmüller, J. 53

Gaiduk, P. 185, 186, 187
Galloni, R. 115
Gaworzewski, P. 66
Gazis, E. 178
Gibbons, J. F. 39, 125, 133
Giese, A. 23
Gilmer, G. H. 15, 60
Gościński, K. 147
Gösele, U. 123
Gösele, U. M. 127
Gossmann, H.-J. 15, 59, 60, 108, 122
Goubet, J. J. 111, 166
Grahn, J. 137
Gravesteijn, D. J. 16, 17, 91, 129, 130
Green, M. L. 131
Griffin, P. B. 9, 13, 18, 24, 58
Griffis, D. P. 69
Grimmeiss, H. G. 184
Grotzschel, R. 178
Gunnlaugsson, H. P. 111
Guo, L. W. 181
Guryanov, G. M. 69
Gust, W. 44

Haahr Christensen, P. 12, 90, 97
Haddara, Y. M. 136
Haesslein, H. 163
Hakala, M. 118
Haller, E. E. 41, 46
Hansen, O. 113
Harrekilde-Petersen, K. 113
Harris, R. D. 30
Hasiguti, R. R. 150
Hautojärvi, P. 118
Haynes, T. E. 15, 59, 60
Heinemann, B. 87
Heller, J. 107
Herzog, H.-J. 132
Hettich, G. 45
Holton, W. C. 4
Hoyt, J. 125
Hoyt, J. L. 39, 125, 133
Hu, S. M. 10, 48, 49, 126
Huang, H. 27
Huang, Q. 181
Huber, H. 178
Hull, R. 128, 180, 191
Hunter, J. L. 69
Hurps, R. 66

Iyer, S. S. 20

Jacobson, D. C. 15, 59, 60, 122
Janotti, A. 182
Janssen, K. T. F. 16
Jaraíz, M. 60
Jaros, M. 180
Jeng, N. 134
Jones, R. 111, 146

Kadlečíková, M. 73
Kambe, Y. 152
Karamian, S. A. 178
Kasper, E. 55, 132
Kaukonen, M. 111
Kauppinen, H. 118
Keinonen, J. 40
Kersten, W. J. 130
Kimerling, L. 169
Kocanda, J. 73
Kokkoris, M. 178
Kossionidis, E. 178
Kresse, G. 53
Kringhøj, P. 21, 33, 42, 43, 82, 85, 86, 120, 167
Krüger, D. 66
Kubiak, R. 75
Kuo, P. 125, 133
Kurps, R. 87
Kuznetsov, A. Yu. 137

Landgren, G. 137
Lang, D. V. 145
Lannoo, M. 25, 141
Larsen, K. K. 37
Lau, S. S. 22
Law, M. E. 136
Lawther, D. W. 101
Ledebo, L.-A. 184
Lefforge, D. 125, 133
Lehto, S. 40
Lemmens, L. F. 170
Lenosky, T. J. 29
Levalois, M. 154, 173, 174
Li, J. H. 181
Li, Y. K. 181
Libertino, S. 120
Likonen, J. 40
Lindstrom, J. L. 111
Linnarsson, M. 185
Linnarsson, M. K. 137
Lippert, G. 87
List, S. 81
Lodding, A. 44
Loesing, R. 69
Luftman, H. S. 15, 60, 122
Lundsgaard Hansen, J. 57, 82, 86, 113, 147, 185, 186, 189

Magee, C. W. 61, 68
Maier, K. 45
Mailhiot, C. 27
Manda, M. L. 38
Marcus, M. A. 108
Marie, P. 154, 173, 174
Mathiot, D. 78, 88, 89, 95
Matsumoto, S. 135
Mayer, J. W. 22, 63
Mehrer, H. 19, 45
Meijer, E. 184
Mejlholm, P. 111
Mesli, A. 7, 165, 188
Meyer, W. 139
Michel, J. 131
Mieskes, H. D. 178
Mogi, T. K. 15
Mooney, P. M. 150, 160, 172
Moro, L. 110
Moss, T. S. 32
Mota, R. 182
Mount, G. R. 68
Movaghar, B. 140
Mucklich, A. 178
Müller, E. 104
Murthy, C. S. 130
Myler, U. 101

Nagesh, V. 153
Neldel, H. 139
Nelson, J. S. 26
Newton, J. L. 30
Nissilä, J. 118
Nobili, D. 99, 109, 110, 119
Nylandsted Larsen, A. 6, 21, 33, 37, 43, 82, 83, 85, 86, 103, 104, 106, 111, 113, 115, 147, 165, 167, 185, 186, 187, 188, 189

Öberg, S. 146
Oberg, S. 111
Odelius, H. 44
Orton, J. W. 142, 158
Osada, K. 135
Oshiyama, A. 47

Osten, H. J. 87

Packan, P. A. 1
Pandey, K. C. 116
Pankratov, O. 27
Pantelides, S. T. 5, 46, 80
Parisini, A. 110, 117
Park, C. H. 108
Paumier, E. 173
Peaker, A. R. 147
Pedersen, F. T. 115
Peng, C. S. 181
Perel, V. I. 143
Petravić, M. 72
Pfister, J. C. 78, 88, 89, 95
Philibert, J. 14
Pigg, J. C. 149
Pizzini, S. 117
Plummer, J. D. 9, 13, 18, 24, 58
Plummer, R. D. 121
Poate, J. M. 15, 59, 60, 120, 122
Poulin, F. 150, 159, 160, 170, 171
Predel, B. 44
Prusseit, W. 178
Pusaka, M. J. 118

Radamson, H. H. 137
Rafferty, C. S. 31, 60, 122
Ramamoorthy, M. 80
Regnard, J. R. 102, 117
Resende, A. 111, 146
Rhoderick, E. H. 144
Rizzoli, R. 115
Roll, U. 44
Romanato, F. 102
Röpke, W. 87
Rousseau, P. M. 58
Rücker, H. 87
Ryssel, H. 81

Saarinen, K. 118
Sadigh, B. 29
Saito, H. 151, 152, 161
Scace, R. I. 164
Schultz, P. A. 26
Scilla, G. J. 20
Sedgwick, T. O. 39, 114
Seidel, T. E. 39
Shaw, D. 49
Shaw, M. J. 180
Sheng, T. T. 181
Sher, A. 98
Sherman Christensen, J. 111
Shiryaev, S. Yu. 82, 83, 85, 86, 113
Sielemann, R. 163
Siffert, P. 7
Sigmund, P. 65
Simpson, P. J. 101
Slack, G. A. 164
Solmi, S. 99, 110
Sørensen, E. S. 83
Srinivasan, G. R. 130
Stauffer, D. 96
Stevie, F. A. 61
Stievenard, D. 166
Stolk, P. A. 15, 31, 60
Stolwijk, N. A. 19, 23
Sugino, O. 47
Svensson, B. G. 37, 72, 111, 137
Sze, S. M. 56

Tan, T. Y. 123, 127
Theiss, S. K. 29
Thompson, M. O. 15
Thomsen, E. V. 113
Tidemand-Petersson, P. 83, 103
Tourillon, G. 117
Trumbore, F. A. 84
Tsai, J. C. C. 121
Tsaur, B.-Y. 39
Tung, C. H. 181
Turner, J. E. 125, 133

Unterwald, F. C. 122
Ural, A. 13, 18

Vainonen-Ahlgren, E. 40
Van Berkum, J. G. M. 130
van de Walle, G. F. A. 16, 17
van der Sluis, P. 129
van Doren, V. E. 170
van IJzendoorn, L. J. 91
van Opdorp, C. 91
van Royen, J. 170

Van Vechten, J. A. 32
Veselý, M. 73
Vlastou, R. 178
Vredenberg, A. M. 122
Vriezema, C. J. 17, 70
Vyncke, C. 8

Walukiewicz, W. 94
Wang, F. F. Y. 34
Watkins, G. D. 5, 30, 31, 51, 52
Weber, G. R. 35
Weber, J. 168
Weir, B. E. 131
Weyer, G. 103, 104, 111, 115
Whan, R. E. 155, 156
Williams, D. B. 77
Williams, J. S. 72
Wilson, R. G. 61
Wittel, F. 36
Wittmaack, K. 67, 74
Wolford, D. J. 46
Woodruff, D. P. 62
Wortman, J. J. 38
Wright, A. F. 26
Wu, C. D. 50
Wulff Petersen, J. 6, 111

Xie, J. 28
Xie, Y.-H. 131

Yassievich, I. N. 143
Yelon, A. 140
Yoshida, M. 135

Zaitsu, Y. 135
Zalm, P. C. 70, 129
Zangenberg, N. 189
Zeindl, H. P. 66
Zhang, Y. H. 181
Zhao, Z. Y. 181
Zhou, J. M. 181
Zistl, C. 162, 163
Zundel, T. 7